

ULTRAFAST TRANSPORT EXPERIMENTS ON OPTICALLY-DRIVEN K_3C_{60}

Dissertation

zur Erlangung des Doktorgrades an der Fakultät
für Mathematik, Informatik und Naturwissenschaften

Fachbereich Physik
der Universität Hamburg



vorgelegt von

Joseph Daniel Adelinia

Hamburg

2025

Gutachter der Dissertation:	Prof. Dr. Andrea Cavalleri PD Dr. habil. Guido Meier
Zusammensetzung der Prüfungskommission:	Prof. Dr. Andrea Cavalleri Prof. Dr. Nils Huse PD Dr. habil. Guido Meier Prof. Dr. Michael Potthoff Prof. Dr. Tim Wehling
Vorsitzender der Prüfungskommission:	Prof. Dr. Michael Potthoff
Datum der Disputation:	04.04.2025
Vorsitzender Fach-Promotionsausschusses PHYSIK:	Prof. Dr. Wolfgang J. Parak
Leiter des Fachbereichs PHYSIK:	Prof. Dr. Markus Drescher
Dekan der Fakultät MIN:	Prof. Dr.-Ing. Norbert Ritter

Eidesstattliche Versicherung

Hiermit versichere ich an Eides statt, die vorliegende Dissertationsschrift selbst verfasst und keine anderen als die angegebenen Hilfsmittel und Quellen benutzt zu haben.

Sofern im Zuge der Erstellung der vorliegenden Dissertationsschrift generative Künstliche Intelligenz (gKI) basierte elektronische Hilfsmittel verwendet wurden, versichere ich, dass meine eigene Leistung im Vordergrund stand und dass eine vollständige Dokumentation aller verwendeten Hilfsmittel gemäß der Guten wissenschaftlichen Praxis vorliegt. Ich trage die Verantwortung für eventuell durch die gKI generierte fehlerhafte oder verzerrte Inhalte, fehlerhafte Referenzen, Verstöße gegen das Datenschutz- und Urheberrecht oder Plagiate.

Hamburg, den 17.01.2025



Joseph D. Adelinia

Abstract

Optical excitation has emerged as a powerful tool to investigate and control the properties of matter. Particular attention in this regard has been devoted to quantum materials, since they present a rich variety of entangled and topologically non-trivial phases that are extraordinarily sensitive to external parameters. Through coherent excitation with ultrashort laser pulses, it has been shown that complex transient phases can be induced on femtosecond timescales, demonstrating great potential for high-speed technology utilising non-equilibrium quantum phenomena.

Harnessing non-equilibrium phenomena in electronic devices is a natural next step for both scientific understanding and potential applications. Electronic devices allow properties to be measured under current and voltage biases, and provide a reliable platform for multiple components to interact, leading to more complex functionalities. However, conducting transport experiments on short-lived non-equilibrium phenomena necessitates a departure from conventional electronics. The first part of this thesis details the development of an ultrafast opto-electronic platform to carry out charge-transport and voltage measurements on timescales shorter than one picosecond.

Recent studies on the alkali-doped fulleride K_3C_{60} have demonstrated signatures of a light-induced superconducting-like phase at temperatures far above its equilibrium critical temperature. To date, however, this phenomenon has predominantly been characterised by its optical features in the terahertz frequency range. In this work, the light-induced phase was investigated in MBE-grown K_3C_{60} by means of sub-terahertz electronic transport. Two ultrafast transport experiments were conducted on granular thin films that revealed a finite enhancement in conductivity, characterised by nonlinear current-voltage behaviour in the excited state (Chapter 5) and inductive voltage dynamics upon in-current excitation (Chapter 6).

The results presented in this work complement a growing body of literature on ultrafast electronics. Furthermore, these experiments demonstrate the ultrafast electronic platform developed here as a valuable tool for investigating non-equilibrium phenomena, paving the way towards high-speed applications.

Zusammenfassung

Die optische Anregung hat sich als leistungsfähiges Instrument zur Erforschung und Kontrolle der Eigenschaften von Materie erwiesen. Besondere Aufmerksamkeit wurde dabei Quantenmaterialien gewidmet, da sie eine große Vielfalt verschränkter und topologisch nicht-trivialer Phasen aufweisen, die außerordentlich empfindlich auf externe Parameter reagieren. Es hat sich gezeigt, dass durch kohärente Anregung mit ultrakurzen Laserpulsen komplexe transiente Phasen auf Femtosekunden-Zeitskalen induziert werden können, was ein großes Potenzial für Hochgeschwindigkeitstechnologien unter Nutzung von Nicht-Gleichgewichts-Quantenphänomenen darstellt.

Die Nutzung von Nicht-Gleichgewichtsphänomenen in elektronischen Geräten ist ein natürlicher nächster Schritt sowohl für das wissenschaftliche Verständnis als auch für mögliche Anwendungen. Elektronische Geräte ermöglichen die Messung von Eigenschaften unter Strom- und Spannungsvorspannung und bieten eine zuverlässige Plattform für die Interaktion mehrerer Komponenten, was zu komplexeren Funktionen führt. Die Durchführung von Transportexperimenten zu kurzlebigen Nicht-Gleichgewichtsphänomenen erfordert jedoch eine Abkehr von der herkömmlichen Elektronik. Der erste Teil dieser Arbeit befasst sich mit der Entwicklung einer ultraschnellen optoelektronischen Plattform zur Durchführung von Ladungstransport- und Spannungsmessungen auf Zeitskalen von weniger als einer Pikosekunde.

Jüngste Studien über das alkalidotierte Fullerid K_3C_{60} haben Anzeichen für eine lichtinduzierte supraleitende Phase bei Temperaturen weit oberhalb der kritischen Gleichgewichtstemperatur gezeigt. Bislang wurde dieses Phänomen jedoch hauptsächlich durch seine optischen Eigenschaften im Terahertz-Frequenzbereich charakterisiert. In dieser Arbeit wurde die lichtinduzierte Phase in MBE-gewachsenem K_3C_{60} mittels elektronischem Transport im Sub-Terahertz-Bereich untersucht. Zwei ultraschnelle Transportexperimente wurden an polykristallinen Dünnschichten durchgeführt, die eine endliche Erhöhung der Leitfähigkeit zeigten, die durch ein nicht-lineares Strom-Spannungs-Verhalten im angeregten Zustand (Kapitel 5) und eine induktive Spannungsdynamik bei Stromanregung (Kapitel 6) gekennzeichnet ist.

Die in dieser Arbeit vorgestellten Ergebnisse ergänzen die wachsende Literatur über ultraschnelle Elektronik. Darüber hinaus zeigen diese Experimente, dass die hier entwickelte ultraschnelle elektronische Plattform ein wertvolles Instrument zur Untersuchung von Nicht-Gleichgewichtsphänomenen ist und den Weg für Hochgeschwindigkeitsanwendungen ebnet. german

List of publications

The results presented in this dissertation are based on the following publications:

1. **J. D. Adelinia**, E. Wang, M. Chavez-Cervantes, T. Matsuyama, M. Fechner, M. Buzzi, G. Meier, and A. Cavalleri. “Probing optically driven K_3C_{60} thin-films with an ultrafast voltmeter”. *Structural Dynamics* **12**, 024503 (2025).
2. E. Wang, **J. D. Adelinia**, M. Chavez-Cervantes, T. Matsuyama, M. Fechner, M. Buzzi, G. Meier, and A. Cavalleri. “Superconducting nonlinear transport in optically driven high-temperature K_3C_{60} ”. *Nature Communications* **14**, 7233 (2023).

Contents

1	Introduction	1
1.1	Quantum materials	1
1.2	Controlling matter with light	2
1.3	Structure of the thesis	3
2	Superconductivity in K_3C_{60}	5
2.1	A brief introduction to superconductivity	5
2.1.1	Phenomenology of superconductivity	5
2.1.2	Type II superconductivity	6
2.2	The alkali-doped fullerenes	9
2.2.1	Electronic properties	10
2.2.2	Superconductivity in the alkali-doped fullerenes	11
2.3	Optical control of superconductivity in K_3C_{60}	13
2.3.1	Equilibrium optical properties	14
2.3.2	Photoinduced optical properties	15
2.3.3	Tuning of the photoinduced state	16
2.4	Proposal for an ultrafast transport experiment	18
3	Ultrafast electronic transport	21
3.1	High-frequency transmission lines	21
3.1.1	Telegrapher's equations	22
3.1.2	Coplanar waveguide	24
3.2	Ultrafast photoconductive switches	25
3.2.1	Tuning the pulse amplitude	27
3.2.2	Pulse duration	28
3.3	Device design considerations	31
3.3.1	Sample placement	31
3.3.2	Waveguide dimensions	32
3.3.3	Launching a symmetric mode	34
3.3.4	Internal reflections	34

4	Device construction	37
4.1	Microstructuring the optoelectronic circuitry	39
4.2	MBE growth of K_3C_{60} thin-films	40
4.3	Integrating K_3C_{60} into ultrafast circuitry	45
4.3.1	Microstructuring K_3C_{60}	45
4.3.2	Hermetic sealing	47
4.4	Device characterisation	48
5	Nonlinear current-voltage behaviour in optically-driven K_3C_{60}	51
5.1	The critical current in superconductors	51
5.1.1	Origin in type I and type II superconductors	52
5.1.2	Extension to granular thin films	53
5.1.3	Effect of short current pulses	54
5.2	Probing with ultrafast currents	55
5.3	Ultrafast transport properties of equilibrium K_3C_{60}	56
5.3.1	Transmission and reflection in the metallic and superconducting states	56
5.3.2	Nonlinear current dependence below T_c	59
5.4	Photo-excitation of K_3C_{60} below T_c	61
5.5	Photo-excitation of K_3C_{60} above T_c	62
5.6	Summary	65
6	Ultrafast voltage dynamics in optically-driven K_3C_{60}	67
6.1	Experimental setup for ultrafast voltmeter measurements	68
6.1.1	Device layout	68
6.1.2	Applying the quasi-DC bias	69
6.2	Extraction of the on-chip voltage changes	70
6.2.1	Subtraction of zero-bias signal	70
6.2.2	Subtraction of constant offset	70
6.2.3	Removing reflections	71
6.2.4	Calibration of the transient voltage magnitudes	73
6.3	Photoinduced voltage dynamics for $T < T_c$	75
6.3.1	High-fluence excitation	76
6.3.2	Low-fluence excitation	78
6.4	Photoinduced voltage dynamics for $T > T_c$	80
6.5	Discussion on the $T > T_c$ photo-induced state	83
6.6	Simulations of the voltage dynamics	87
6.6.1	Granular two-fluid model	87
6.6.2	Pump-induced heating in a two-temperature model	92
6.6.3	Simulations for $T < T_c$	93

6.6.4 Simulations for $T > T_c$	95
6.7 Summary	97
7 Conclusions	99
7.1 Summary	99
7.2 Outlook	100
Bibliography	103
A Optical setup	123
B Electronic setup	127
C Calibration of the picosecond current pulses	129
D Processing of ultrafast voltmeter data	131
D.1 Raw data	131
D.2 Processed data	137

Chapter 1

Introduction

1.1 Quantum materials

In the past century, developments in solid state physics have brought about great advances in technology, fundamentally altering the way in which we live. The 20th century was dominated by the semiconductor—the key ingredient in LEDs, CCDs, and, of course, the transistor, which enabled an explosion of progress in computer logic. Nowadays, computer chips based on the transistor can be found in every facet of our lives, from our household computers and mobile phones to large-scale data centres and powerful supercomputers. These developments were made possible by the tunability of the semiconductor, with transport properties that are remarkably sensitive to electrostatic gating [1, 2], doping [3], and light [4, 5].

Semiconductor physics is fundamentally semi-classical; while the quantum-mechanical nature of the electron is necessary to explain the band structure of solids, concepts like entanglement and topology do not play a role in the observable properties. In some solids, however, these effects do manifest over macroscopic length scales and result in states that cannot be explained by a semi-classical picture, ranging from topological insulation to superconductivity [6]. We call these solids *quantum materials*.

Quantum materials not only offer a platform to explore and study how microscopic quantum interactions give rise to emergent phenomena on macroscopic length scales, but also show potential for applicability. For example, dissipationless transport in a superconductor opens up the possibility for lossless computational devices, energy transmission, and high magnetic field applications [7], while topologically protected quantum states may facilitate large-scale quantum computation [8].

A unique aspect of quantum materials is their hyper-sensitivity to their environment. Electronic wave functions are easily altered by scattering from defects or thermally

excited lattice vibrations, meaning that many quantum phases, such as superconductivity, are only present at low temperatures. A great research effort has been directed towards improving the robustness of such phases, allowing them to remain present at higher temperatures [9]. Sensitivity, however, also leads to tunability, and much work has been focused on enhancing these macroscopic quantum states by fine-tuning the crystal environment via pressure, strain, doping, heterostructuring, electrostatic gating, and magnetic fields [10].

1.2 Controlling matter with light

Recent efforts have moved beyond static methods of influencing these materials, and have opened up a new avenue of dynamical control through the use of light [10]. Broadly speaking, light fields introduce new possibilities for control of material properties that go beyond thermal excitation of a system or subsystem.

Symmetry is of fundamental importance for material properties, as the symmetry of a material determines which phenomena it can host. By breaking symmetry with optical fields, phenomena that were previously forbidden by symmetry become allowed, and in some cases may also be energetically favourable [11]. For example, use of circularly polarised light to break time-reversal symmetry has been shown to induce large effective magnetic fields in CeF_3 [12] and SrTiO_3 [13], as well as an anomalous Hall effect in graphene [14].

Periodic electric fields or driven lattice excitations can give rise to a time-periodic Hamiltonian with an altered ground state, known as Floquet engineering [15–20], which has been shown to alter the electronic states within a single optical cycle [21]. Light can also be used to directly modulate the crystal structure. One example of this is in SrTiO_3 , where it was demonstrated that optical driving of the A_{2u} phonon to large amplitudes produces strain in the material and induces a ferroelectric order that is absent in equilibrium [22]. Strong excitations have also been shown to bring oscillators out of the linear-potential regime [23] and, due to coupled modes, can even result in quasi-static crystal displacements that are orders of magnitude larger than those possible via static perturbation [24].

Various experiments have investigated optical control over many categories of quantum phenomena, including charge density wave order [25], magnetism [26–29], and superconductivity [30–32]. Ultrafast control of superconductivity in particular presents a promising research direction for high-speed, lossless electronics, and targeted excitation provides insight into which degrees of freedom have the strongest influence on superconductivity. In one candidate material, K_3C_{60} , superconducting-like

optical features have been observed upon mid-infrared excitation well above the equilibrium critical temperature T_c [32], with lifetimes far longer than the excitation pulse [33], demonstrating potential for devices exploiting ultrafast state switching. Experiments on this material form the backbone of this work, and a detailed background will be presented in Chapter 2.

Ultrafast phenomena in quantum materials have been studied using a range of techniques, including optical probes, time- and angle-resolved photo-emission spectroscopy, scattering, and ultrafast electronic transport [34]. In particular, ultrafast electronic transport has attracted significant attention as a bridge between fundamental research and functional application. Electronic transport measurements of ultrafast phenomena present a significant challenge due to the femtosecond to picosecond timescales over which these states develop and decay, which cannot be reached with conventional electronics. Nevertheless, it is a vital characterisation technique, providing information at frequencies below those accessible with ultrafast optics, enabling current- and voltage-dependent measurements, and, from an applications perspective, determining how optically-manipulated states can interact in larger devices of networked components. Such investigations have been made possible through the use of photo-conductive switches [4] and terahertz waveguides [35], and several recent works have demonstrated their use in condensed matter systems [14, 36–39].

1.3 Structure of the thesis

This thesis describes a series of ultrafast electronic transport experiments on the fulleride superconductor K_3C_{60} , and will primarily focus on investigating the photo-induced phase in this material. Chapter 2 will introduce K_3C_{60} and its material family, the alkali-doped fullerenes, alongside existing evidence for an optically driven superconducting-like phase at temperatures above T_c . Chapter 3 will outline the fundamental principles of ultrafast electronic transport, followed in Chapter 4 by the technical details of device construction. Two ultrafast electronic transport experiments are subsequently discussed in the following chapters: Chapter 5 reports the discovery of nonlinear transport in the photo-induced state using picosecond current pulses, and in Chapter 6, the voltage dynamics upon in-current excitation are investigated via an ultrafast voltmeter.

Chapter 2

Superconductivity in K_3C_{60}

2.1 A brief introduction to superconductivity

The discovery of superconductivity in 1911 by H. Kamerlingh Onnes [40] marked the beginning of more than a century of scientific investigation aimed at not only uncovering the fundamental origin of the phenomenon, but also driving progress towards key technological applications [41, 42]. Onnes's observation was that the resistivity of mercury, when cooled to a temperature below 4.2 K, reduced to *exactly* zero. This turns out to be only one of several defining properties of superconductivity that will be summarised in this section.

2.1.1 Phenomenology of superconductivity

Fig. 2.1 displays a sketch of a typical resistance-versus-temperature curve for a superconducting transition. The loss of resistivity occurs sharply at a temperature T_c , the superconducting critical temperature, which is intrinsic to the material itself. Below this temperature, persistent currents in superconducting rings have been observed to flow with no measurable decrease for a year [43]. Many of the potential applications of superconductivity arise from this property of perfect conductivity, such as lossless transmission lines and high-field superconducting magnets—the latter of which are even in use today in large-scale facilities like the Large Hadron Collider.

Perfect conductivity is, however, not the only defining feature of superconductivity. In 1933, Meissner and Ochsenfeld reported the observation of perfect diamagnetism in a superconductor [44]. When a magnetic field is applied to a bulk superconductor below its critical temperature, the magnetic field is completely excluded. This would be expected of a perfect conductor. The distinguishing feature of perfect diamagnetism is that, when the sequence is reversed, i.e. the superconductor is cooled

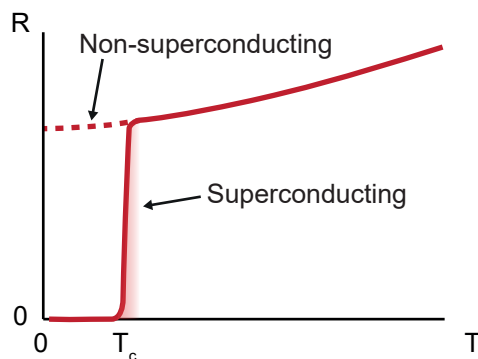


Figure 2.1: **Sketch of a typical superconducting transition.** When cooling through the critical temperature T_c , the resistance R reduces abruptly to zero.

through T_c in the presence of a magnetic field, this magnetic field gets expelled from the material bulk, rather than trapped inside it. This phenomenon, known as the Meissner-Ochsenfeld effect, is illustrated in Fig. 2.2a. Magnetic field lines flow around the superconductor, and the magnetic field inside the bulk is zero.

The Meissner-Ochsenfeld effect indicates that superconductivity competes energetically with the magnetic field, and indeed superconductivity is destroyed when the magnetic field exceeds a critical value H_c . This critical field is temperature dependent, and a typical phase diagram of a type I superconductor is sketched in Fig. 2.2b. At T_c , the critical field is reduced to zero and the material returns to its “normal” state.

Closely related to the critical magnetic field is the critical current. When an electronic current is applied to a superconductor, superconductivity will be suppressed when the current exceeds a critical value I_c . A resistance-versus-current curve is sketched in Fig. 2.3. In a simplified picture, the critical current can be viewed as arising from the self-field of the current in the superconductor. The critical current is reached when the self-field exceeds H_c . While the critical current is broadly related to the thermodynamic critical field, many complications arise from additional factors, and these will be discussed in more detail in chapter 5.

2.1.2 Type II superconductivity

Much of the above discussion has been based on type I superconductors, which exhibit perfect diamagnetism below a single critical magnetic field, above which

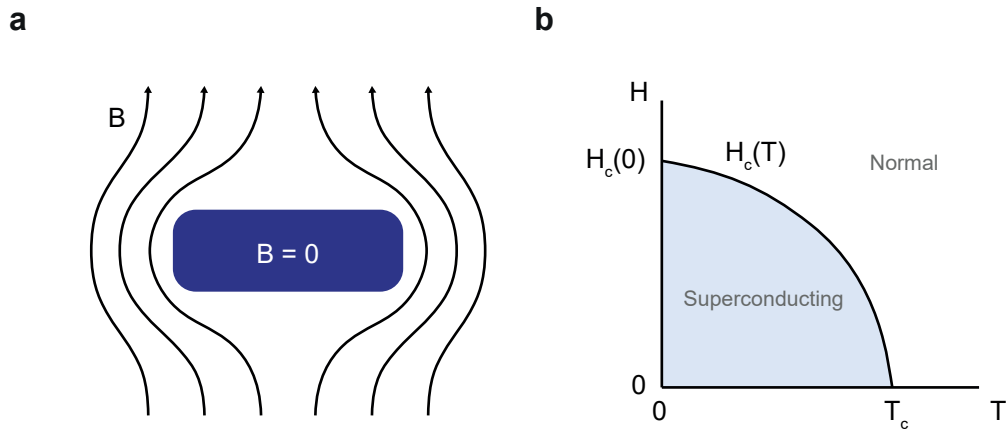


Figure 2.2: **The Meissner-Ochsenfeld Effect.** **a**, Sketch of magnetic field expulsion from a superconducting material. Field lines are redirected around the superconductor, such that the magnetic flux density inside the bulk is zero. **b**, A typical magnetic field vs temperature phase diagram for a type I superconductor.

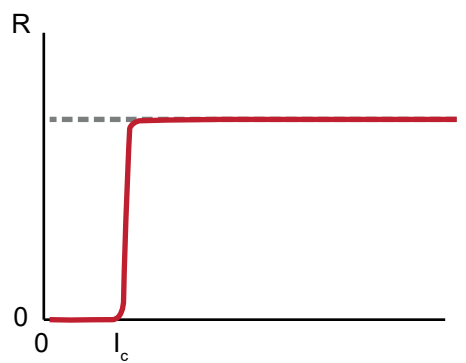


Figure 2.3: **The critical current.** Sketch of a typical current dependence of the resistance in a superconductor. Above a critical current I_c , the superconductor becomes resistive.

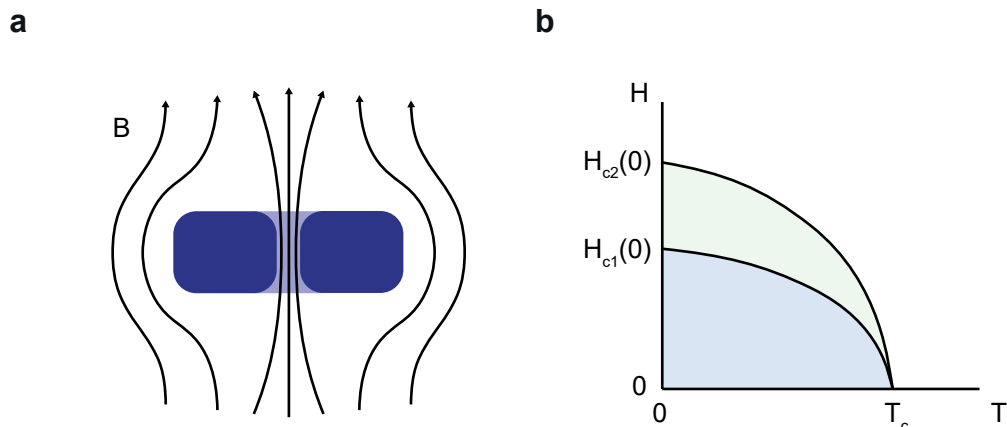


Figure 2.4: **Type II superconductivity.** **a**, Field lines of a magnetic flux vortex. **b**, A typical phase diagram for type II superconductivity. Spontaneous vortex formation occurs in the green region.

superconductivity is disrupted. A different variety, type II superconductivity, was first discovered experimentally in 1935 [45], but was not discussed theoretically until Alexei Abrikosov did so over two decades later [46]. Unlike type I superconductivity, type II superconductivity does not break down immediately upon reaching a critical magnetic field. Instead, magnetic flux begins to creep into the superconductor above a *lower* critical field H_{c1} , with the flux density increasing until superconductivity is completely suppressed above an *upper* critical field H_{c2} .

In the intermediate regime between H_{c1} and H_{c2} , magnetic flux penetrates into the material in the form of flux vortices. Flux vortices are filaments of quantized magnetic flux, inside which superconductivity breaks down. A superconductor with a vortex filament is sketched in Fig. 2.4a, and a phase diagram for a type II superconductor is sketched in Fig. 2.4b. Since the vortices offset the energy cost of magnetic field expulsion, H_{c2} is typically much larger than the thermodynamic critical field H_c . However, vortex motion gives rise to a voltage drop, resulting in energy dissipation when a current is applied. By introducing pinning centres to the materials, vortex motion can be inhibited, and these factors combine to provide a large increase in critical current for some type II superconductors.

For their great potential both in dissipationless electrical networks and high-magnetic-field applications, a great research effort has been directed towards finding materials with ever-increasing critical temperatures.

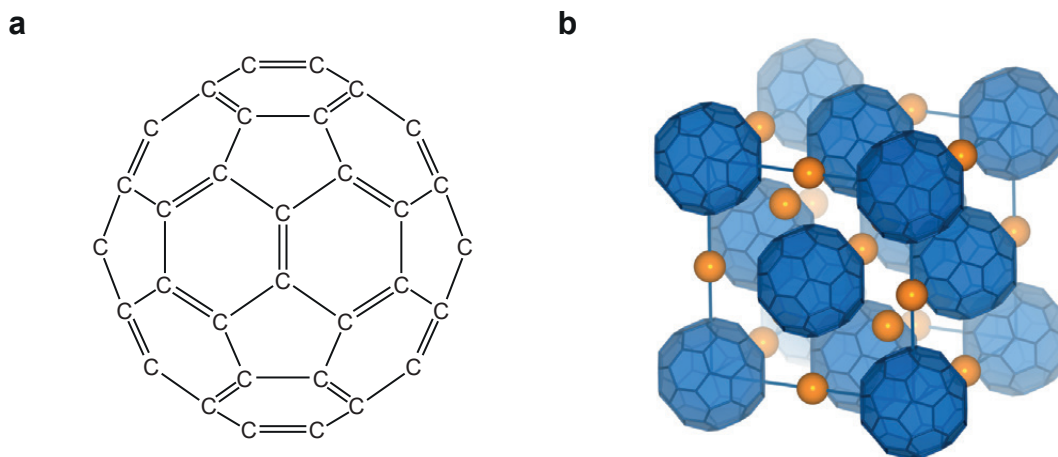


Figure 2.5: **The alkali-doped fullerenes.** **a**, Structure of the Buckminsterfullerene C_{60} [47]. **b**, Crystal structure of K_3C_{60} [52, 53]. The C_{60} molecules (blue) are arranged in an fcc structure, and intercalated with potassium (orange).

2.2 The alkali-doped fullerenes

The discovery of the fullerene C_{60} [47] marked the beginning of an explosion of research into its complex properties and potential applications, in both its molecular and crystalline forms. The C_{60} molecule, depicted in Fig. 2.5a, is an icosahedron of carbon atoms which boasts a high symmetry order of 120, a bulk modulus predicted to be larger than that of diamond [48–50], and an exotic and varied chemistry [51].

In its crystalline form, C_{60} forms a cubic structure with a lattice constant of 14.17 \AA [54]. Neglecting the orientation of the individual molecules, C_{60} possesses space group symmetry $Fm\bar{3}m$ at room temperature, and undergoes a phase transition to a simple cubic structure upon cooling [54–57]. While C_{60} is an insulator, the introduction of dopants drastically changes its electronic properties. This thesis will focus on the alkali-doped fulleride K_3C_{60} (Fig. 2.5b), where each potassium atom donates one electron to the C_{60} ground state. This compound is metallic at room temperature, and becomes superconducting below a critical temperature of 19.3 K [52, 58].

Not only does the potassium introduce additional charge carriers, but it also changes the lattice constant of the underlying C_{60} crystal. K_3C_{60} has an fcc lattice structure with a lattice parameter $a = 14.24 \pm 0.01 \text{ \AA}$ [52, 57] — slightly larger than undoped C_{60} . Extending to other alkali-metal dopants produces a rich phase diagram (Fig. 2.6), with a superconducting dome bordered by a Mott insulating state, and a metallic state at higher temperatures. The insulating phase is characterised by anti-ferromagnetism in the A15 phase, and more complex magnetic behaviour

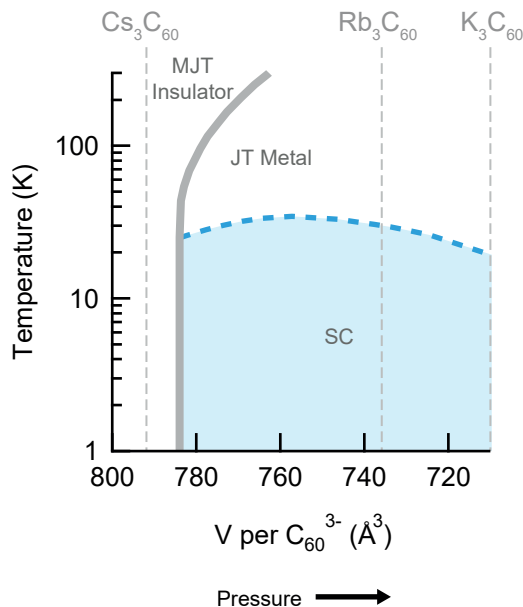


Figure 2.6: **Phase diagram of the alkali-doped fullerides.** The superconducting dome (SC) is shown in blue. Above is the Jahn-Teller (JT) metal phase, and to the left is the Mott-Jahn-Teller (MJT) insulating phase. Adapted from [59] and [61].

in the fcc phase [59]. The superconducting dome peaks at a temperature of 38 K, observed in Cs_3C_{60} under pressure [60].

2.2.1 Electronic properties

In C_{60} , the highest occupied molecular orbital (HOMO) is completely filled, making it a semiconductor with a bandgap of approximately 1.5 eV [63]. The lowest unoccupied molecular orbital (LUMO) is of t_{1u} symmetry [64], and originates from the π -orbitals. When doped into K_3C_{60} , the potassium dopant donates 3 electrons to the t_{1u} band, bringing it to half-filling and resulting in metallic behaviour [65]. The t_{1u} band has a bandwidth W of ~ 500 meV, and is triply degenerate at the Γ -point.

The band structure of K_3C_{60} , as calculated using density functional theory (DFT), is displayed in Fig. 2.7, alongside the density of states (DOS) at each energy. The bands are distinctly separated, which is typical of a molecular solid, where the neighbouring molecules have a relatively small overlap between orbitals. The next band, of t_{1g} symmetry, is found approximately 500 – 700 meV above the t_{1u} band.

Interestingly, although the half-filled t_{1u} bands are also present in Cs_3C_{60} , it is an insulator. The transition to insulating behaviour is widely considered to result from Mott localisation [66]. This makes sense when considering the effective correlation

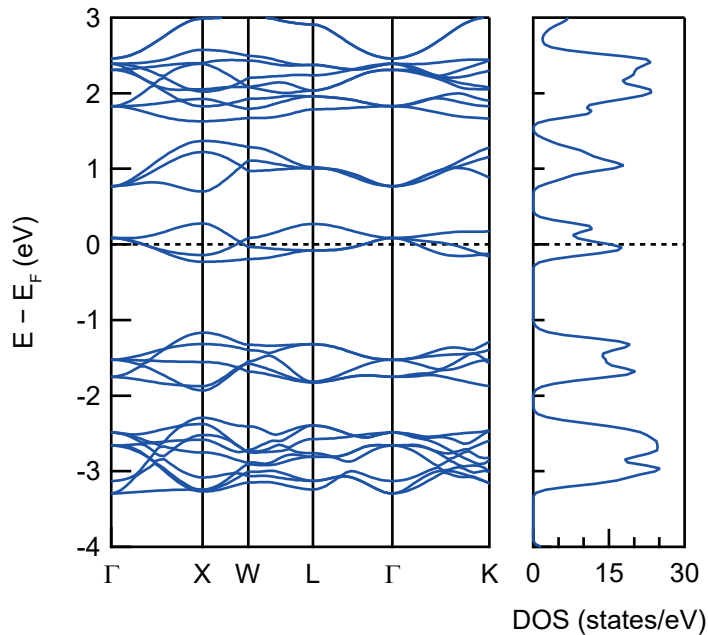


Figure 2.7: **Band structure and density of states of K_3C_{60} .** Data was obtained via DFT calculation based on the cuts shown in [62], and was kindly provided by Dr. Michael Fechner.

strength, given by U/W , where U is the on-site Coulomb repulsion energy. U has been found to be 1.6 ± 0.2 eV in undoped C_{60} [67], and 1.4 ± 0.2 eV in K_6C_{60} [68]. Experimental results and calculations outlined in Gunnarsson (2004) [69] put U/W in the range 1.5–2.5, confirming the importance of electronic correlations.

In contrast to other materials, the fullerides exhibit particularly large intramolecular phonon energies, owing to the light carbon nuclei and the large stiffness of the C_{60} molecules. Meanwhile, the conduction electron energy scale is reduced due to the low carrier density and reduced hopping energy [69]. This puts the electronic and nuclear dynamics on the same energy scales, leading to complex and interesting competing effects in this class of materials.

2.2.2 Superconductivity in the alkali-doped fullerides

Phenomenology of the superconducting state

As mentioned in section 2.2, superconductivity has been observed below a temperature of 19.3 K in K_3C_{60} [52, 58], and the temperature-pressure phase diagram reveals a superconducting dome that peaks at 38 K in high-pressure Cs_3C_{60} [60].

The alkali-doped fullerenes are type-II superconductors, and the superconductivity is widely considered to be s-wave in nature [70]. In K_3C_{60} , the lower critical field H_{c1} has been found in the range 7–13 mT [71, 72], and values for the upper critical field H_{c2} have been measured to be within 26–33 T [71, 73, 74]. The Ginzburg-Landau coherence length ξ_{GL} of K_3C_{60} has been measured in the range 26–32 Å [71, 72, 74, 75]. From these results, the London penetration depth $\lambda(0)$ has been estimated to be 250 nm [76] using the relation [43]

$$H_{c1} = \frac{\phi_0}{4\pi\lambda(0)^2} \ln \frac{\lambda(0)}{\xi_{GL}}, \quad (2.1)$$

where $\phi_0 = hc/e$.

Critical current densities at 0 K have been estimated at $3 \times 10^6 \text{ A cm}^{-2}$ [71] and $1 \times 10^6 \text{ A cm}^{-2}$ [77] from zero-temperature extrapolation of magnetic measurements.

Evidence for strongly correlated superconductivity

The combination of a Mott insulating phase and a superconducting dome is reminiscent of the cuprate superconductors [78], and suggests that strong electronic correlations also influence the superconducting state in the alkali-doped fullerenes. Both phononic [79–82] and electronic [83–85] mechanisms driving superconductivity have been proposed, but ultimately the mechanism of superconductivity remains unclear [76, 78].

The isotope effect can often provide information with regards to the mechanism of superconductivity. In BCS theory, for a system with a single type of ion of mass M , the transition temperature follows $T_c \sim M^{-\alpha}$, where $\alpha = 0.5$ [86]. Measurements of the carbon isotope effect in almost completely ^{13}C substituted K_3C_{60} have yielded $\alpha = 0.30 \pm 0.06$ [87]. This suggests that electron- C_{60} phonon coupling plays a role in superconductivity in the alkali-doped fullerenes. On the other hand, dopant isotope substitution in Rb_3C_{60} has yielded no evidence for a dopant isotope effect [88–90], and application of pressure to Rb_3C_{60} reduces its T_c to that of K_3C_{60} [57]. Both of these observations indicate that changes in the lattice parameter are the primary cause of the dopant material's influence on T_c [76].

When considering the influence of electronic correlations, interestingly, K_3C_{60} does not show signs of resistivity saturation even up to temperatures of 800 K, in violation of the Ioffe-Regel-Mott criterion, suggesting that the electronic scattering length is significantly smaller than the fcc lattice constant [69, 91, 92]. In addition,

in the metallic phase, close to the metal-insulator boundary on the A_3C_{60} phase diagram, the infrared spectrum resembles that of the neighbouring Mott phase [61]. This region has been referred to as a “Jahn-Teller metal” phase [78]. Capone and colleagues [93–95] have suggested that the proximity to the Mott transition results in electron-electron interactions being beneficial for superconductivity, rather than detrimental, and term the resulting state “strongly correlated superconductivity”. Furthermore, the effect of dynamical screening from nonlocal (intermolecular) Coulomb interactions was investigated by Nomura [96–98], and, by accounting for this, a quantitatively accurate phase diagram for the alkali-doped fullerenes could be reproduced.

2.3 Optical control of superconductivity in K_3C_{60}

Above-gap excitation of a superconductor is understood to break Cooper pairs and disrupt superconductivity [99], and this phenomenon has already found applications in single-photon detection [100, 101]. Meanwhile, there is also evidence that certain forms of excitation may lead to an enhancement of superconductivity. The first was found under sub-gap microwave excitation [102, 103], and was explained via an elevation of above-gap quasiparticles leading to an effective cooling of the system [43]. One of the most striking results, however, has been discussed under the term “light-induced superconductivity”, which was first demonstrated in the material $La_{1.8-x}Eu_{0.2}Sr_xCuO_4$ for a doping of $x = 0.125$ ($LESCO_{1/8}$) [30]. In this case, *above-gap* excitation, at temperatures above T_c , resulted in the emergence of superconducting-like optical features – a plasma edge was observed after excitation, accompanied by a divergence in the imaginary component of the conductivity. The proposed mechanism originated from the low-temperature tetragonal distortion in $LESCO_{1/8}$, a “striped” charge- and spin-order, that suppresses superconductivity [104]. By melting the competing stripe order via mid-infrared excitation, superconductivity could become energetically favourable.

Light-induced superconducting-like properties have since been observed in several systems, including other cuprates [31, 105–107], charge-transfer salts [108, 109], and the alkali-doped fullerenes [32, 33, 110, 111]. This section will summarise the results from optically-driven K_3C_{60} , in which excitation of K_3C_{60} powders with femtosecond, mid-infrared laser pulses gave rise to long-lived superconducting-like optical properties at temperatures well-above the equilibrium T_c . The observations were drawn from terahertz reflectivity measurements, which are briefly explained in the following.

2.3.1 Equilibrium optical properties

The optical response of a material contains information about conductivity, collective modes, and electronic and phononic excitations [112, 113], making it an excellent tool for understanding the properties of materials. This information manifests in the reflectivity and transmissivity of the material, and can be accessed with coherent laser pulses in the terahertz frequency range.

Reflectivity measurements were made on K_3C_{60} powders using picosecond terahertz pulses. From the reflectivity, the real and imaginary components of the optical conductivity (σ_1 and σ_2 , respectively) can be extracted. In the metallic phase above T_c , an optical response characteristic of a Drude metal is expected. In particular, the optical properties of a Drude metal obey the relation

$$\hat{\sigma}(\omega) = \frac{ne^2\tau}{m} \frac{1}{1 - i\omega\tau}, \quad (2.2)$$

where n is the charge carrier number density, m is the carrier mass, and $-e$ is the electronic charge. This can be decomposed into its real and imaginary components, with $\hat{\sigma}(\omega) = \sigma_1(\omega) + i\sigma_2(\omega)$, given by

$$\sigma_1(\omega) = \frac{ne^2\tau}{m} \frac{1}{1 + \omega^2\tau^2} \quad (2.3)$$

$$\sigma_2(\omega) = \frac{ne^2\tau}{m} \frac{\omega\tau}{1 + \omega^2\tau^2}. \quad (2.4)$$

In this model, the optical response is determined completely by the plasma frequency $\omega_p^2 = ne^2/m$ and the scattering rate $\gamma = 1/\tau$. For frequencies far below γ , σ_1 is frequency-independent, while for frequencies far above γ , σ_1 decreases as $1/\omega^2$. In σ_2 , there is a peak at a frequency of γ .

The equilibrium data from K_3C_{60} are displayed in Fig. 2.8 for temperatures above (red) and below (blue) T_c [32]. For temperatures above T_c , the drop-off in σ_1 extends out to 10 meV, while the Drude peak in σ_2 can also be seen at around 4 meV. Notably, a broad absorption peak has been observed, centred around 50 meV. The origin of this absorption is unclear [114–116], but a recent study proposes that it is an excitonic peak arising from strong band renormalization due to Jahn-Teller splitting [117].

For the case of superconductivity, the relevant frequency scale corresponds to the superconducting energy gap 2Δ . Below the gap frequency, several distinguishing features arise - the reflectivity increases to exactly 1, the real part of the conductivity reduces to exactly 0, and the imaginary part of the conductivity diverges in frequency

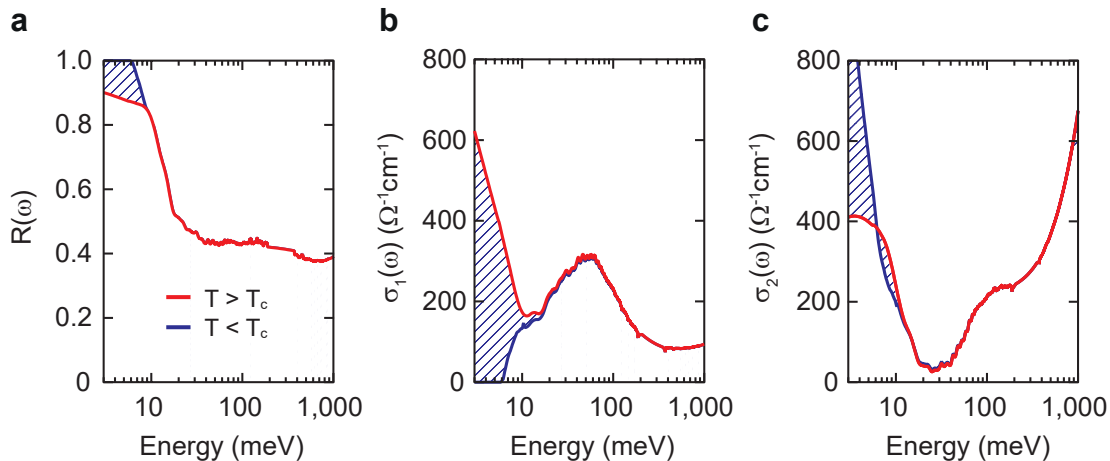


Figure 2.8: **Equilibrium optical properties of K_3C_{60} .** **a**, Reflectivity, **b**, the real component of the optical conductivity, and **c**, the imaginary component of the optical conductivity versus energy. Measurements are shown above T_c (red) and below T_c (blue). Figure reused from [32] with permission.

as $1/\omega$. Below T_c , the above-mentioned features of superconductivity emerged below a frequency of 6 meV, corresponding to previously measured values for the energy gap in K_3C_{60} [118, 119].

One way to understand the below-gap conductivity features in a superconductor is to extrapolate the Drude model to very long scattering times τ . In doing so, the cut-off frequency in σ_1 is reduced to zero, and the spectral weight is condensed to a delta peak at zero-frequency. For the imaginary component, we have

$$\sigma_2(\omega) \propto \frac{\omega}{1/\tau^2 + \omega^2}, \quad (2.5)$$

which approximates to a $1/\omega$ divergence for very large τ .

2.3.2 Photoinduced optical properties

The use of picosecond terahertz pulses allows for time-resolved measurements of the optical properties. Reflectivity measurements were also made before and after the incidence of a mid-infrared excitation pulse at a temperature of 100 K. By considering the pump and probe penetration profiles, the pump-induced optical features at the sample surface could be extracted, which are displayed in Fig. 2.9 [32]. The optical properties in equilibrium are shown in red. After incidence of the pump pulse, the optical properties of the excited state (blue) were found to resemble the equilibrium superconducting state. A gap emerged below ~ 10 meV, and the

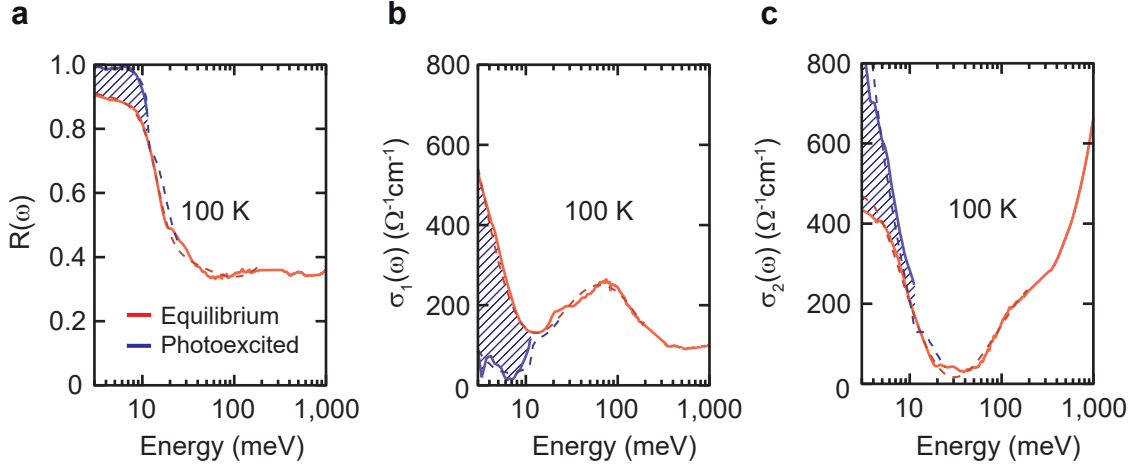


Figure 2.9: **Photo-excited optical properties of K_3C_{60} .** **a**, Reflectivity, **b**, the real component of the optical conductivity, and **c**, the imaginary component of the optical conductivity versus energy. Measurements are shown for a temperature of 100 K in equilibrium (red) and 1 ps after mid-infrared excitation (blue). Figure reused from [32] with permission.

divergent σ_2 indicated an extremely large carrier mobility. Together, these features suggested that a superconducting-like phase is induced by mid-infrared excitation of K_3C_{60} , even at temperatures far above its equilibrium T_c .

In this experiment, the photoinduced superconducting-like optical features were induced using a pump frequency of 43 THz with a fluence of 1 mJ cm^{-2} , and were observed to have a lifetime of $\sim 1 \text{ ps}$.

2.3.3 Tuning of the photoinduced state

The photoinduced optical properties of K_3C_{60} have been characterised by both their temperature [32] and pressure [110] dependencies, which are displayed in Fig. 2.10. The photoinduced changes were suppressed by both increasing temperature and increasing pressure, which followed the same trend as the equilibrium phase diagram for K_3C_{60} . In particular, the temperature dependence indicated a slow reduction, with indications of a partial photoinduced gap remaining present even at base temperatures up to room temperature. On the other hand, the photoinduced carrier mobility reduced sharply with increasing pressure, with a reduction of several orders of magnitude at 0.1 GPa, and saturating at $\sim 0.5 \text{ GPa}$. Conversely, the equilibrium state above T_c displayed an increase in carrier mobility with increasing applied pressure.

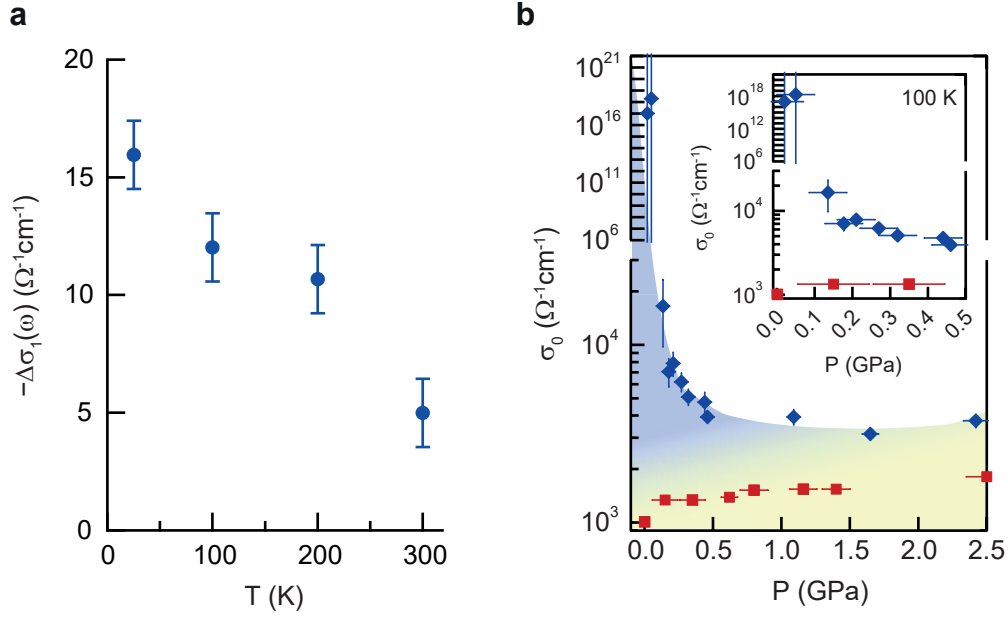


Figure 2.10: **Scaling of the photo-induced optical features.** **a**, Temperature dependence of the reduction in σ_1 . Adapted from [32] with permission. **b**, Pressure dependence of the extracted zero-frequency conductivity. The blue diamonds are zero-frequency conductivities extrapolated from Drude-Lorentz fits to the transient optical spectra. The red squares are the zero-frequency conductivities at equilibrium. The insets display a zoomed-in low-pressure region. Adapted from [110] with permission.

It was later shown that larger excitation fluences with longer pulses can extend the lifetime of the photo-excited state as far as 10 ns [33]. The optical measurements in this study were complemented by two-contact transport measurements on the long-lived effect in pressed pellet samples of K_3C_{60} . There, nanosecond current pulses were applied to the K_3C_{60} sample before and after incidence of the excitation pulse, from which the voltage drop across the device was measured. In these measurements, a large, non-metallic contact impedance needed to be subtracted under the assumption that the contact impedance was not affected by the excitation, which was calibrated through the use of a separate four-contact device. In the two-contact device, a reduction in voltage drop was measured upon photo-excitation, and this was found to be consistent with a completely vanishing sample resistance.

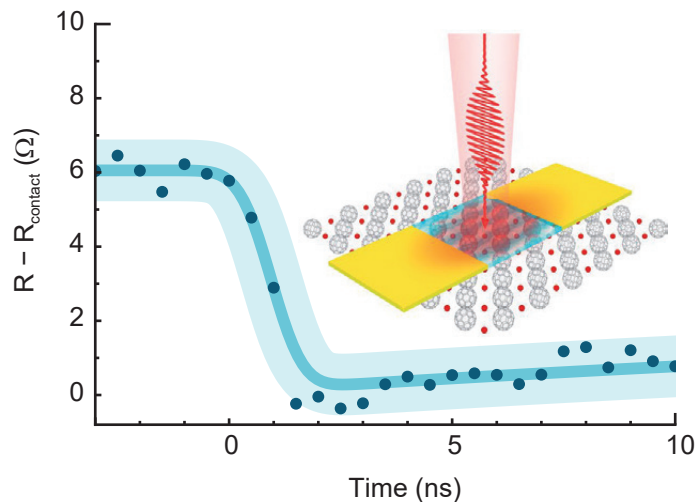


Figure 2.11: Nanosecond voltage pulse measurements of pressed K_3C_{60} powder. Reprinted from [33] with permission.

2.4 Proposal for an ultrafast transport experiment

Previous nanosecond transport measurements [33] served as a promising proof-of-concept for further experimentation on the photoinduced phase of K_3C_{60} . Challenges regarding the contact impedance at the sample and the timescale limitations of nanosecond pulses can be overcome through the use of K_3C_{60} *thin films*, which also enable the use of much larger current densities. This thesis will outline a series of transport experiments on K_3C_{60} thin films, which were incorporated into devices based on terahertz transmission lines and photoconductive switches. The high-bandwidth transmission lines and photoconductive switches allow for the generation and detection of currents and voltages on picosecond timescales, representing an improvement of three orders of magnitude over the previous transport measurements.

An ultrafast transport device incorporating a K_3C_{60} thin film presents multiple experimental possibilities, which are outlined in Fig. 2.12. In Fig. 2.12a, an on-chip terahertz spectroscopy measurement is illustrated. This experiment makes use of launched picosecond current pulses, which are incident on the K_3C_{60} thin film. The reflected and transmitted pulses can then be detected to extract information about the complex impedance of the sample on picosecond timescales. Since larger current densities can be applied to a thin film sample, the critical current of the equilibrium superconducting state can also be reached in this geometry. This enables the possibility to increase the magnitude of the incoming current pulses and search

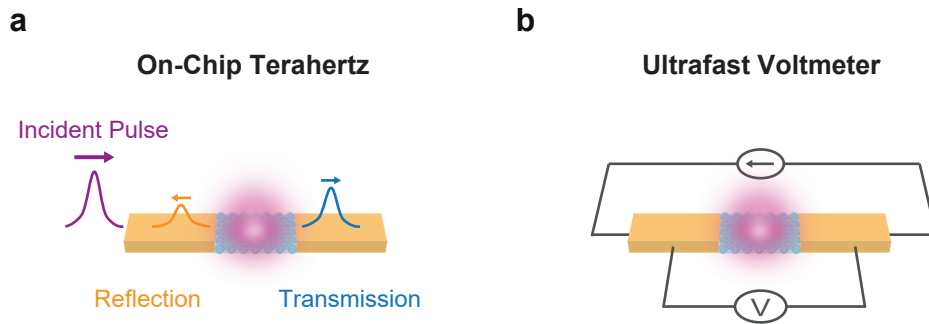


Figure 2.12: **Proposal for picosecond transport measurements.** **a**, Sketch of an on-chip terahertz experiment. Picosecond current pulses are launched towards the sample, and the reflected and transmitted pulses provide a snapshot of the transport properties. **b**, Sketch of an ultrafast voltmeter measurement. A DC bias is applied to the sample. Photo-excitation alters the sample properties, resulting in a dynamical voltage.

for nonlinear current voltage behaviour in the photo-excited regime of K_3C_{60} .

A second experimental configuration is illustrated in Fig. 2.12b, where the device is operated as an “ultrafast voltmeter”. In this geometry, a DC current can be applied from an external source, and voltage changes upon photo-excitation of the K_3C_{60} can be detected. Since the properties of the K_3C_{60} would change in the presence of a bias, the induced voltage dynamics can provide insight into the fast carrier dynamics upon photo-excitation, and potentially allow time-varying inductances to be observed.

In the following chapters, we will explore how a device can be realised to conduct both of these measurements, and outline the process of incorporating thin films of K_3C_{60} .

Chapter 3

Ultrafast electronic transport

3.1 High-frequency transmission lines

In order to measure changes in transport properties on picosecond timescales, current pulses with frequency content in the terahertz regime need to be detectable. However, when increasing frequencies propagate through a simple wire, the movement of charges creates excitations in the free-space electromagnetic field [120], and energy is lost through emission of electromagnetic waves. As such, high-frequency spectral content, and therefore time-resolution, is lost. To overcome this, the electromagnetic fields can be confined in a *transmission line* geometry. Transmission lines offer an advantage over free-space optics for their ability to confine low-frequency fields even below the diffraction limit [37]. This is particularly useful in the case of ultrafast phenomena, which are often driven by strong optical excitation, requiring in most cases large pump-fields and therefore small pump spot sizes. Additionally, most transmission lines have no low frequency cut-off, enabling the propagation of signals down to the DC regime [35].

Transmission lines come in many forms, and the properties of the transmission line are heavily dependent on its geometric parameters [35]. Some of these forms are illustrated in Fig. 3.1. The most common is the coaxial cable (Fig. 3.1a), consisting of a central conduction wire surrounded by a cylindrical ground line. Panels b, c, and d display a microstrip, coplanar strip, and coplanar waveguide, respectively. The microstrip consists of a conduction line separated from a ground plane by a dielectric material. Here, the electric field is primarily distributed within the dielectric, resulting in a uniform dielectric constant. The following two geometries are planar, where the field lines pass through both air and substrate. The non-uniform dielectric must be accounted for, but this can lead to a smaller *effective* dielectric constant. In the coplanar strip, the electric field lines run from one conductor to the other and are distributed mainly along the surface of the substrate. This is the

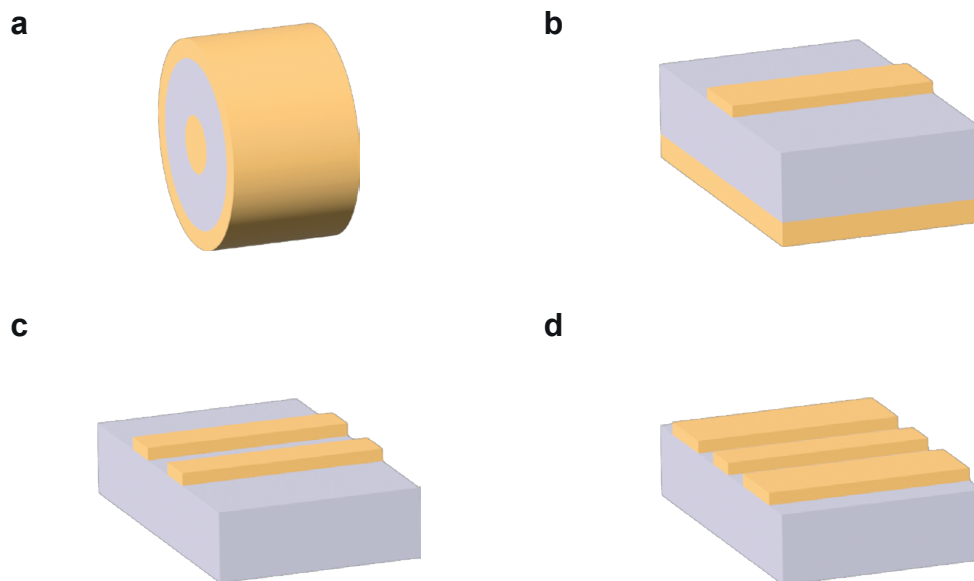


Figure 3.1: **Some transmission line geometries.** **a**, Coaxial cable. **b**, Microstrip. **c**, Coplanar strip. **d**, Coplanar waveguide.

same for the coplanar waveguide, except in this case there is a central conduction line that allows for the propagation of symmetric modes. In both of these cases, device fabrication is simpler due to the planar geometry. The coplanar waveguide will be discussed in more detail in section 3.1.2.

3.1.1 Telegrapher's equations

Transmission lines can be generally represented by the circuit displayed in Fig. 3.2. In this circuit representation an infinitesimal slice of a transmission line is considered, with length dz . Losses in the conductors are described by the resistance per unit length R , and losses in the dielectric medium between the conductors are captured in the conductance per unit length G . The inductance per unit length of the line is given by L , and the capacitance per unit length between the conduction line and the ground is given by C . Kirchoff's laws allow us to derive the equations of motion for the transmission line, known as the “telegrapher's equations” [112]. The changes in voltage $V(z, t)$ and current $I(z, t)$ when comparing two points on the line with infinitesimal separation δz are given by

$$V(z + \delta z, t) - V(z, t) = - \left\{ RI(z, t) + L \frac{\partial I(z, t)}{\partial t} \right\} \delta z \quad (3.1)$$

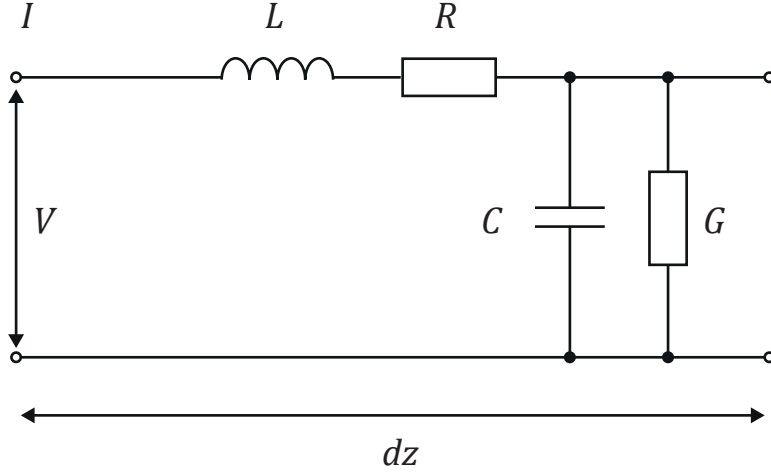


Figure 3.2: **Circuit representation of a transmission line.** The resistance and inductance of the conductor are represented in the top line. The two lines are connected together via the capacitance and admittance across the dielectric region.

$$I(z + \delta z, t) - I(z, t) = - \left\{ GV(z, t) + C \frac{\partial V(z, t)}{\partial t} \right\} \delta z. \quad (3.2)$$

It follows that

$$-\frac{\partial V(z, t)}{\partial z} = RI(z, t) + L \frac{\partial I(z, t)}{\partial t} \quad (3.3)$$

$$-\frac{\partial I(z, t)}{\partial z} = GV(z, t) + C \frac{\partial V(z, t)}{\partial t}. \quad (3.4)$$

These can be rearranged to get separate equations for the voltage and current:

$$\frac{\partial^2 V(z, t)}{\partial z^2} = RG \cdot V(z, t) + (RC + LG) \frac{\partial V(z, t)}{\partial t} + LC \frac{\partial^2 V(z, t)}{\partial t^2} \quad (3.5)$$

$$\frac{\partial^2 I(z, t)}{\partial z^2} = RG \cdot I(z, t) + (RC + LG) \frac{\partial I(z, t)}{\partial t} + LC \frac{\partial^2 I(z, t)}{\partial t^2}. \quad (3.6)$$

A set of solutions to these equations is given by

$$V(z, t) = V_0 \exp[-i\omega t] \exp \left[\pm [(R - i\omega L)(G - i\omega C)]^{1/2} z \right] \quad (3.7)$$

$$I(z, t) = I_0 \exp[-i\omega t] \exp \left[\pm [(R - i\omega L)(G - i\omega C)]^{1/2} z \right], \quad (3.8)$$

where we can define a “propagation constant” k given by

$$k = [(R - i\omega L)(G - i\omega C)]^{1/2}, \quad (3.9)$$

which can also be written in the form

$$k = k_1 + ik_2. \quad (3.10)$$

We consider the rightward propagating wave, thereby taking only the negative form of the second exponent. If we insert these solutions into equations 3.3 and 3.4, we obtain

$$V = \left[\frac{R - i\omega L}{G - i\omega C} \right]^{1/2} I. \quad (3.11)$$

From the ratio of the voltage to the current we can obtain the characteristic impedance of the waveguide, given by

$$\hat{Z} = \left[\frac{R - i\omega L}{G - i\omega C} \right]^{1/2}. \quad (3.12)$$

This parameter turns out to provide most of the information that one needs when analysing a transmission line [112], and will prove to be important in the coming chapters.

3.1.2 Coplanar waveguide

The coplanar waveguide (CPW) offers several benefits that make it a valuable choice for our ultrafast electronic measurements: First, at high frequencies, the electric field is tightly confined within the slots, enabling high-bandwidth, ultrashort electromagnetic pulses to propagate with low dispersion [121, 122]. Second, the geometry allows for tunability of the characteristic impedance and bandwidth, and the substrate can be arbitrarily thick, simplifying fabrication [123].

The fundamental mode of the CPW (Fig. 3.3a) is described as a quasi-TEM mode, since the magnetic field possesses an out-of-plane component [35, 124]. We will refer to this mode as the “even” mode, since the electric field distribution is symmetric about the center of the signal line. Another mode is illustrated in Fig. 3.3b, and will be referred to as the “odd” mode. Higher order modes can also be excited in this geometry. Notably, different modes can have different propagation velocities, and a superposition of modes can be present in the transmission line [121].

The CPW, with roughly half of the field being inside the dielectric substrate, and the other half in free space, can be approximated as being totally immersed in a dielectric with an effective dielectric constant ϵ_{eff} given by

$$\epsilon_{\text{eff}} = \frac{1 + \epsilon_r}{2}, \quad (3.13)$$

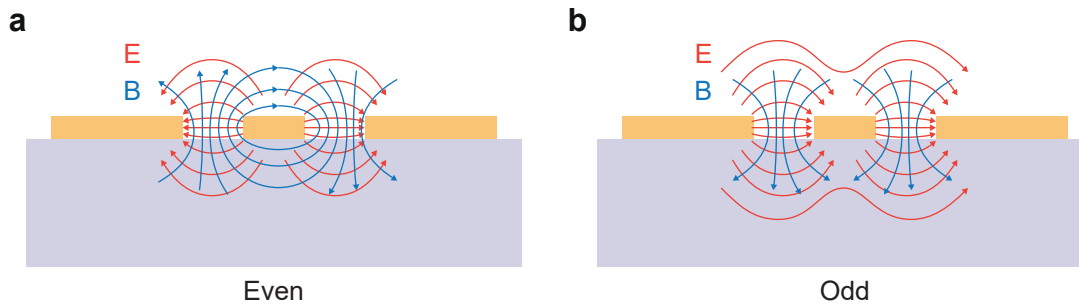


Figure 3.3: **Electromagnetic fields in a coplanar waveguide.** In-plane electromagnetic field components in the coplanar waveguide. **a**, The quasi-TEM (even) mode. **b**, The asymmetric (odd) mode. The electric field is represented in red, and the magnetic field in blue. In both cases, the magnetic field has a small out-of-plane component [35].

where ε_r is the relative dielectric constant of the substrate [124]. The phase velocity v_p of the fundamental mode is therefore given by

$$v_p = \left(\frac{2}{1 + \varepsilon_r} \right)^{1/2} c, \quad (3.14)$$

where c is the speed of light in vacuum. If we consider a coplanar waveguide on a sapphire substrate, where $\varepsilon_r = 9.54$, we obtain $v_p = 0.44c$.

3.2 Ultrafast photoconductive switches

We can achieve the confined propagation of high-frequency electrical signals with a transmission line, but measurements of ultrafast transport dynamics also require ultrafast generation and sampling of these electrical signals. This is possible using a photoconductive switch, which was first demonstrated by D. H. Auston in 1975 [4]. Photoconductive switches consist of a patch of semiconducting material — some frequently-used materials are silicon [4] or gallium arsenide [125, 126] — contacted to two wires, as illustrated in Fig. 3.4a. When a bias is applied to the wire, current flow is negligible; the switch is in the OFF state. However, when a laser pulse with photon energy above the band gap is incident on the switch, it excites photocarriers into the conduction band. These carriers now have states available for transport to occur, so the switch becomes conductive, or switched into the ON state, and current can flow (Fig. 3.4b). The current can flow only until the photocarriers relax back into the valence band. A biased switch will therefore launch a current pulse when excited, behaving as a current source [14]. The pulse duration is determined by

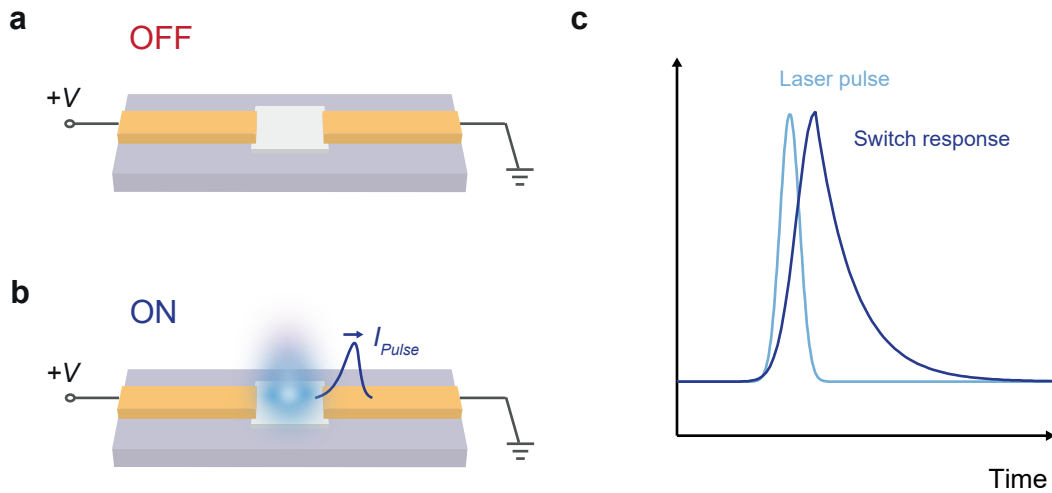


Figure 3.4: **Photoconductive switches.** **a**, Photoconductive switch in the OFF state. **b**, Photoconductive switch in the ON state, during excitation with a laser pulse in the visible range. When excited under an applied bias V , the switch launches a picosecond current pulse. **c**, Time profile of the current pulse. The rise time relates to the laser pulse duration. The decay time corresponds to the carrier lifetime in the switch material.

both the duration of the exciting laser pulse and the photocarrier relaxation time (Fig. 3.4c).

The bias does not need to be an applied DC voltage, but could also be a fast-changing, transient voltage that we would like to detect. In this case, the launched current pulse becomes the correlation of the transient voltage with the switch response function. If we consider a typical pump-probe configuration, with many laser pulses and transient voltages occurring at a fixed repetition rate, a simple measurement of the average current at the output of the photoconductive switch allows us to acquire a snapshot of the transient voltage. By taking many measurements of the total charge, and varying the mutual time delay between the transient voltage and the switch excitation pulse, we can acquire a time-resolved profile of the transient voltage.

A combination of current pulse generation and transient voltage detection are demonstrated with a simple experiment. The configuration for this experiment is displayed in Fig. 3.5a, where multiple photoconductive switches are connected to a coplanar waveguide. A DC bias is applied to switch 1, and switch 2 is connected to a transimpedance amplifier followed by a lock-in amplifier. Laser pulses are used to excite switch 1 and launch current pulses into the CPW, which carry an equivalent voltage given by $V(t) = I_{Pulse}(t)\hat{Z}$. This voltage is then detected at switch 2, and the voltage profile is measured by varying the mutual time delay between the excitation laser pulses for switch 1 and switch 2 (Fig. 3.5b). In this case, the

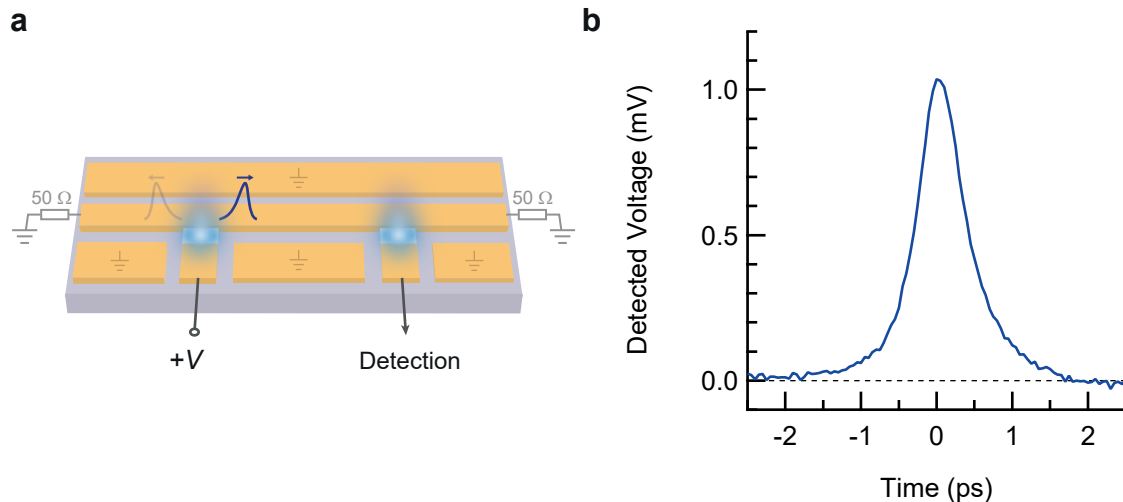


Figure 3.5: **Launching and detecting a current pulse.** **a**, Experimental setup. Pulses are launched from the leftmost switch, and detected using the switch on the right. **b**, Detected voltage versus time, measured by varying the delay between the launching laser pulse and the detection laser pulse. The FWHM is 1 ps.

measured voltage profile is the correlated response functions for the two switches.

A biased switch excited in this geometry (perpendicular to the signal line) launches current pulses in both signal line directions. In principle, by appropriately terminating the transmission line with a matched impedance, in this case $50\ \Omega$, only the rightward-travelling pulse is detected. In practice, it is difficult to impedance-match the connections between the device and the external electronics, and the presence of other switches can also interrupt the signal line. When considering reflections from these boundaries, the leftward-travelling pulse can therefore become important, as will be discussed in section 3.3.4.

3.2.1 Tuning the pulse amplitude

When using current pulses as a probe, it is desirable to have in-situ control over the magnitude of the launched current pulse. As mentioned, the launched current is dependent on the bias voltage — Fig. 3.6 displays the raw detected voltage for the cross-correlation of two photoconductive switches for bias voltages in the range 2–100 V. Notably, the form of the current pulse remains unchanged within this voltage range (Fig. 3.6a), while the magnitude increases linearly with the applied voltage (Fig. 3.6b).

The voltage cannot be increased indefinitely. Once the dielectric breakdown field of the semiconductor is reached, electronic ionisation interactions overwhelm electron-

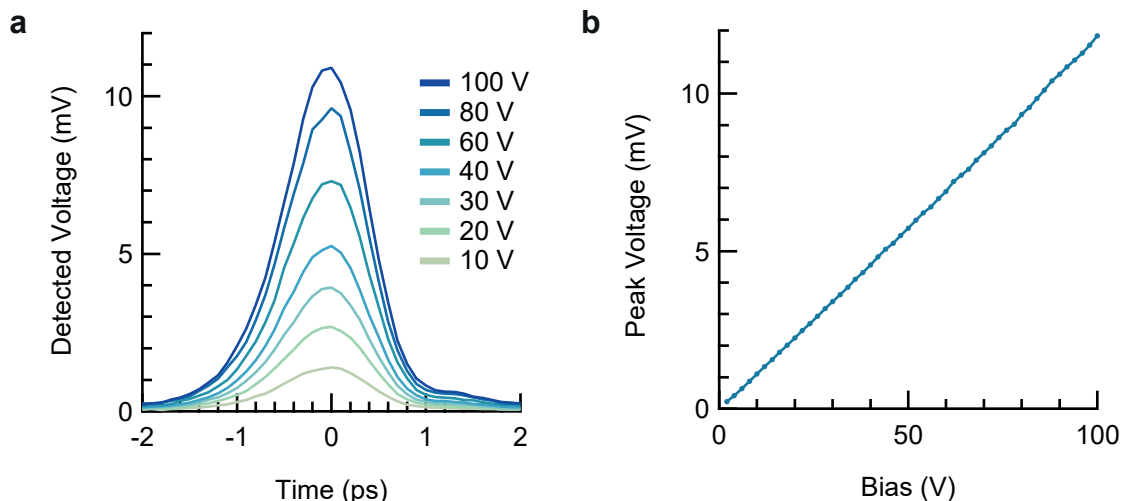


Figure 3.6: **Switch bias dependence.** **a**, Switch correlation measurements for biases 10–100 V. **b**, Peak of the switch correlation versus bias.

lattice interactions and the resistance of the semiconductor decreases sharply [127–129]. To achieve even higher peak currents in the launched pulses, the excitation fluence can also be increased. A larger number of photons will result in more photocarriers and also increase the magnitude of the pulse. In Fig. 3.7a, we can see that increasing the fluence of the excitation pulse does not change the shape of the launched pulse up to at least 1.6 mJ cm^{-2} . Fig. 3.7b displays the peak of the detected voltage as a function of fluence, and no saturation was observed in the measured fluence range.

3.2.2 Pulse duration

Characterising the lifetime of the photo-excited carriers in the switches is necessary to determine the time resolution of the ultrafast voltage measurements. There are a few techniques that can be used to do this. The lifetime can be determined optically by measuring the reflectivity of the photo-excited switches [130, 131], or determined directly on the chip. The on-chip method requires two switches situated opposite one another, as depicted in Fig. 3.8a. Here, switch 1 is biased with a voltage and excited with a pulse of 515 nm light, launching a voltage pulse into the signal line. The opposite switch, switch 2, is used as the detection switch by exciting it with a second laser pulse. By adjusting the time delay between the two laser pulses, a voltage versus time profile can be obtained — data obtained in this geometry on a full device is shown in Fig. 3.8c. This represents the correlation of the switch response functions for switches 1 and 2. Since the switches are so close to one

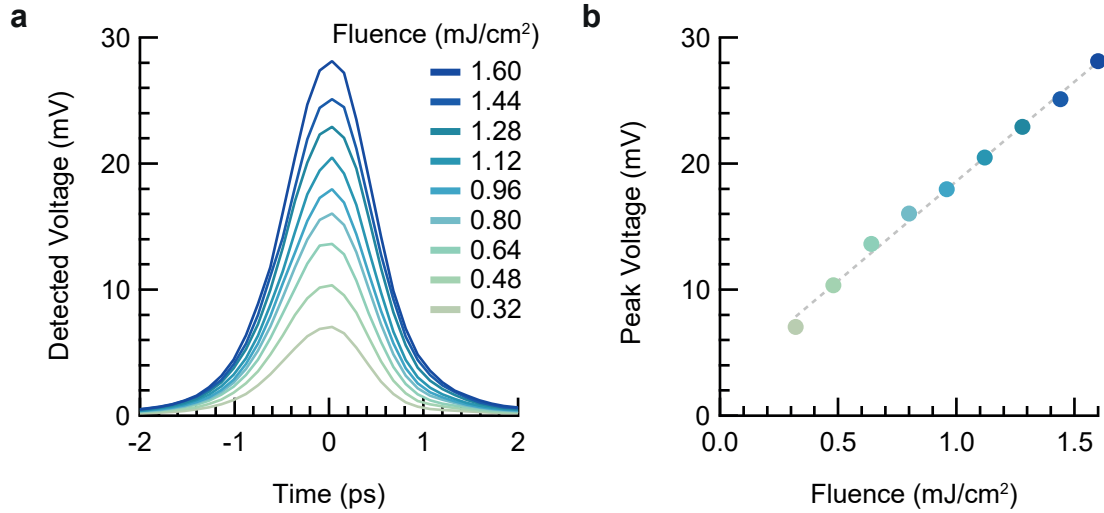


Figure 3.7: **Switch fluence dependence.** **a**, Switch correlation measurements for fluences $0.32 - 1.60 \text{ mJ cm}^{-2}$. **b**, Peak of the switch correlation versus fluence.

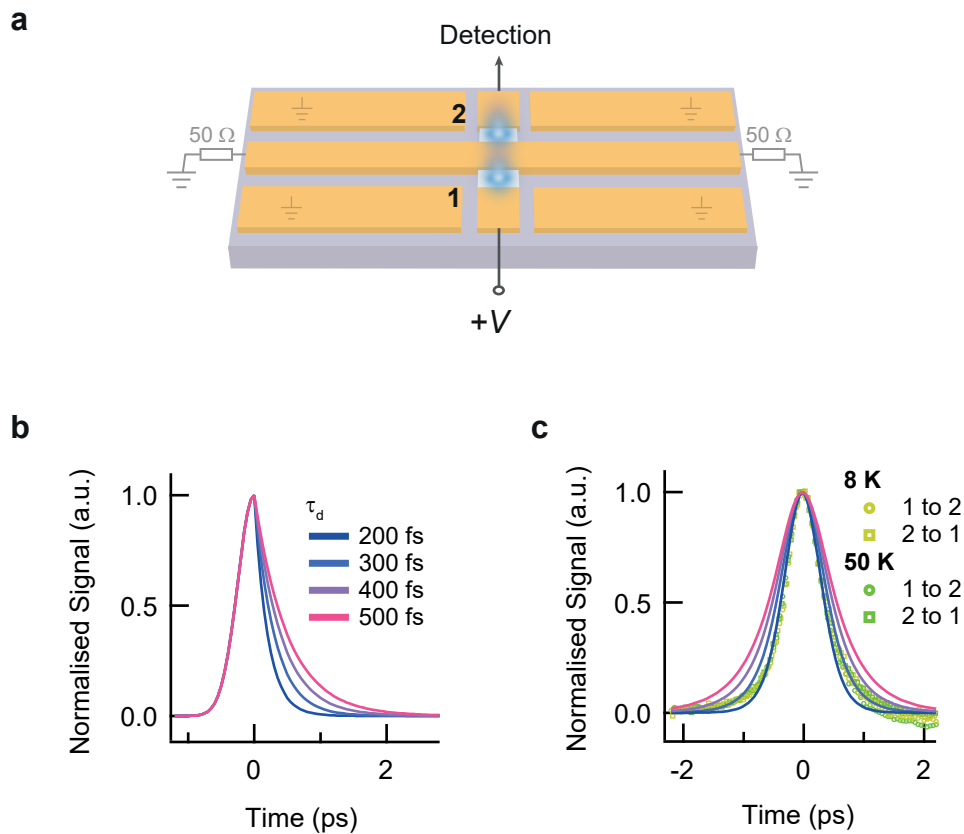


Figure 3.8: **Determining the photocarrier lifetime.** **a**, Measurement setup. A DC voltage bias was applied to one switch, and the launched pulses were detected using the opposite switch. **b**, Switch response functions for different exponential decay constants τ_d . **c**, Autocorrelation of the switch response functions in (b), compared with the measured data when launching from different switches.

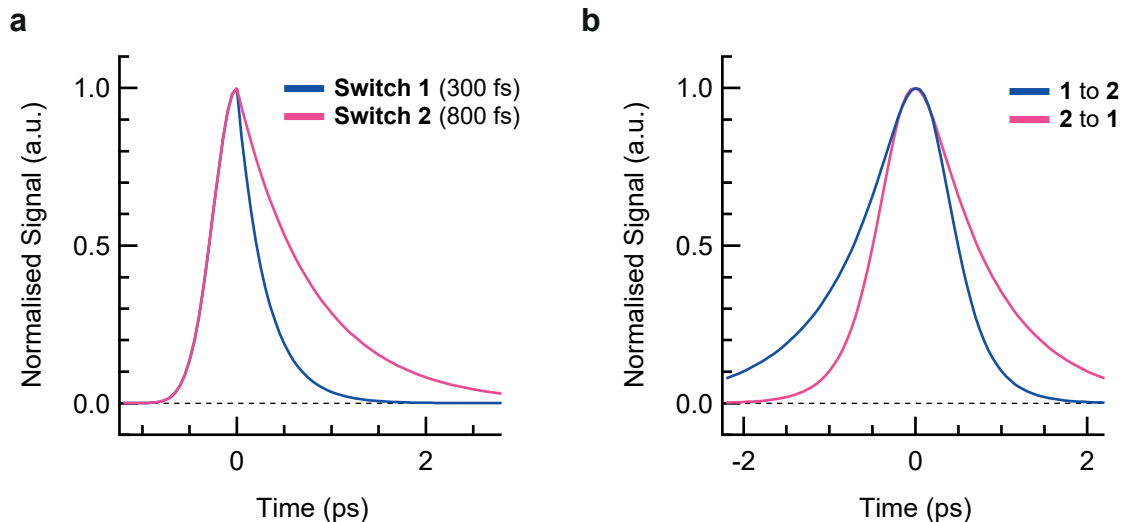


Figure 3.9: **Asymmetric behaviour in switches with different carrier lifetimes.** **a**, Switch profiles for a decay time of 300 fs for switch 1 (blue) and 800 fs for switch 2 (pink). **b**, Correlation of the two different switch profiles, simulating launching at switch 1 and detection at switch 2 (blue), or launching at switch 2 and detection at switch 1 (pink). If the two switches have different carrier lifetimes when conducting the measurement in 3.8, an asymmetric form would be observed, as simulated here.

another, we minimise pulse dispersion in the waveguide and obtain a more accurate measurement of the response function correlation.

A model switch response is used to fit the experimental data, where the response has an error-function rise and exponential decay. The rise time is determined by the duration of the excitation laser pulse of 250 fs, and the decay time is determined by the lifetime of the photo-excited carriers. Model switch response functions for different decay times are displayed in Fig. 3.8b. By taking the autocorrelation of these response functions and comparing them with the measured data, an estimate of the decay time and therefore an appropriate switch response function can be obtained. In this case, a decay time of 300 fs provides the best fit to the data.

The correlation alone cannot differentiate between the response functions of switches 1 and 2, which are not necessarily identical as the switches can differ in their photocarrier relaxation times. This may arise due to various factors affecting silicon growth during device fabrication, such as inhomogeneities in substrate surface quality or temperature during silicon deposition. Significant differences in switch response functions can be diagnosed by making an additional correlation measurement in the reverse direction, i.e. by applying a bias to switch 2 and detecting the voltage at switch 1. If one switch has a longer decay time, reversing the measurement would skew the correlated trace. A simulation of this is displayed in Fig. 3.9, with two differing switch responses shown in Fig. 3.9a, and their correlations for both directions

in Fig. 3.9b. When switch 2, with the longer decay time, acts as the gate, the rise time of the pulse launched by switch 1 appears broadened due to the long tail of the gate. In the reverse situation, where the gate has a fast decay, the broadening of the rise is reduced. In the experimental data, this is not the case, justifying the assumption that the switch responses do not differ significantly.

3.3 Device design considerations

3.3.1 Sample placement

The placement of the sample strongly affects how it interacts with the electromagnetic fields and currents within the transmission line. Fig. 3.10 shows several different possibilities in various transmission line geometries. In Fig. 3.10a, a sample is situated within a coplanar strip. Here, the sample interacts directly with the electric field between the two conduction lines. Such a geometry has previously been employed to conduct on-chip terahertz spectroscopy measurements in directly coupled [37] and capacitively coupled [38, 39] regimes.

Fig. 3.10b illustrates a coplanar waveguide with the sample incorporated into the central conduction line. In this geometry, charge can be injected directly into the sample. By ensuring that the sample has the same width as the signal line of the CPW, the interaction of the sample with the terahertz electric field is reduced, and experiments can be carried out that focus mainly on the charge transport. In the work described here, the inline CPW geometry shown in Fig. 3.10b was used.

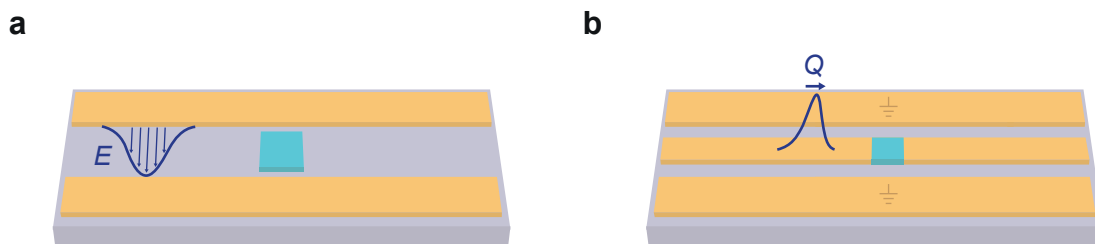


Figure 3.10: **Sample placement configurations.** **a**, Coplanar strip geometry, with the sample placed between the two conductive lines. The electric field E is incident on the sample. **b**, Coplanar waveguide geometry, with the sample incorporated inline into the central conduction line. A charge Q is incident on the sample.

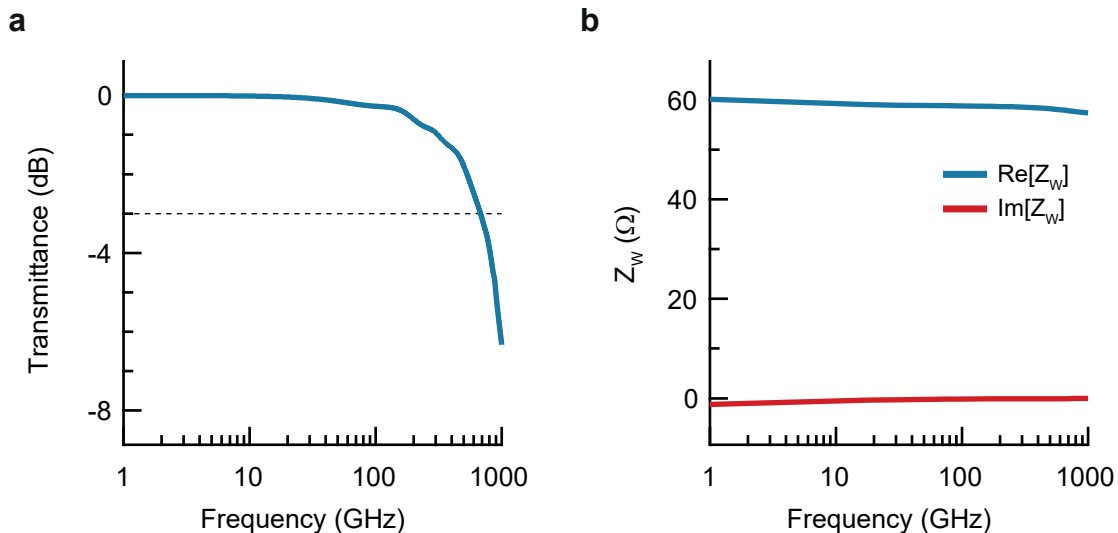


Figure 3.11: **Waveguide characterisation.** **a**, Transmittance versus frequency of a 200 μm -long waveguide, with 20 μm signal line width and 10 μm gap width. **b**, Real and imaginary components of the impedance for the same waveguide. Data was obtained from simulations in CST and kindly provided by Dr. Toru Matsuyama.

3.3.2 Waveguide dimensions

The waveguide dimensions have a significant impact on the quality of the propagating mode. In particular, a wider gap and signal line result in increased radiative losses and encourage the formation of higher-order waveguide excitations [132]. Narrower gaps can increase the bandwidth of the waveguide, but reducing the width of the conduction line can increase dissipation due to skin-depth effects [132]. In this work, a 20 μm signal line width and 10 μm gap width were used.

The transmittance and wave impedance of a coplanar waveguide with a 20 μm signal line width and 10 μm gap width were determined through simulations that were carried out in CST Studio Suite. The simulated frequency-dependent transmittance of a 200 μm -long waveguide is displayed in Fig. 3.11a, where the transmittance can be seen to drop off sharply at high frequencies, with the -3 dB point at approximately 700 GHz.

The real and imaginary components of the wave impedance are displayed versus frequency in Fig. 3.11b, and do not vary significantly in the 50 GHz–1 THz range. The real component $\text{Re}[Z]$ is approximately 59 Ω and the imaginary component $\text{Im}[Z]$ is less than 0.2 Ω , and can therefore be neglected in later calculations.

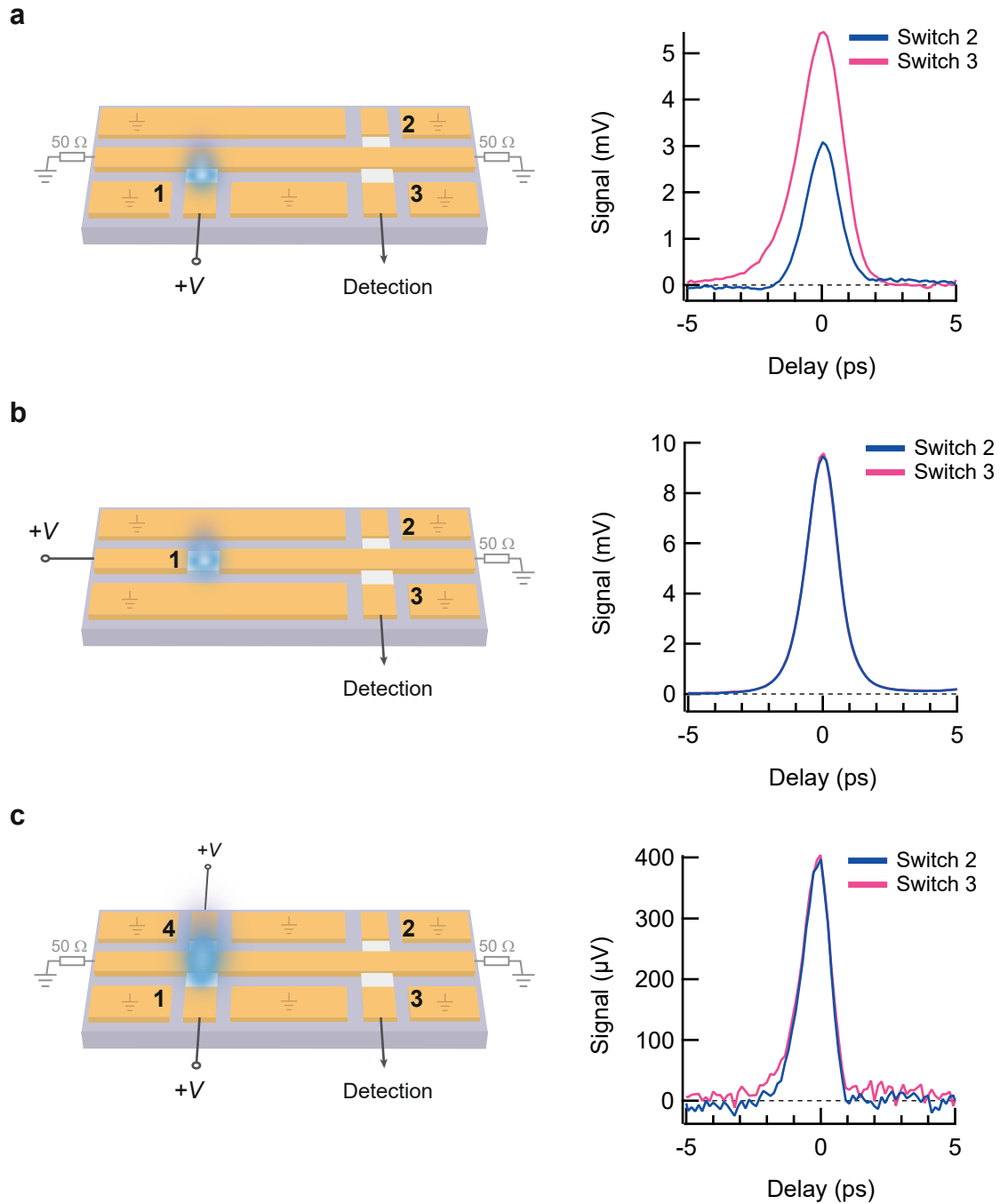


Figure 3.12: **Pulse launching configurations.** **a**, Asymmetric configuration. Pulses are launched from switch 1, which is connected to the side of the coplanar waveguide. The detected pulses at switches 2 and 3 are different, indicating that the electric field in the gap is asymmetric. **b**, Symmetric (but impractical) launch configuration, placing the launching switch (1) in the signal line. The detected pulses at switches 2 and 3 are the same for this configuration. **c**, Symmetric and practical launching configuration. Switches 1 and 4 are biased with an equal voltage, and excited with a laser pulse simultaneously. The detected pulses at switches 2 and 3 are the same for this case, indicating that the waveguide is excited symmetrically.

3.3.3 Launching a symmetric mode

In section 3.1.2, we saw that a superposition of modes can propagate in the coplanar waveguide. If the even and odd modes shown in Fig. 3.3 are both present, then the electric field on either side of the CPW will be different. An asymmetric electric field distribution makes it difficult to calibrate the voltages and currents propagating in the signal line from the measured data, since we obtain different signals from different switches. Ideally, we would like to excite only the fundamental mode of the CPW. Here, several different pulse launching geometries were tested by measuring the launched pulses on each side of the CPW.

The first geometry is shown in Fig. 3.12a, alongside measurements from a test device with an equivalent configuration. Pulses were launched from switch 1 and detected at switches 2 and 3. Data from each of the switches 2 and 3 were normalised by the sensitivity of the respective switches, allowing the measurements to be compared on the same scale. The measured signal at switch 2 was significantly smaller than the signal from switch 3, which is indicative of an asymmetric electric field distribution.

In the second geometry, displayed in Fig. 3.12b, the device itself was symmetric about the signal line of the CPW. Similarly to before, pulses were launched from switch 1, and detected at switches 2 and 3. In this case, the scaled measurements at switches 2 and 3 were identical, indicating a symmetric pulse. Although this is good, this device configuration introduces another issue, namely that DC transport in the signal line is inhibited by switch 1.

Fig. 3.12c introduces a geometry with a clear signal line and a symmetric photoconductive switch configuration, in order to launch symmetric pulses while preserving the DC conductivity of the signal line. Here, two opposing switches 1 and 4 were connected to the sides of the signal line. These were biased simultaneously with the same voltage, and excited with a single, large-area laser pulse. The measured signal magnitudes at switches 2 and 3 were found to be equal in this practical geometry, although the total amplitude was slightly reduced due to the increased laser spot size. The device design featured in the rest of this work features this setup utilising pairs of photoconductive switches.

3.3.4 Internal reflections

Although the switch configuration introduced in Fig. 3.12c does not interrupt the central conductor of the CPW, the switches still protrude into the gaps between the

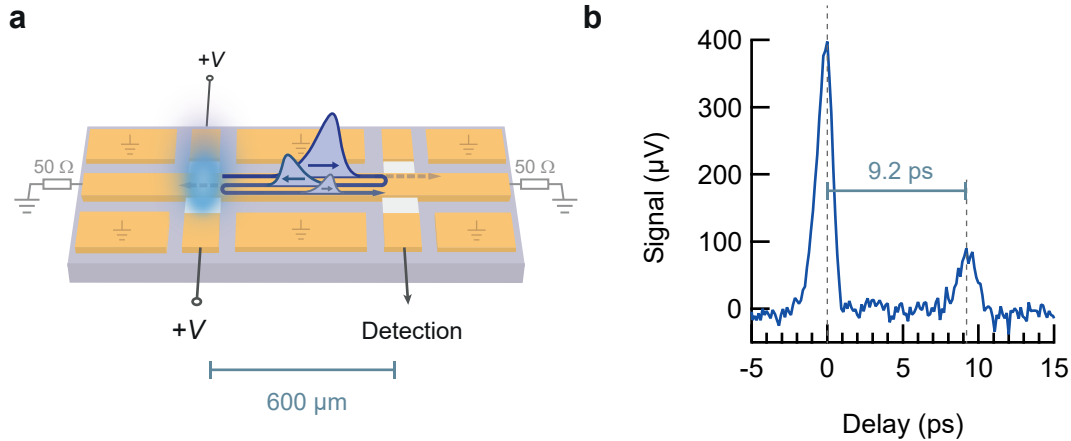


Figure 3.13: **Reflections from photoconductive switches.** **a**, Illustration of a coplanar waveguide geometry, with pulses launched from the leftmost pair of switches. The pulses travel to the right pair of switches, which are used for detection. Partial reflections result in additional pulses arriving at the detection switch at later times. **b**, Experimental data from the configuration depicted in (a). The reflected pulse arrives 9.2 ps after the launched pulse.

signal line and ground planes. This affects the wave impedance at these locations, resulting in partial reflection of travelling pulses. The sample also has an impedance mismatch with the waveguide, and can itself partially reflect pulses. Not only is the launched pulse measured at the detection switch, the partially reflected pulses are also measured at later times, and can interfere with the signal that we want to detect. A simplified example is illustrated in Fig. 3.13.

The signal and reflections should be separated in time as much as possible, which is achieved by increasing the distance between pairs of photoconductive switches. The pulses propagate with an on-chip speed of $0.44c$, which is approximately equivalent to $130 \mu\text{m ps}^{-1}$. Considering that a reflected pulse must travel away from the detection switch and then return to it, the photoconductive switches must be separated by $260 \mu\text{m}$ in space to separate the pulses by 4 ps in time.

Chapter 4

Device construction

This chapter will describe the important steps in realising the previously-described ultrafast optoelectronic circuitry, including the incorporation of K_3C_{60} to build the experimental device.

An examination of nonlinear current-voltage characteristics in K_3C_{60} requires that the critical current density of $\sim 1 \text{ GA m}^{-2}$ in the equilibrium superconducting state is accessible. For a square sample in a $10 \mu\text{m}$ wide signal line, an accessible critical current on the order of several milliamperes necessitated a sample thickness of approximately 100 nm . Such thin samples are not achievable with the powders or pellets used in previous experiments on photo-excited K_3C_{60} . Instead, thin-films of K_3C_{60} were grown via molecular-beam epitaxy (MBE).

Section 4.1 will outline the microstructuring process to build the optoelectronic devices. This consisted of a photo-lithography, thermal evaporation, and lift-off procedure. Next, the MBE growth procedure for the K_3C_{60} is explained in section 4.2, followed by the incorporation of the K_3C_{60} into the ultrafast transport devices in section 4.3. The device properties are then discussed via the characterisation of test circuits. The resulting device architecture was used in the two experiments described in Chapters 5 and 6.

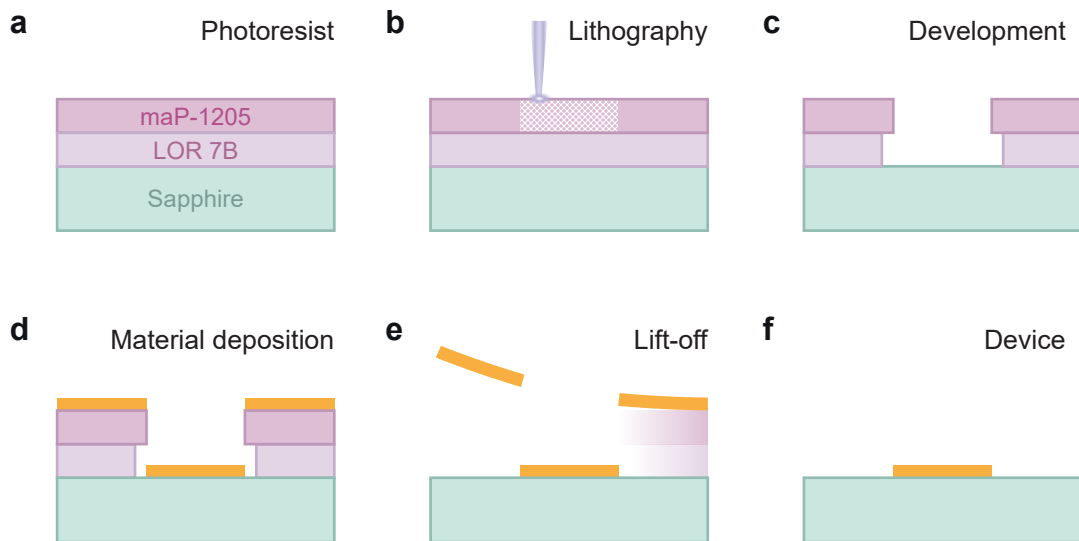


Figure 4.1: **Photolithography process.** **a**, A photoresist bilayer of maP-1205 and LOR 7B is coated onto a sapphire substrate. **b**, The pattern is drawn out with a focused laser beam onto the light-sensitive top layer. The written region is shown as a faded area. **c**, After submersion in the developer solution, the written area of the top layer and part of the buffer layer are dissolved, leaving an undercut. **d**, Material is deposited onto the photoresist and exposed substrate surface. **e**, After submersion in the remover solution, the photoresist is dissolved completely, lifting the material that is not directly on the substrate. The undercut ensures a clean separation between the two layers. **f**, The device after the process, with deposited material in the written pattern.

4.1 Microstructuring the optoelectronic circuitry

In order to minimise higher-order waveguide excitations, the width of the signal line and gaps in the coplanar waveguide should be small — on the order of $10\ \mu\text{m}$. To achieve this, a microstructuring process based on photo-lithography was employed [133]. In this process (Fig. 4.1), a substrate is covered in a photo-sensitive mask, upon which a focused laser is used to expose the surface in the pattern of the desired structure. The exposed area is dissolved during a development process, revealing the bare substrate, onto which the material can be deposited via electron-beam evaporation. A final “lift-off” process dissolves the remaining mask layer, detaching the unwanted material from the substrate. These steps were carried out first for the photo-conductive switches, where silicon was deposited, followed by the waveguide, where gold was deposited atop an intermediary titanium binding layer.

The first step in the microstructuring process is the mask. This consists of a photo-sensitive layer, known as a photoresist, atop a buffer layer (Fig. 4.1a). Spin-coating is used to achieve a thin layer of each resist, which are subsequently cured at high temperature before lithography. For this work, the buffer layer was formed of LOR 7B, which was coated at 3500 rpm. The device was subsequently heated to $180\ ^\circ\text{C}$ for 4 min 5 s to cure the resist. The top layer was formed of maP-1205, which was coated at 2000 rpm and cured at $100\ ^\circ\text{C}$.

The microstructure is then written into the cured resist bilayer via exposure to laser light. The device is placed onto a stage, where it can be moved around in the laser focus. Switching the laser allows for selective exposure of the allocated pattern on the device, where exposure to light changes the chemical properties of the light-sensitive top layer. For maP-1205, which is a positive photoresist, the exposed area becomes soluble in a developer solution while the area that was not exposed remains insoluble (Fig. 4.1b). Negative photoresists also exist, which are soluble in the developer solution until exposure to light. The buffer layer is not light sensitive, and will slowly dissolve irrespective of its exposure to light. The development stage involved immersing the exposed devices in developer maD-331/S for 45 seconds, which results in the formation of an “undercut” as depicted in Fig. 4.1c. The purpose of the undercut becomes clear after material deposition, where it ensures a clean separation between the material on the substrate and that on the top of the photoresist. Without this separation, removal of the photoresist could result in damage to the device.

Materials for the optoelectronic circuitry were deposited using electron-beam evaporation. In this process, a tungsten filament is heated in a high-vacuum environment, resulting in electron emission. The emitted electrons are accelerated in an electric

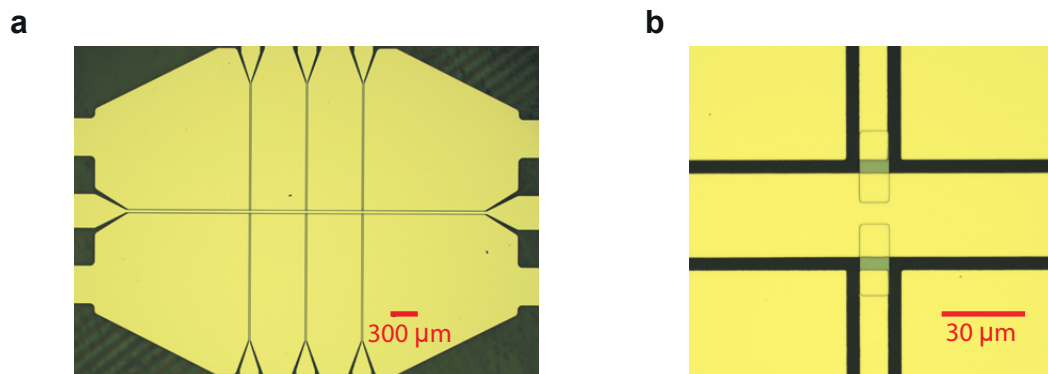


Figure 4.2: **Optical microscope image of a completed test device.** **a**, Full device. The signal line runs horizontally through the middle. The vertical branches are connected to the photoconductive switches. **b**, Zoomed in image of a pair of photoconductive switches.

field and focused into a beam using a magnetic field, after which they are directed onto a crucible containing the material which is to be deposited. The energy of the electron beam is transferred to the material, causing it to evaporate. The evaporated material is then deposited onto the substrate, which is suspended above the crucible in the vacuum chamber. A piezoelectric quartz crystal is also suspended in the chamber, onto which some material is also deposited. By measuring changes in the resonant frequency of a quartz crystal mounted within the chamber, the deposited mass and thickness of the material can be calibrated.

After material deposition, the device will resemble Fig. 4.1d. In order to reveal the patterned structure, the remaining resist must be removed in a lift-off process, which is done by immersing the devices into a solvent. In this case, devices were immersed in Remover PG at a temperature of 60 °C and left overnight. The lift-off process detaches the material that was not directly deposited onto the substrate, leaving the written pattern (Fig. 4.1e and 4.1f).

Fig. 4.2 shows an optical microscope image of a finished test device. The silicon switches can be seen connecting the detection line to the signal line, and the different deposition stages can be aligned to one another with sub-micron precision.

4.2 MBE growth of K_3C_{60} thin-films

Molecular-beam epitaxy is a deposition technique for growth of high-purity single crystal thin-films. A typical MBE configuration is displayed in Fig. 4.3. A material is deposited via thermal evaporation onto a substrate. By measuring changes in the

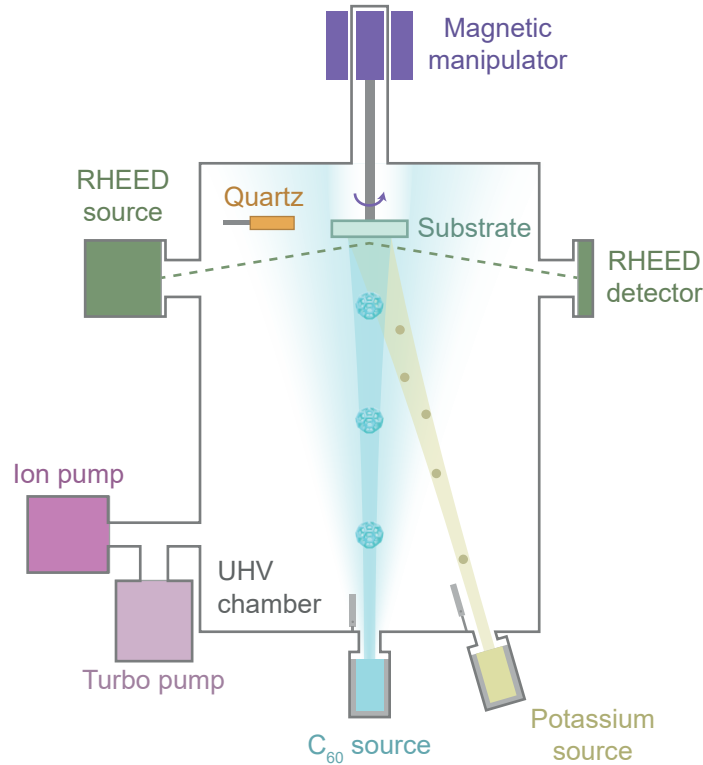


Figure 4.3: Schematic of an MBE chamber.

resonant frequency of a quartz crystal mounted within the chamber, the deposited mass and thickness of the material can be calibrated. The deposited material can be left with trapped impurities if particles are present in the vacuum, so deposition is carried out in an ultra-high vacuum environment (less than 10^{-10} mbar). The structure of the deposited material can be characterised in-situ using reflection high-energy electron diffraction (RHEED).

For the case of K_3C_{60} , film growth occurred in two steps: A thin film of C_{60} was first deposited onto the substrate, and was subsequently doped with potassium.

The structural quality of the deposited C_{60} depends upon the substrate surface quality and upon the conditions for crystal nucleation. Imperfections in the substrate surface, such as a large surface roughness, disturb the sample growth process and reduce the size of the grains that form. Fig. 4.4a displays an AFM image of a C_{60} film grown on a substrate of thermally-evaporated gold, with a substrate roughness of ~ 1 nm. The C_{60} forms small, poorly connected grains, as the rough surface prevents their undisturbed growth. Likewise, Fig. 4.4b shows a similar AFM image of a C_{60} grown on an annealed sapphire substrate. The sapphire forms atomically-flat terraces when annealed at high temperature (1200°C). The C_{60} formed under these

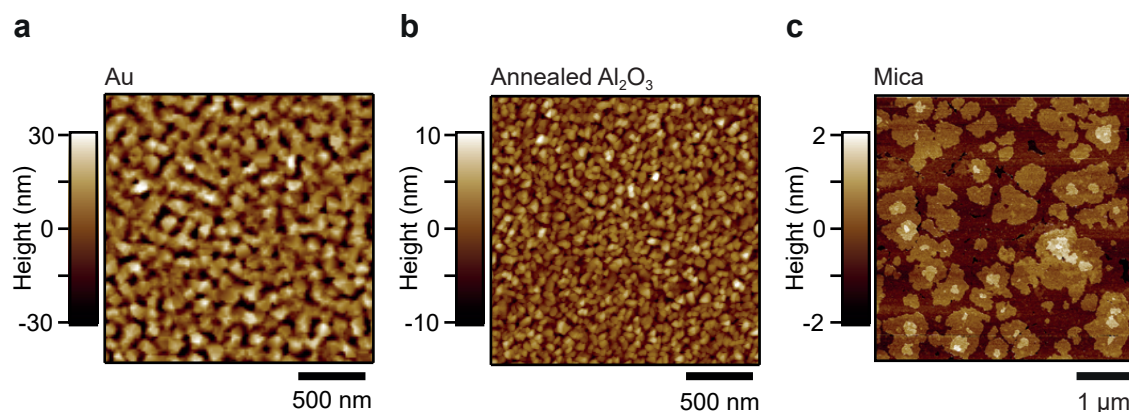


Figure 4.4: **MBE grown C_{60} thin films.** Atomic force micrographs of the C_{60} surface for optimised growth on **a**, gold, **b**, annealed sapphire, and **c**, mica substrates.

conditions has a significantly reduced roughness, and grains grow until they meet another grain with a different orientation.

To prevent the formation of grain boundaries, the domains must be aligned such that the edges merge when they meet. This is typically done by way of lattice matching to the substrate. The crystal structure of the substrate forms a potential landscape upon which the deposited C_{60} molecules orient themselves. When the potential landscape formed by the substrate matches the desired sample crystal structure in symmetry and lattice parameter, the nucleated domains will form in alignment with the crystal orientation of the substrate.

For C_{60} , this can be achieved through use of a Mica substrate. A cut along the (111) plane of C_{60} shows a hexagonal structure with a lattice parameter of 10.1 \AA . Mica can be cleaved to form an atomically flat surface, where the cleaved surface has a hexagonal crystal structure with a lattice parameter of 5.2 \AA [134]. Fig. 4.4c shows an AFM image of a C_{60} thin-film grown on a freshly-cleaved mica substrate. A layered structure can be seen in the image, where terraces in the film form with a thickness of 14 \AA , corresponding to a single layer of C_{60} . At the optimal temperature, C_{60} molecules will move to fill in gaps at the lower-lying layers before more layers form, minimising the inhomogeneity.

Nucleation on the substrate is affected by the deposition rate and substrate temperature. Deposition rate is dependent on chamber-specific factors such as the distance between the crucible and the substrate, but can be primarily controlled by the crucible temperature. A deposition rate of approximately 4 \AA min^{-1} was found to be optimal for C_{60} deposition, corresponding to a crucible temperature of $380 \text{ }^\circ\text{C}$. The substrate is also mounted on a filament, allowing for temperature control of the substrate itself. Reliable epitaxial growth of a material is achieved at a “sweet spot”

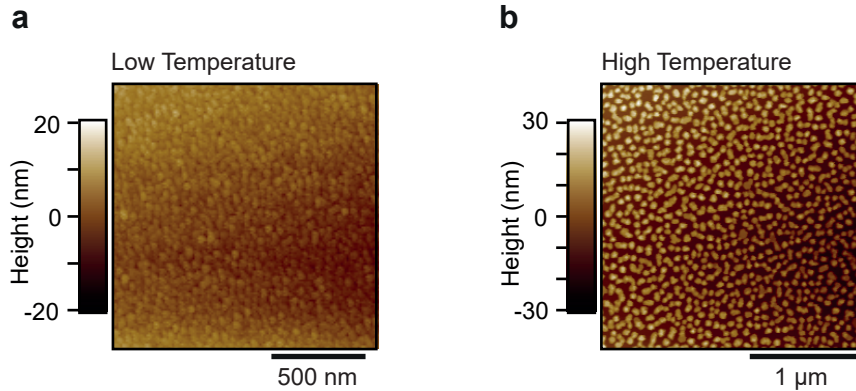


Figure 4.5: **Substrate-temperature dependence of C_{60} growth on a mica substrate.** Atomic force micrographs of the sample surface for growth at **a**, low substrate temperature (approx. 150°C) and **b**, high substrate temperature (approx. 170°C). Optimal substrate temperature is approximately 160°C .

for substrate temperature. If the substrate is too cold, the deposited molecules move only a short distance by way of Brownian motion, and the resulting growth is amorphous. If the substrate is too hot, nucleation is too aggressive, which results in the formation of islands of material that grow too quickly in the direction normal to the substrate. Fig. 4.5 displays C_{60} growth on a mica substrate at sub- and super-optimal temperatures. In the low-temperature sample, only very small crystals were able to form. On the other hand, the high temperature sample shows islands of crystalline grains that are disconnected. The substrate surface can be seen between the grains, and the roughness indicates that the grains developed normal to the substrate. At the ideal temperature, domains will grow outwards from their nucleation point, in the plane of the substrate surface, resulting in the growth seen in Fig. 4.4c.

With an optimal deposition rate and substrate temperature, granular growth on an atomically-flat, non-lattice-matched substrate can nevertheless produce a sample with desirable properties. As such, annealed sapphire and mica are both viable candidates for use in experiments on MBE-grown K_3C_{60} that can be chosen based on other experimental considerations. In this work, annealed sapphire was used for its minimised interaction with the mid-infrared excitation pulse and for high deposition quality.

The deposited C_{60} thin-film is then doped with potassium to form K_3C_{60} . Potassium is thermally evaporated onto the C_{60} , where it is absorbed. To achieve the correct stoichiometry for the doped film, the resistance is monitored in-situ. Of the K_xC_{60} compounds, a resistance minimum is observed at $x = 3$ [135]. Measurements on K_3C_{60} samples in single-crystal, thin-film, and pressed powder form have displayed

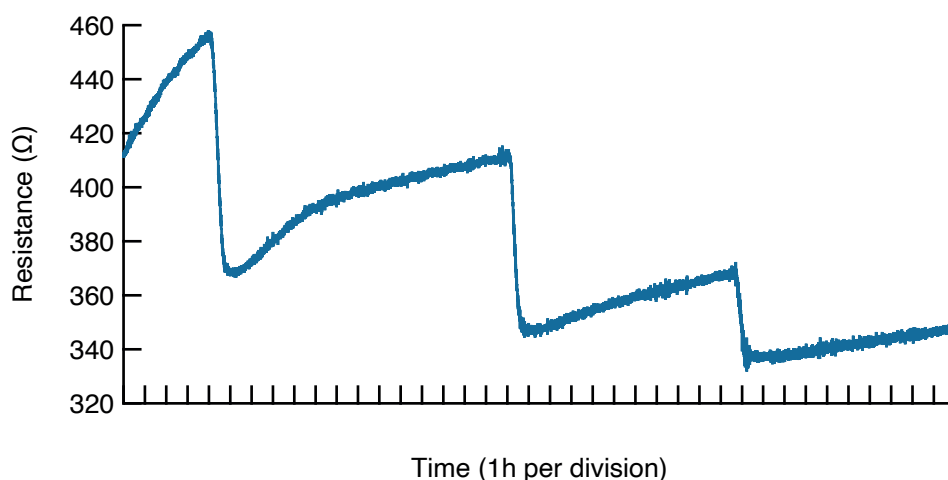


Figure 4.6: K_xC_{60} resistance versus time during the doping process. The resistivity decreases while the potassium shutter is opened, seen as the downward steps. After the shutter is closed, the resistivity increases over time as the potassium diffuses into the film.

resistivities in the range of $1\text{--}5\text{ m}\Omega\text{ cm}$, providing a quantitative observable as a metric for doping uniformity during the doping process [71, 136–139].

The diffusion time of the potassium in the C_{60} must also be taken into consideration. After blocking the potassium source, a sample of 100 nm thickness requires several hours for the potassium to homogenise. This indicates that a fast doping rate will result in an inhomogeneous stoichiometry along the thickness of the film. K_4C_{60} exhibits a structural change from an fcc lattice to bct [69], so a significant overdoping of the sample surface cannot be reversed via potassium diffusion. To prevent overdoping and maximise stoichiometric homogeneity, a dope-anneal cycle was used, consisting of one hour of doping with the potassium source at 100°C followed by a $3\text{--}8\text{ h}$ anneal where the substrate temperature was increased to 300°C to facilitate faster potassium diffusion. An example resistivity profile of the K_xC_{60} thin film is shown in Fig. 4.6. Following this procedure, doped thin films could be obtained with resistivities of $1\text{ m}\Omega\text{ cm}$ for samples on mica substrates and $3\text{ m}\Omega\text{ cm}$ for samples on annealed sapphire substrates. In both cases, the samples exhibited metallic behaviour from the annealing temperature of 575 K down to the critical temperature of 19 K .



Figure 4.7: Schematic of sapphire shadow mask for C_{60} growth.

4.3 Integrating K_3C_{60} into ultrafast circuitry

Now that we have a means to both manufacture ultrafast electronic circuits and grow K_3C_{60} thin films, the next step is to combine them. This comes with two important challenges: first, the C_{60} thin film itself must be microstructured and doped in the ultrafast circuitry, and second, the doped K_3C_{60} is highly reactive and must be hermetically sealed in an inert atmosphere before a transfer to the cryostat can occur.

For the transport experiments discussed here, the choice of substrate has implications for the dielectric properties of the resulting device. This factor must also be reconciled with optimising K_3C_{60} growth. The choice of a coplanar waveguide structure is helpful in this regard, in that the substrate has a smaller impact on its dielectric properties when compared to another geometry, such as a microstrip. Ultimately, however, the device production process degrades the mica surface quality to such an extent that epitaxial C_{60} growth is no longer possible, leaving annealed sapphire as the most desirable option.

4.3.1 Microstructuring K_3C_{60}

Thin films of K_3C_{60} were incorporated directly into the signal line of the coplanar waveguide. This was to ensure that measurements could be done in both DC and at high frequencies. To do this, the waveguide was manufactured with a gap in the signal line, into which the C_{60} thin film was grown. The C_{60} is soluble in the chemicals used in the photolithography process, so a different approach is required to create a mask. A mask of $150\ \mu\text{m}$ thick sapphire was used for the C_{60} deposition, into which a $20\ \mu\text{m} \times 30\ \mu\text{m}$ rectangular hole was laser-cut. A profile of the laser-cut mask is shown in Fig. 4.7. The ablation process results in a smaller hole in the bottom surface of the mask. Empirically, sample growth is better when this surface is placed on the device. This is likely because it limits the possibility of

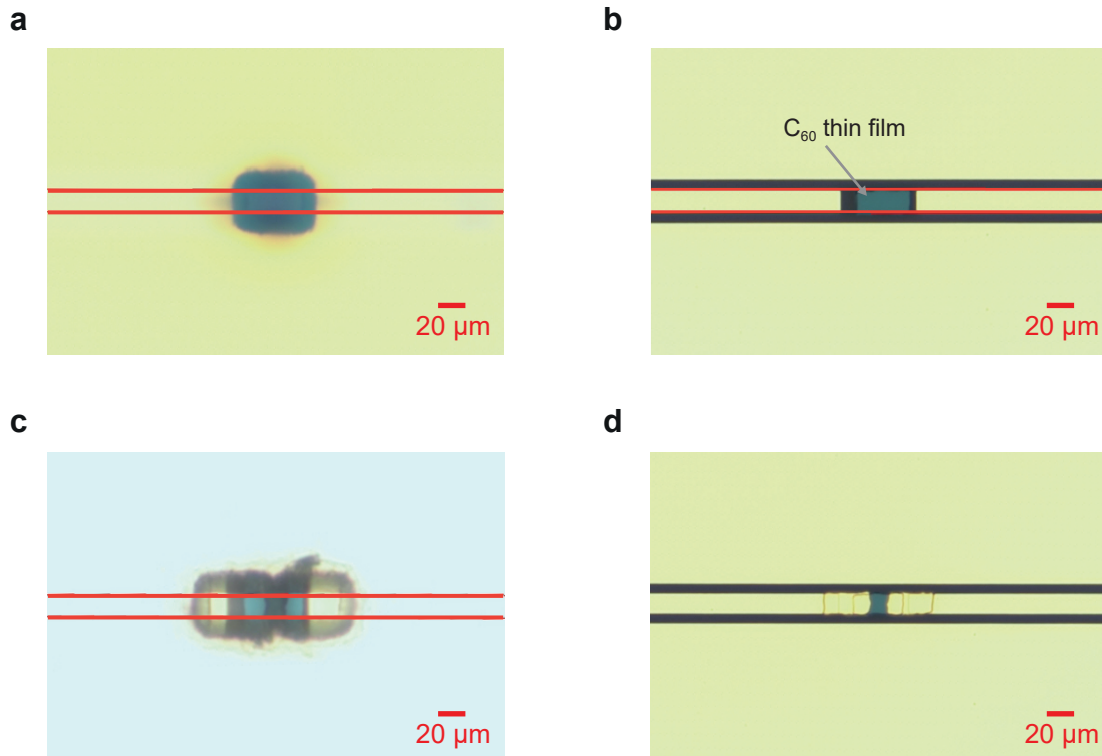


Figure 4.8: **Growth and contacting of C_{60} using a shadow mask.** **a**, Mask alignment for C_{60} deposition. **b**, Resulting C_{60} thin film in the CPW. **c**, Mask alignment for gold contact deposition. **d**, Final contacted device. The red lines demarcate the edges of the signal line of the CPW.

C_{60} molecules scattering from the sloped surface back towards the substrate. The mask was aligned to the device under an optical microscope. For this process, the device was placed onto a heating stage, while the mask was mounted onto a 3-axis micrometer translation stage. After alignment, the mask was connected to the sample holder with three small dots of H20E silver epoxy. The stage was then heated to 120°C for 20 minutes to cure the epoxy and fix the mask in place. An optical microscope image of the device with mask in place is displayed in Fig. 4.8a, and the resulting C_{60} thin film can be seen in Fig. 4.8b.

After growth of C_{60} has taken place and the first mask removed, the sample must be contacted in order to monitor the resistance while doping with potassium. A practical advantage of the coplanar waveguide structure is that DC measurements can be carried out directly in this geometry. However, we have established that C_{60} does not grow well on the deposited gold, so depositing C_{60} directly onto the edges of the gold signal line would result in poor contacts. To overcome this, titanium/gold contacts were deposited onto the C_{60} and signal line. This was carried

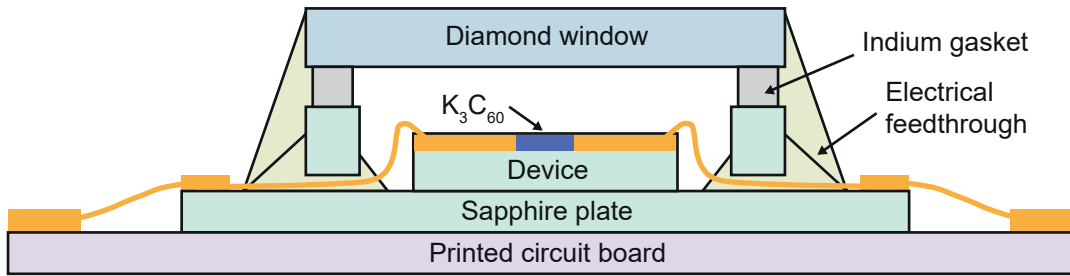


Figure 4.9: **Hermetic sealing construction.** The construction is completed in an argon-purged glove box with the indium gasket and diamond window after doping of the sample.

out using a similar sapphire shadow mask to that used for C_{60} growth, except with two $20\ \mu\text{m} \times 40\ \mu\text{m}$ rectangular holes spaced $20\ \mu\text{m}$ apart (Fig. 4.8c). After attaching the mask, 10 nm of titanium was deposited followed by 360 nm of gold. The evaporated contacts are shown in Fig. 4.8d, with a $20\ \mu\text{m} \times 20\ \mu\text{m}$ exposed area of C_{60} .

To access the device with external electronics, the ends of the signal line and detection lines were contacted with gold wires, bonded using conductive silver epoxy.

4.3.2 Hermetic sealing

To protect the reactive K_3C_{60} thin film from the atmosphere, certain preparations were necessary before the doping could take place. In addition to protecting the sample from the atmosphere, the sealing structure must also preserve optical and electrical access to the device. This was achieved using the structure illustrated in Fig. 4.9. Electrical feedthroughs were fabricated from a sapphire ring and Torr seal vacuum epoxy, with the insulating vacuum epoxy serving as a feedthrough medium for the bonded wires, and holding the sapphire ring in place. The feedthrough wires were then used to connect the signal line and C_{60} to an external source meter in order to monitor the resistance while doping.

After doping, the sample was transported in a high-vacuum suitcase into an argon-purged glove box, where the remaining sealing could take place. Here, the device was capped with a diamond window to facilitate optical access. The diamond window facilitates optical access and has a featureless optical response in the mid-infrared range with a transmissivity of 70% for the pump wavelength of $7\ \mu\text{m}$ [140]. The degas from the vacuum epoxy curing process is damaging to K_3C_{60} , necessitating

a intermediary indium seal between the sapphire ring and diamond window. The epoxy itself then provided a more stable seal for removal from the glove box.

The device was then contacted to a printed circuit board and connected to the optical cryostat for measurements.

4.4 Device characterisation

The equilibrium DC properties of the K_3C_{60} thin film were measured directly on the experimental device, serving as a vital preliminary characterisation tool.

Resistance vs temperature

DC measurements were carried out on the K_3C_{60} thin film in a two-contact geometry. The resistance vs temperature of the K_3C_{60} thin film is displayed in Fig. 4.10a, including contributions from contact resistance and cryostat wiring, carried out with a DC current bias of $1\mu\text{A}$. Since the resistance of the K_3C_{60} was much larger than these additional contributions, it dominated the observed response. The film demonstrated metallic behaviour above T_c , and a superconducting transition that began at $\sim 19\text{K}$, indicating good sample quality.

An expanded view of the superconducting transition is shown in the inset of Fig. 4.10a. Here, the transition was found to be broadened with a width of 5K . This is expected for the granular samples grown on sapphire substrates, as a broadened transition is a typical feature of a granular superconductor [141]. Stoichiometric inhomogeneity is characterised by a double superconducting transition [142–144], but no such feature was observed in the doped K_3C_{60} , indicating that the doping was uniform.

Critical current in the superconducting state

The resistance of the K_3C_{60} thin film is plotted in Fig. 4.10b as a function of the applied current, for a temperature of 8K . At this temperature, the sample showed zero resistance for the applied biases smaller than the critical current. The onset of resistance in the K_3C_{60} thin film occurred when the applied current bias exceeded 1.5mA . Larger currents resulted in an increased resistance in the thin film, which eventually approached the resistance value seen in the metallic state above T_c .

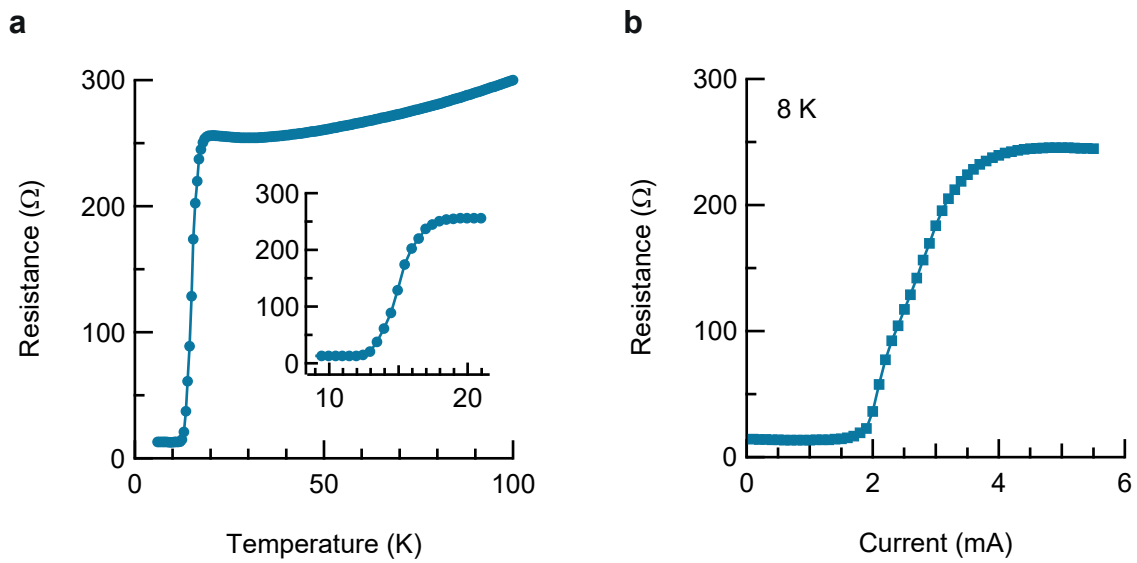


Figure 4.10: **DC characterisation of the K_3C_{60} thin film.** **a**, Resistance versus temperature, carried out with a $1\ \mu\text{A}$ bias. The inset shows a zoomed-in region around the superconducting transition. **b**, Resistance versus current at 8 K. The onset of resistance occurs at the critical current of $\sim 2\ \text{mA}$. Measurements were carried out on the experimental device in a two-contact configuration.

Chapter 5

Nonlinear current-voltage behaviour in optically-driven K_3C_{60}

Parts of this chapter have been published in [145].

This chapter will describe experiments using sub-picosecond current pulses to probe the current-voltage characteristics of the photo-excited phase in K_3C_{60} . In doing so, we seek to understand whether the current-voltage characteristics exhibit nonlinear behaviour that would be expected from critical current effects in a superconductor. In order to search for a critical current in the photo-excited phase above T_c , we must understand how the critical current behaves on ultrafast timescales in a thin-film superconductor below T_c . This is discussed first from literature, followed by current pulse experiments on the equilibrium state of K_3C_{60} below T_c . Finally, we discuss the measurements of the photo-excited phase above T_c .

5.1 The critical current in superconductors

The critical current is a macroscopic observable in a superconductor, defined as the largest electrical current that a superconductor can transport before the onset of resistivity. This is demonstrated in Fig. 5.1, where the thin film of K_3C_{60} was biased with a current source and the voltage was measured in a two-contact geometry. In Fig. 5.1a, the voltage across the thin film vanished at low temperatures and low currents, as expected for a dissipationless superconducting state. However, upon increasing the current above a critical value ~ 2 mA, a voltage drop set in, eventually trending towards Ohmic behaviour. The onset of dissipation is well-illustrated by examining the resistance versus applied current, as shown in Fig. 5.1b.

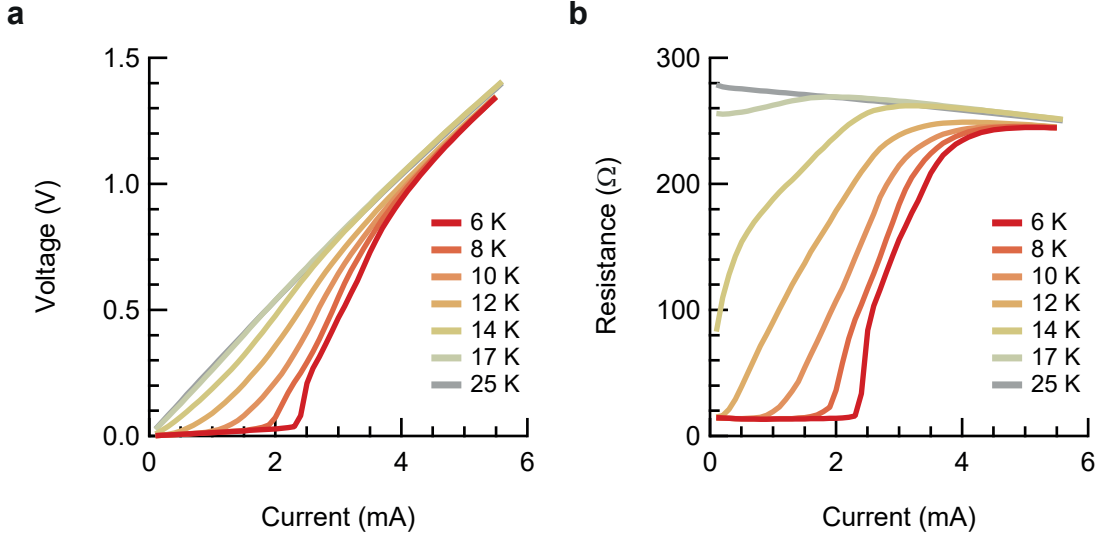


Figure 5.1: **Critical current of a K_3C_{60} thin film.** **a**, Voltage versus current, and **b**, Resistance versus current for temperatures in the range 6–25 K. All measurements were taken in a two-contact configuration under a DC bias current.

5.1.1 Origin in type I and type II superconductors

In 1916, F. B. Silsbee proposed that the critical current arises from the magnetic self-field due to the supercurrent [146]. Once the magnetic self-field due to the supercurrent (Fig. 5.2a) exceeds H_c , superconductivity is no longer energetically favourable. In a thick wire of radius r_0 , this can be written as

$$I_c = \frac{H_c r_0}{2}. \quad (5.1)$$

This relation holds up well for DC measurements in the type I elemental superconductors, and coincides well with the depairing current density J_d , which is the current density above which the kinetic energy of the Cooper pairs exceeds their binding energy [147]. This can also be related to the London penetration depth λ and written as [148]

$$J_d \sim \frac{H_c}{\lambda}. \quad (5.2)$$

However, additional considerations become important in other systems and on shorter timescales. For example, in a type II superconductor, a magnetic self-field exceeding the lower critical field H_{c1} will result in the nucleation of vortex/anti-vortex pairs, as shown in Fig. 5.2b. In the absence of pinning, which will be discussed later, the vortices move towards the centre of the material due to the Lorentz force $F_L = J \times B$, whereby work is done and energy is taken from the supercurrent. This energy is dissipated as heat when the vortex pairs meet and annihilate. The tem-

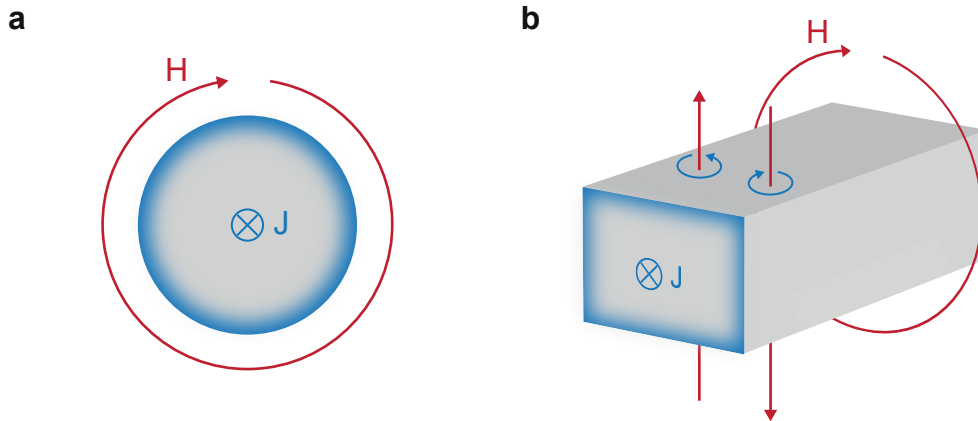


Figure 5.2: **Critical current and magnetic fields.** **a**, Magnetic self-field H due to a current density J . **b**, Vortex/anti-vortex pairs form in a type II superconductor once the self field exceeds H_{c1} .

perature therefore increases, resulting in further vortex formation and a runaway effect where the supercurrent is destroyed.

5.1.2 Extension to granular thin films

In the absence of any factors inhibiting vortex motion, one would expect the onset of resistivity to coincide with the formation of vortices, i.e. when $H = H_{c1}$. Vortex motion can, however, be affected in several ways. First, vortices can localise on inhomogeneities within the superconductor, known as “vortex pinning” [43, 149]. When microstructural inhomogeneities exist within the material, superconductivity can be locally suppressed. This gives rise to local energy minima experienced by the vortices. The potential well therefore acts against any forces that are applied to the vortex, meaning that a larger current is required to induce vortex motion, leading to an increase in the critical current.

On the other hand, the magnetic flux vortices are of opposite polarity at opposing surfaces, so they attract one another when the separation between them is small. For a vortex separation larger than the London penetration depth, the magnetic field from one vortex is screened from the other by the superconducting bulk. However, when the vortex separation is on the order of λ or smaller, the attractive force between antipolar vortices becomes significant.

The interplay between these effects can be illustrated nicely in superconducting thin films. Consider the case of a type II superconducting thin film of thickness a . When $a > \lambda$, the critical current is governed by the pinning of flux vortices [150]. In this

case, pinning suppresses vortex motion and the critical current corresponds to a self-field that is *larger* than H_{c1} . However, in the case that $a \sim \lambda$, vortex attraction generally overcomes the pinning force as soon as the magnetic flux vortices form. This leads us to write

$$J_c \sim \frac{H_{c1}}{\lambda} \quad (5.3)$$

for a film with thickness comparable to the London penetration depth. This relation has been shown to hold for many type II superconducting compounds as long as $a \sim \lambda$ [149]. This current is known as the depinning current, and is observed when heat dissipation due to vortices is the dominant effect influencing the critical current.

The depinning current generally overshadows the depairing current in a type II superconductor, since the latter is related to the thermodynamic critical field H_c , which is larger than H_{c1} . The depairing current is therefore typically very large in a type II superconductor, with values in the range of $10^{12} - 10^{13} \text{ A m}^{-2}$ [147]. However, the depairing current becomes relevant when heating due to vortex dissipation can be eliminated, and has been observed in various systems by suppressing vortex motion through the introduction of artificial pinning centres [151, 152], by suppressing vortex formation with nanobridge structures [153, 154], and by using pulsed currents on timescales much shorter than those of heat dissipation [150].

It is important to note that the critical current is heavily dependent on the macroscopic structure of the sample, with the shape affecting the self-field distribution around the sample [43], and granularity leading to phase slips across domain boundaries [155].

5.1.3 Effect of short current pulses

By applying the current on a short timescale, a significant reduction in the total heating of the system is expected. The reduced heating enables supercurrents to propagate with magnitudes greater than the DC critical current but smaller than the depairing current for a short amount of time. This results in a broadening of the resistance vs current curves when comparing pulsed-current measurements to DC measurements. This is illustrated in the experimental data shown in Fig. 5.3. Here, voltage pulses of nanosecond duration were applied to the K_3C_{60} thin film, and the resistance was measured at the end of the pulse (Fig. 5.3a). The resistance vs current is displayed in Fig. 5.3b for various pulse durations, and compared with a DC measurement. In the DC case, the resistivity sets in sharply once the critical

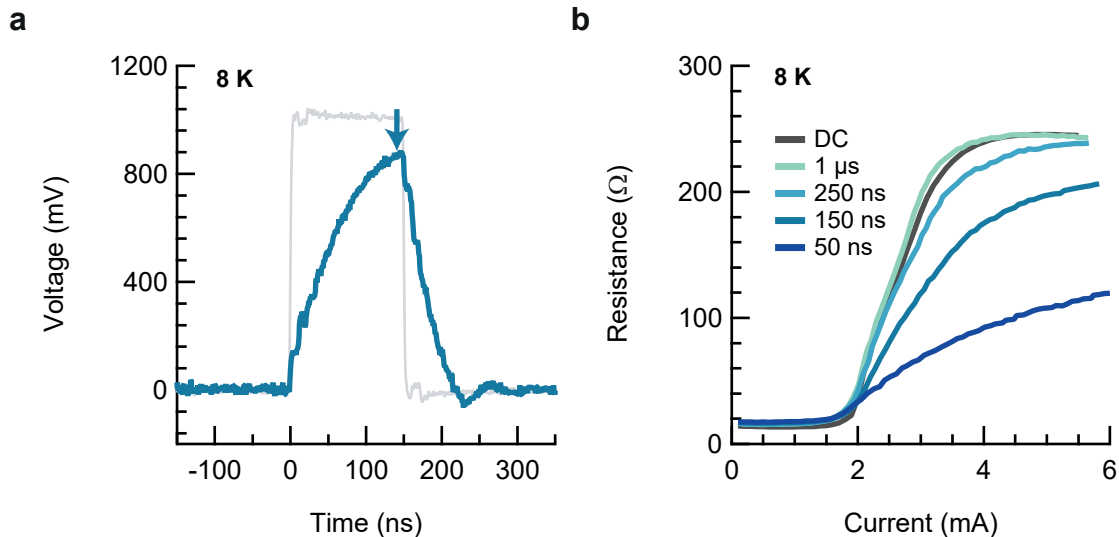


Figure 5.3: **Nanosecond critical current measurements.** **a**, Voltage drop measured across the K_3C_{60} film versus time (blue) in a two-contact geometry at 8 K, with a 150 ps flat-top voltage pulse of 5 V amplitude. Measurements were taken with a 1 k Ω preresistor. The incoming voltage pulse is divided by 5 and shown in grey. The arrow indicates at which time the voltage is read to calculate the resistance. **b**, Resistance versus current across the device, for pulse durations of 50 ns, 150 ns, 250 ns, and 1 μ s, and in DC.

(depinning) current is reached, but for shorter pulse durations the transition is significantly broader.

This broadening becomes more apparent when we move to even shorter pulse durations, such as the picosecond pulses we will be using to examine the photo-excited state in K_3C_{60} . In section 5.3, we will look at the effect of picosecond currents on the equilibrium superconducting state.

5.2 Probing with ultrafast currents

Fig. 5.4 depicts the experimental schematic for a picosecond transport measurement on the K_3C_{60} thin film. The two leftmost switches were biased simultaneously with a DC voltage, and excited with a femtosecond laser pulse at 515 nm wavelength with a repetition rate of 50 kHz. The excitation symmetrically launched current pulses with picosecond duration into the waveguide (see Chapter 3). The incoming pulses were first detected at Switch 1, providing a reference. After interaction with the sample, the partially reflected pulses were also detected at Switch 1. The partially transmitted pulses were then detected at Switch 2. By scanning the time delay between the launching laser pulse and detection laser pulse, a time resolved picture

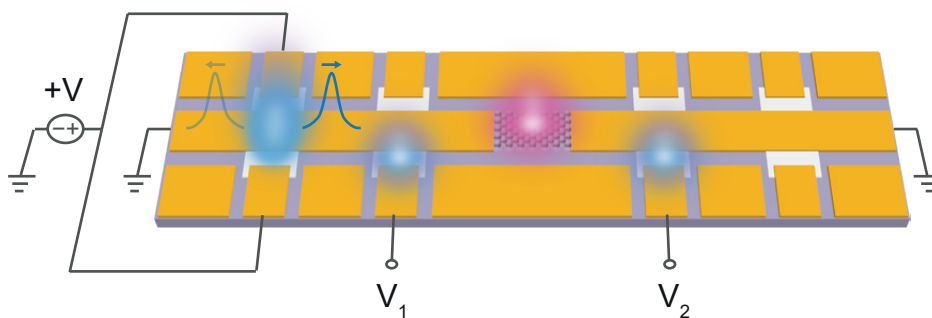


Figure 5.4: **Picosecond current pulse setup.** Current pulses were launched by biasing and exciting the leftmost pair of switches. The incident and reflected pulses were detected at V_1 . The transmitted pulses were detected at V_2 .

of the voltages at Switch 1 (V_1) and Switch 2 (V_2) could be obtained. Details for the calibration of V_2 are explained in Appendix A.

The ends of the conduction line were connected to ground, meaning that residual charge introduced with the injection of current pulses was able to dissipate on timescales faster than the $20 \mu\text{s}$ repetition period of the laser.

The first set of measurements that we will discuss were conducted with the K_3C_{60} sample in equilibrium. In the second set of measurements, application of mid-infrared laser excitation allowed for the same current pulse measurements to be carried out in the non-equilibrium regime. The pre- and post-excitation sample properties could be determined by adjusting the time delay between the mid-infrared laser pulse and the current pulse.

5.3 Ultrafast transport properties of equilibrium K_3C_{60}

5.3.1 Transmission and reflection in the metallic and superconducting states

The voltages V_1 and V_2 are plotted in Fig. 5.5a for the temperatures 8 K and 20 K. The first peak in V_1 is the incoming current pulse, which serves as a reference for the pulse magnitude, and all voltages were normalised by the peak of this pulse. The second pulse in V_1 is the reflected pulse from the sample. On cooling through the superconducting transition, the reflected pulse decreased in amplitude and developed

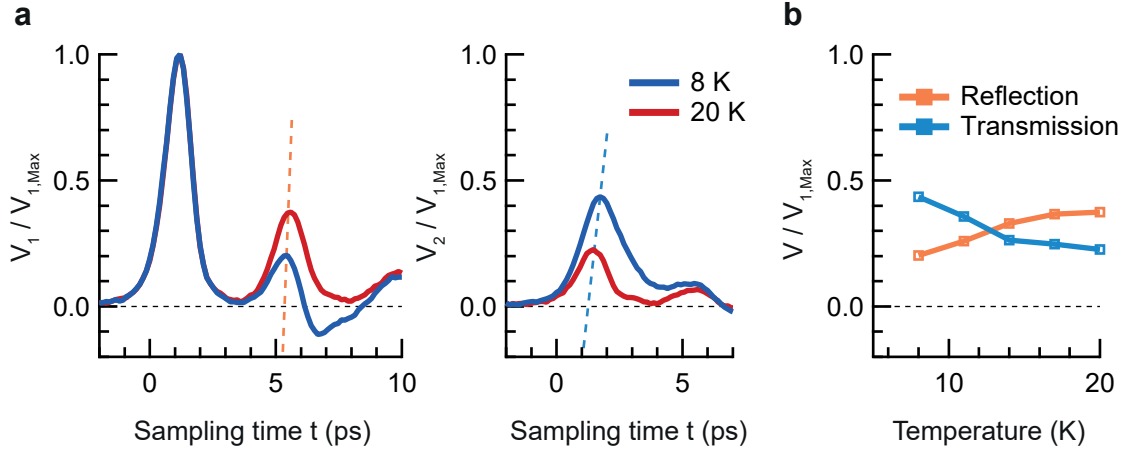


Figure 5.5: **Equilibrium picosecond current pulse measurement on the K_3C_{60} thin film.** **a**, Left: V_1 versus probe-gate delay; the incident and reflected pulses. Right: V_2 versus probe-gate delay; the transmitted pulse. **b**, Peaks of the reflected and transmitted pulses versus temperature. All data are normalised by the peak of the incident pulse in V_1 .

an additional negative response at a time delay of 5 ps, indicating a significant reduction in the low-frequency component of the reflection. Similarly, while at 20 K the transmitted pulse in V_2 was strongly attenuated, the amplitude increased significantly when cooling to 8 K and the pulse was broadened in time. The peaks of both the reflected and transmitted peaks are tracked in Fig. 5.5b as a function of temperature, illustrating a shift in spectral weight from the reflected pulse to the transmitted pulse upon cooling through T_c .

The differences in the above- and below- T_c reflection and transmission properties can be qualitatively well-understood in terms of the conductivity of the superconducting state. When cooling well below T_c , the spectral weight in σ_1 condenses into a delta peak at zero frequency. As such, the DC component of the incident current pulse is entirely transmitted, and the reflected pulse has no DC component. Similarly, the increase in spectral weight in σ_2 results in an inductive response in the sample, and a phase shift arises in both the reflected and transmitted pulses. It should be noted that the true reflection and transmission coefficients of the sample are expected to be slightly larger than the ratios observed in the raw data, since the incident pulse is also partially reflected from the detection switches before interacting with the sample.

The increase in DC transmission is seen clearly in the frequency domain, as shown in Fig. 5.6a, where the transmittance increases most significantly at lower frequencies. Below frequencies of 400 GHz, the modulus of the transmittance was larger than 1

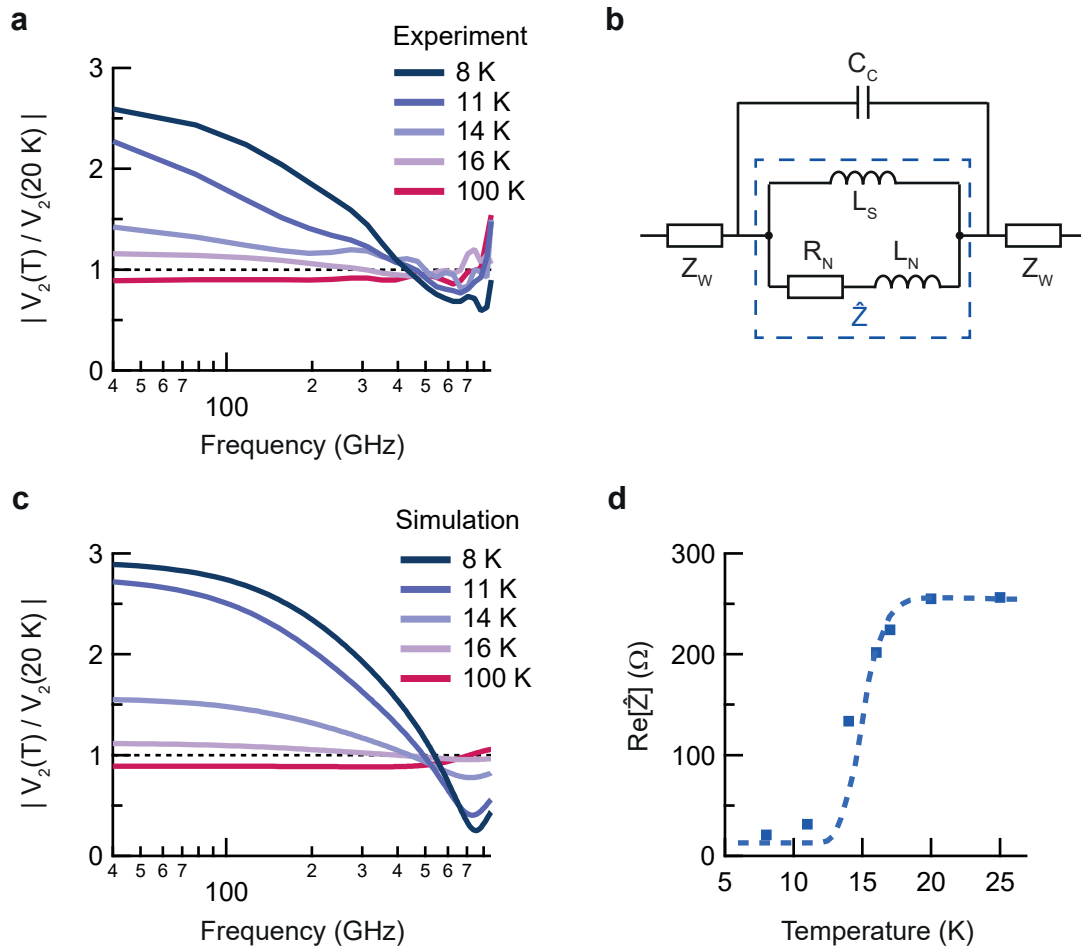


Figure 5.6: **Transmittance data in the frequency domain.** **a**, Normalised transmittance measured for temperatures below T_c in the range 8–16 K, and above T_c at 100 K, normalised by the transmittance at 20 K. **b**, Circuit model used to simulated the transmittance. The dashed lines highlight the two-fluid model representing the K_3C_{60} sample. **c**, Simulated transmittance using the circuit model in **b**. **d**, Real component of the impedance at 50 GHz (blue squares) alongside the DC resistance (blue dashed line) as a function of temperature.

for temperatures $T < T_c$, and smaller than 1 for temperatures $T > T_c$. At higher frequencies, a dip was observed for temperatures below T_c , centred at 700 GHz, due to an LC resonance formed by the inductance of the superconducting K_3C_{60} and the capacitance C_C between the two contacts on either side of the sample.

The transmittance of the sample was simulated using the circuit model depicted in Fig. 5.6b, where the K_3C_{60} transport properties were considered in a two-fluid picture, consisting of an superconducting channel with kinetic inductance L_S and a metallic channel with resistance R_N and kinetic inductance L_N . The two-fluid model can be collected into a total complex sample impedance \hat{Z} . The transmission line impedance was included as an impedance Z_W on either side of the sample. The simulated transmittance is displayed in Fig. 5.6c.

The sample transmittance $\bar{\Theta}(\omega, T)$ is given by

$$\bar{\Theta}(\omega, T) = \frac{V_2(\omega, T)}{V_2(\omega, 20 \text{ K})} = \frac{2Z_W + \hat{Z}(\omega, 20 \text{ K})}{2Z_W + \hat{Z}(\omega, T)}, \quad (5.4)$$

from which the complex impedance $\hat{Z}(\omega, T)$ of the sample was extracted. The real component of $\hat{Z}(\omega, T)$ for $\omega = 50$ GHz, plotted in Fig. 5.6d as a function of temperature, was found to scale consistently with the DC resistance.

5.3.2 Nonlinear current dependence below T_c

The next step was to investigate the effect of supercritical picosecond currents on the K_3C_{60} thin film. A current-driven suppression of the superconducting state is expected to manifest as a nonlinearity in the current-dependence of the transmittance. The voltage V applied to the launching switches was varied in order to control the magnitude of the injected current pulses. The transmittance versus the peak current is displayed in Fig. 5.7 for temperatures of 8 K and 25 K. The time-domain (Fig. 5.7a) and frequency-domain (Fig. 5.7b) responses at 8 K displayed a reduction in magnitude with increasing current, consistent with a suppression of superconductivity. In the frequency domain, the nonlinear current-voltage response was observed to be strongest at lower frequencies. On the other hand, at the above- T_c temperature of 25 K, the transmittance was found to be entirely linear in current (Fig. 5.7c and Fig. 5.7d).

The real part of the impedance $\hat{Z}(\omega, T)$ at $\omega = 50$ GHz was extracted as before, and its picosecond current dependence is compared against the DC measurements in Fig. 5.8. The picosecond impedance measurement followed the trend observed with nanosecond pulses, with an onset of resistivity notably occurring above a critical

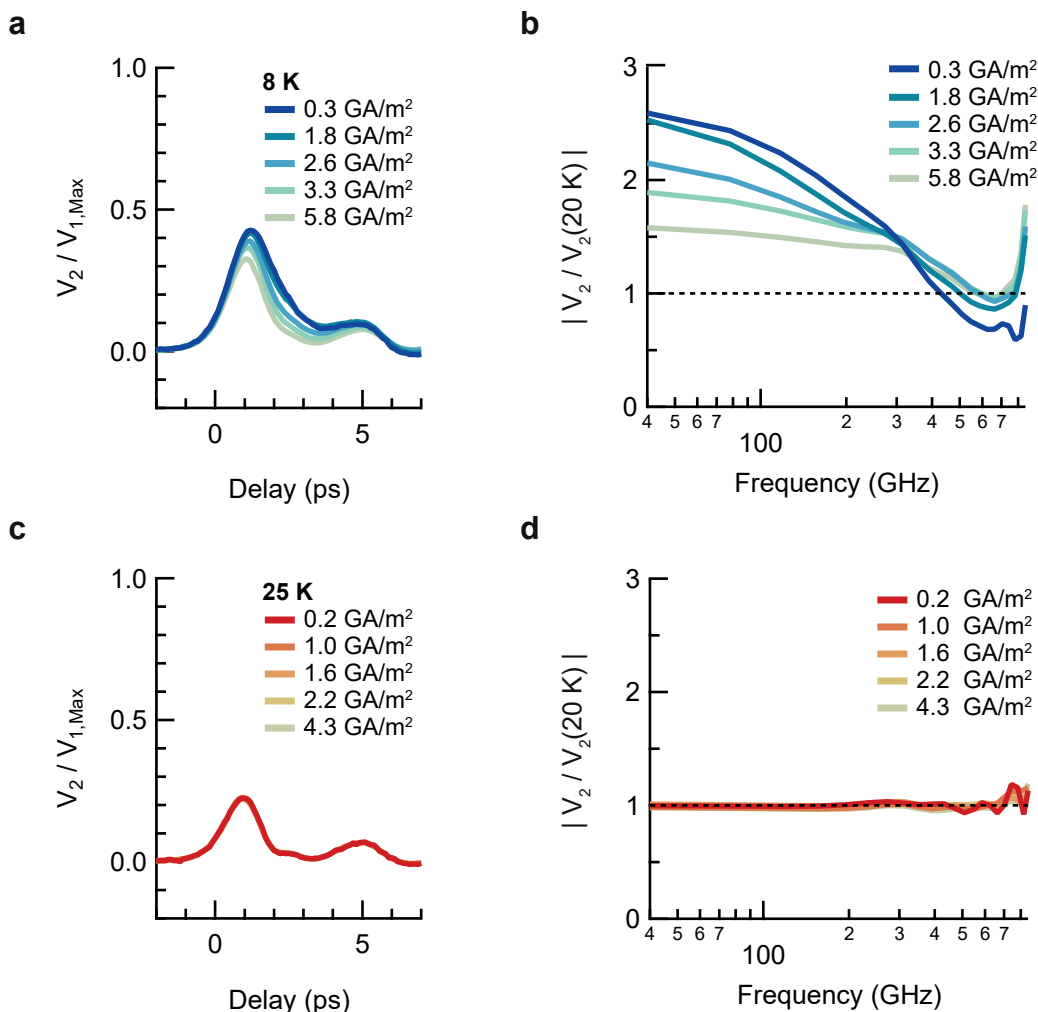


Figure 5.7: **Current dependence of the transmitted pulse.** **a**, Transmitted pulse V_2 vs probe-gate delay at 8 K, for peak currents in the range $0.3\text{--}5.8\text{ GA m}^{-2}$. **b**, Fourier transform of the data in (a). **c**, Transmitted pulse V_2 vs probe-gate delay at 25 K, for peak currents in the range $0.3\text{--}5.8\text{ GA m}^{-2}$. All curves lie atop one another. **d**, Fourier transform of the data in (c).

value, but at a much slower rate for this ultrashort pulse duration. For intermediate temperatures just below T_c , finite resistivity was observed even at the lowest currents, with the resistivity increasing further with increasing current. Nonlinear current-voltage behaviour was only observed at temperatures below T_c .

The superconducting transition from the metallic state at $T > T_c$ to a purely inductive superconductor (Fig. 5.6) was broadened due to the polycrystalline structure of the thin film, with the purely inductive behaviour only observed for $T < 0.6T_c$. This can be understood by considering a granular superconductor [155–159] consisting of an array of superconducting grains connected by weak links. At finite temperatures below T_c , thermally activated phase-slips across the weak links result in the onset of resistivity, and thus the broadening of the transition.

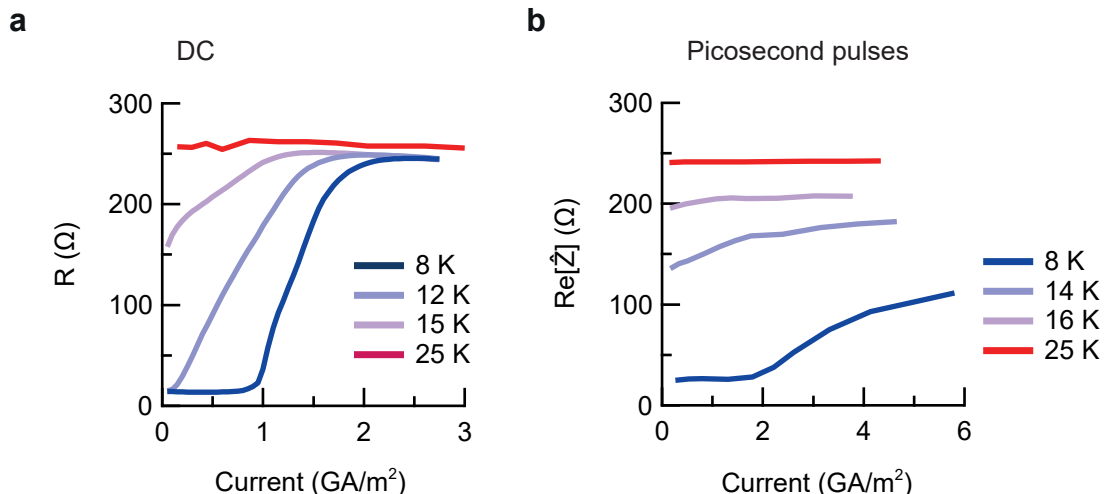


Figure 5.8: **Current dependence of the impedance.** **a**, Resistance vs current in DC for temperatures 8 K, 12 K, 15 K, and 25 K. **b**, Real component of the impedance at 50 GHz vs peak current, measured with picosecond current pulses at temperatures 8 K, 14 K, 16 K, and 25 K.

At the lowest measurement temperature of 8 K, thermal phase fluctuations are reduced and transport is dominated by coherent tunnelling between grains. Once the current density exceeds the critical current density J_c , phase-slips are induced at the weak links, leading to a finite resistance that grows with bias current. The behaviour under picosecond pulses can be understood by considering that the phase-slips are generated less efficiently with such a short pulse duration, so the resistance increases less sharply with current.

At intermediate temperatures, phase-slips are already induced by thermal fluctuations at the lowest applied currents, so the resistivity is finite. As the current is increased, current-induced phase-slips result in a further increase in resistance. As such, nonlinear current-voltage behaviour is still observed in the finite-resistivity regime just below T_c .

5.4 Photo-excitation of K_3C_{60} below T_c

The optical excitation is now introduced, and we begin by investigating the transmittance of the K_3C_{60} thin film when photo-excited below its superconducting critical temperature. The K_3C_{60} thin film was photo-excited with a 300 fs excitation pulse at $7 \mu m$ wavelength, and subsequently probed on-chip with a picosecond current pulse after a delay of 15 ps. Mid-infrared pulses with a fluence of $4 mJ cm^{-2}$ were used. The transmitted current pulses were measured as described for the measurements

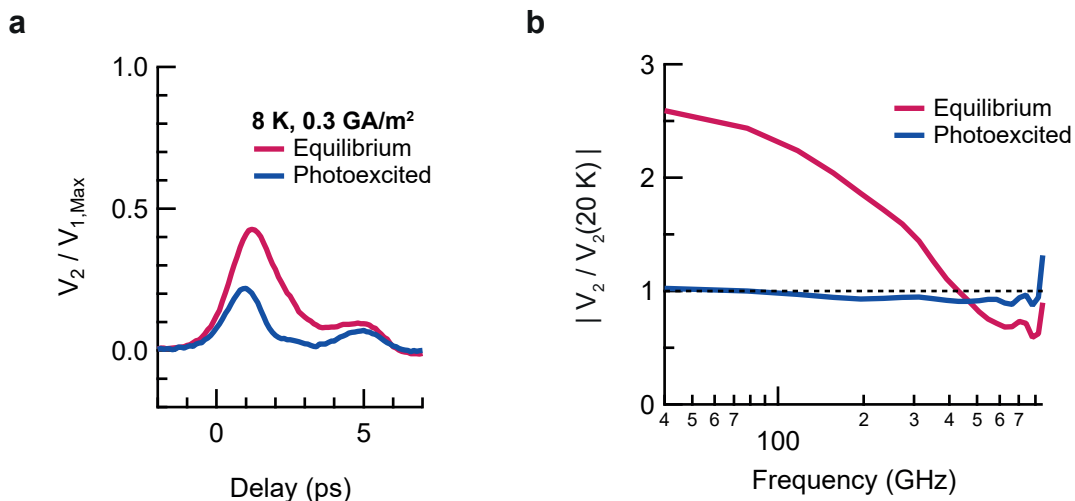


Figure 5.9: **Transmittance of photo-excited K_3C_{60} at 8 K.** a, Transmitted pulse V_2 in the time-domain for equilibrium (red) and 15 ps after mid-infrared excitation at 4 mJ/cm^2 (blue), with a peak current density of 0.3 GA m^{-2} . b, Fourier transform of the data in (a), normalised by the values at 20 K.

in equilibrium. Since the photon energy of the mid-infrared pulses is larger than the energy gap 2Δ in K_3C_{60} [118], disruption of superconductivity is expected upon optical excitation [160].

Fig. 5.9a displays the time-resolved transmitted current pulses upon photo-excitation at 8 K. This measurement was carried out with a small peak current of 0.3 GA m^{-2} . Upon photo-excitation, the magnitude of the transmitted pulses was reduced to approximately half of the equilibrium value, accompanied by a small phase shift associated with a reduced inductance.

An examination of the pulses in the frequency domain (Fig. 5.9b) shows that the photo-excited transport response was almost identical to the transport response of the equilibrium state at 20 K, which is consistent with a complete disruption of superconductivity.

5.5 Photo-excitation of K_3C_{60} above T_c

The same current pulse experiment was then conducted in the above- T_c photo-excited phase of K_3C_{60} . After photo-excitation with a fluence of 4 mJ/cm^2 , the amplitude of the transmitted pulse increased (Fig. 5.10a), corresponding to a reduction in the sample resistivity. The magnitude of the transmittance changes nevertheless point towards a finite resistivity after photo-excitation at 25 K, and the extracted $\text{Re}[\hat{Z}(\omega = 50\text{ GHz})]$ was found to be $206 \pm 1\ \Omega$ in the photo-excited state, compared

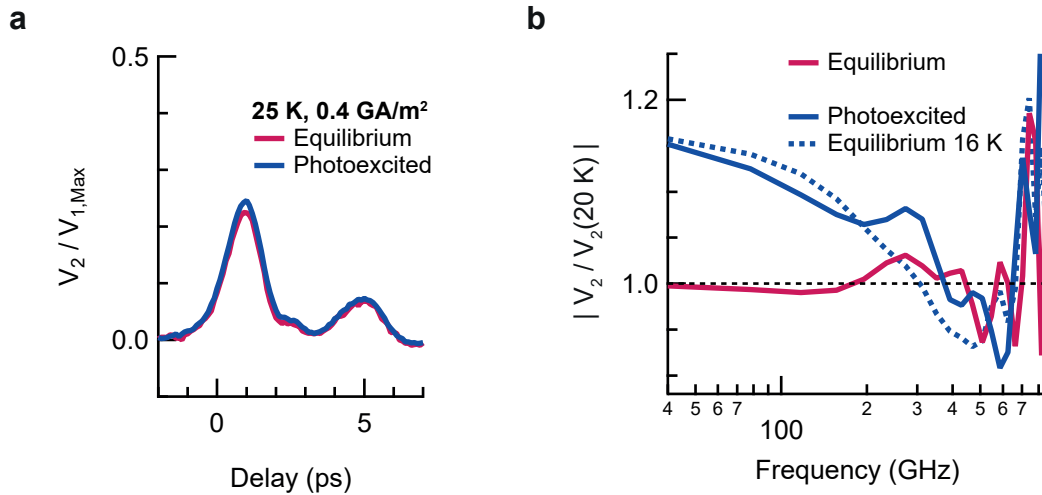


Figure 5.10: **Transmittance of photo-excited K_3C_{60} at 25 K.** **a**, Transmitted pulse V_2 in the time-domain for equilibrium (red) and 5 ps after mid-infrared excitation at 4 mJ/cm^2 (blue), with a peak current density of 0.4 GA m^{-2} . **b**, Fourier transform of the data in (a), normalised by the values at 20 K. The orange dashed line represents the equilibrium transmittance at 16 K.

with $256 \pm 2 \Omega$ in equilibrium. These values were obtained for the smallest current density of 0.4 GA m^{-2} .

From a cursory inspection of the data, a reduction in resistivity indicates a non-thermal excitation, since the sample possessed metallic properties in equilibrium. More information can be acquired by examining the transport properties in the frequency domain. The transmittance spectrum in the photo-excited state, shown in Fig. 5.10b, was found to closely resemble that of the equilibrium state at 16 K.

The current dependence in the photo-excited state was measured by increasing the magnitude of the current pulse, in which a similar trend was observed. Fig. 5.11a displays the normalised transmittance in equilibrium for current densities up to 3 GA/m^2 , alongside the transmittance of the photo-excited state for the same current densities. After photo-excitation with mid-infrared pulses at 25 K, the K_3C_{60} thin film exhibited nonlinear current-voltage behaviour that was quantitatively close to the current dependence in the equilibrium state at 16 K. In contrast to the nonlinear behaviour observed in equilibrium at 16 K and in the photo-induced state at 25 K, the equilibrium transmittance at 25 K was constant under the applied current. Furthermore, when photo-excited with a pulse at a much shorter wavelength of 515 nm, for which no superconducting-like optical properties were observed [32], the transmittance remained constant.

The similarity is reinforced when examining current-induced changes in the extracted real component of $\hat{Z}(\omega = 50 \text{ GHz})$, shown in Fig. 5.11b. Here, deviations from the

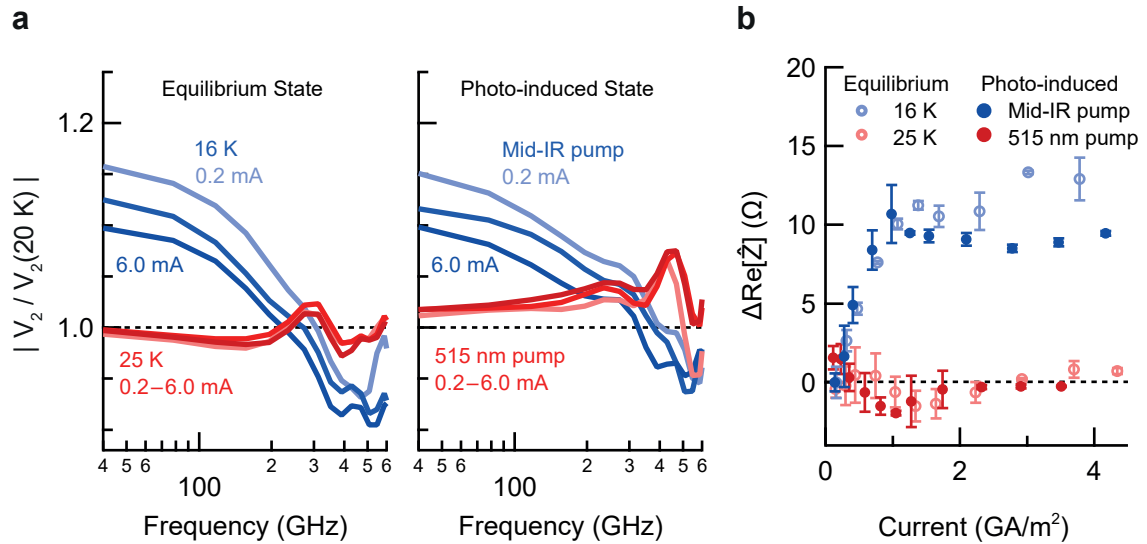


Figure 5.11: **Nonlinear current dependence in the photo-induced state.** **a**, Left: Current dependence of the transmittance in equilibrium at 16 K (blue) and 25 K (red). Right: Current dependence of the photo-induced state at 25 K with $7\ \mu\text{m}$ pump (blue) and 515 nm pump (red), both with $4\ \text{mJ cm}^{-2}$ fluence. **b**, Deviation in the real component of the impedance $\text{Re}[\hat{Z}]$ for increasing current, in equilibrium at 16 K (blue open circles) and 25 K (red open circles), as well as the photo-induced state at 25 K for excitation at $7\ \mu\text{m}$ (blue filled circles) and 515 nm (red filled circles). The error bars represent the standard error.

low-current impedance are plotted as a function of increasing current density. In both the equilibrium state at 16 K and the mid-infrared-driven state at 25 K, $\text{Re}[\hat{Z}]$ increased sharply with increasing current up to currents of $1\ \text{GA/m}^2$. Above this value, the impedance stabilised for both cases, plateauing for the photo-induced state and continuing to increase at a much slower rate for the equilibrium state at 16 K. On the other hand, photo-excitation at 515 nm pump wavelength did not induce nonlinear current-voltage behaviour, with $\text{Re}[\hat{Z}]$ remaining constant at all currents.

The pump-induced change in V_2 is plotted in Fig. 5.12 as a function of the delay between the mid-infrared pump and the current pulse probe. A fast initial rise in V_2 was observed immediately after excitation, consistent with terahertz reflectivity measurements [32, 33, 161]. Interestingly, V_2 continued to increase at a slower rate after the initial excitation, peaking at a delay of 15 ps, in contrast to the previous terahertz reflectivity measurements. After 15 ps, the changes in V_2 started to decay, but still persisted even up to long time delays, with a small effect still present at 2 ns delay. A $1/e$ decay time of $150 \pm 10\ \text{ps}$ was estimated for the photo-induced effect.

The quantitative similarities between the high-temperature photo-excited state and

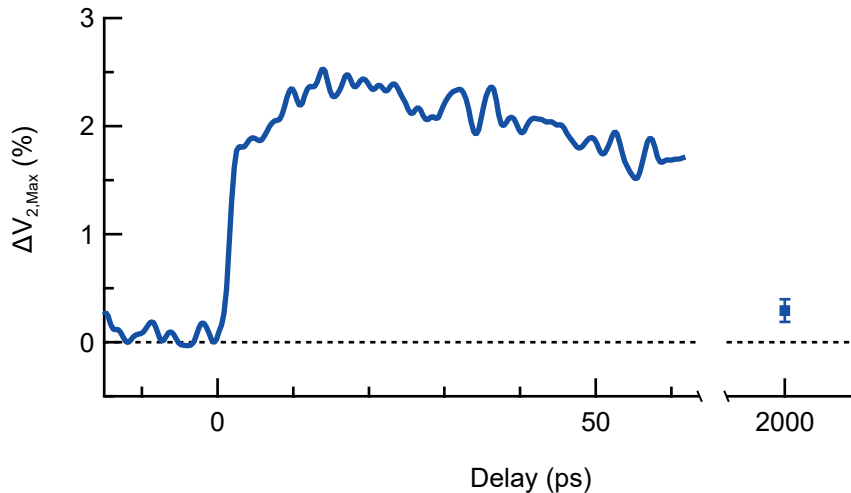


Figure 5.12: **Lifetime of the photo-induced state.** The photo-induced change in the peak of V_2 versus pump-probe delay, as a percentage of the reference peak.

the equilibrium state at 16 K reinforce the link drawn between the photo-excited state and the equilibrium superconducting state by previous optical measurements. At 16 K, thermal effects play a significant role in the transport properties of the equilibrium state, indicating that this may also be the case for the photo-excited state above T_c . This is particularly relevant in the case of granular systems like the one studied here, where phase-slips can be induced at weak links. One also cannot exclude the possibility that a fast quench after optical excitation results in an inhomogeneous state in which these effects would be more pronounced.

5.6 Summary

In this chapter, granular thin films of K_3C_{60} were probed with picosecond current pulses in both the equilibrium and photo-excited states. In the equilibrium state below T_c , an increase in the transmitted pulse magnitude was found when cooling through the superconducting transition, accompanied by a phase shift associated with the inductive transport in the superconducting state. A current dependence revealed how the critical current behaves on picosecond timescales, where Joule heating is negligible. A slower onset of resistivity was observed when compared to DC and nanosecond currents, and this picosecond critical current likely arose from current-induced phase slips.

From measurements in the finite-temperature regime $0.6T_c < T < T_c$, a finite resistivity was found even at low applied currents, which was attributable to the granu-

lar constitution of the thin film. In this temperature range, thermally-induced and current-induced phase-slips inhibit dissipationless transport across the weak links connecting adjacent grains. A nonlinear current-voltage behaviour was observed at all temperatures below T_c .

After photo-excitation above T_c , an enhancement in the sample transmittance was observed, from which a reduced but still finite resistivity was extracted for the photo-excited state. The enhanced transmittance was characterised by nonlinear current-voltage behaviour that quantitatively resembled the equilibrium state at a temperature of 16 K. Since transport in this finite-temperature regime below T_c is dominated by phase-slips at the grain boundaries, this result raises the important possibility that phase-slips play a significant role in the transport properties of the photo-excited state. The role of phase-slips could be exacerbated by heating resulting from the energy imparted by the excitation pulse, emphasising the need to investigate the carrier and thermal dynamics after the excitation. These effects will manifest in the voltage dynamics upon in-current photo-excitation, which is discussed in the following chapter.

Chapter 6

Ultrafast voltage dynamics in optically-driven K_3C_{60}

Parts of this chapter have been published in [162].

In the previous chapter, a parallel was drawn between the picosecond current-voltage behaviour in the photoinduced state to that in equilibrium at 16 K. In equilibrium, the sample behaviour in the temperature range 12–19 K is characteristic of a granular superconductor, where a broadened resistance-vs-temperature superconducting transition is observed and the superconducting state is characterised by nonlinear current-voltage behaviour. This suggests that the effects that play an important role in a granular superconductor at finite temperature in equilibrium, notably thermally-induced phase slips, may also be present in the photo-induced state above T_c .

Other important aspects to consider are the carrier and thermal dynamics associated with the formation of the photo-excited state. To begin to investigate this experimentally, we can extend the capabilities of the same optoelectronic platform to measure the voltage dynamics across the K_3C_{60} thin film when photo-excited in the presence of a current. Such a configuration allows physical properties such as time-varying inductances and fast carrier dynamics to be accessed more directly than with the previously-discussed picosecond-long current pulses. In this chapter, we will examine the use of photo-conductive switches to detect ultrafast voltage changes across the K_3C_{60} thin film upon in-current photo-excitation.

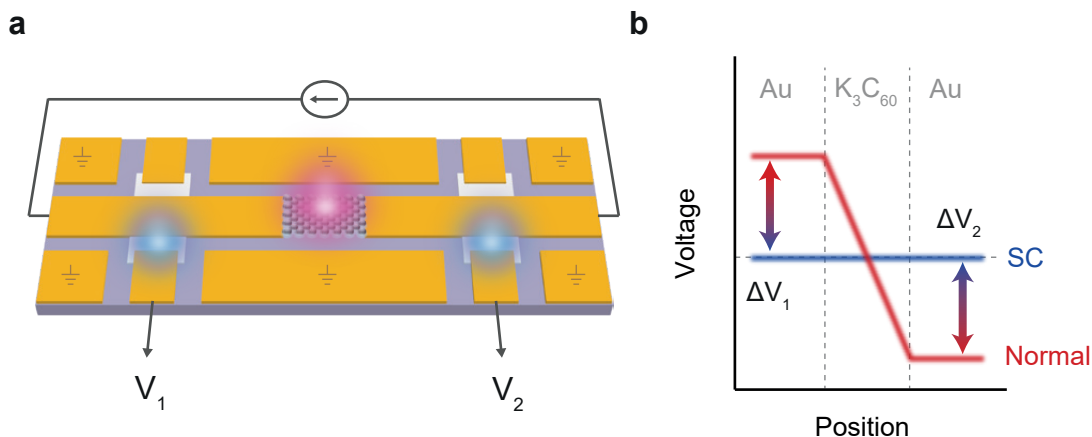


Figure 6.1: **Ultrafast voltmeter.** **a**, Device architecture. The K_3C_{60} thin film was biased with a quasi-DC current, and photo-excited with a 300 fs laser pulse at $7\ \mu\text{m}$ wavelength and $5\ \text{mJ cm}^{-2}$ fluence. The resulting changes in voltage (ΔV_1 and ΔV_2) were detected at the left and right switches. **b**, Sketch of the voltage profile across the device for ultrafast transitions between the metallic and superconducting states.

6.1 Experimental setup for ultrafast voltmeter measurements

6.1.1 Device layout

The device was operated as shown in Fig. 6.1a. A quasi-DC bias was applied to the K_3C_{60} thin film, the details of which are described in section 6.1.2. In the metallic state for $T > T_c$, this induced a voltage drop across the sample as sketched in Fig. 6.1b (red line). Upon photo-excitation with a 300 fs laser pulse at $7\ \mu\text{m}$ wavelength, changes to the conductivity of the sample resulted in changes to the voltage drop across the sample. On the ultrafast timescales probed in this measurement, the voltage in the device was effectively floating, so the voltage changes resulted in equal and opposite voltage pulses on either side of the sample. The voltage pulses then propagated away from the sample, where they could be detected at photo-conductive switches 1 and 2. The experiment was carried out by chopping the pump pulse, so the resulting measurements at switches 1 and 2 were proportional to the pump-induced change in voltage at the respective positions on the waveguide. These are henceforth referred to as ΔV_1 and ΔV_2 .

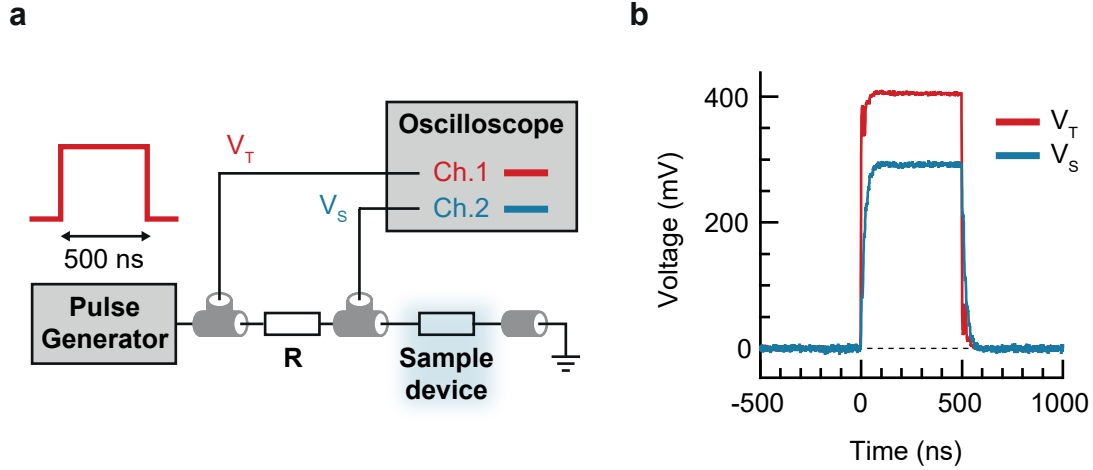


Figure 6.2: **Measurement of the applied quasi-DC current.** **a**, Measurement setup with a pulsed voltage bias of 500 ns duration. **b**, Voltage drop across the sample (V_S) and sample + resistor (V_T) as a function of time, for an applied voltage of 400 mV.

6.1.2 Applying the quasi-DC bias

To minimise current-induced heating in the sample, a true DC current bias was not used. Instead, flat-top 500 ns voltage pulses were applied to the K_3C_{60} sample prior to photo-excitation. The mid-infrared laser pulse was timed to arrive after the current through the sample had stabilised. To determine the current flowing through the sample under this voltage pulse, the setup depicted in Fig. 6.2a was utilised. A known resistance R was connected in series between the sample and the voltage pulse generator via coaxial cables. Resistances $R = 300 \Omega$ and $R = 100 \Omega$ were used for the measurements below T_c and above T_c , respectively. The voltages before the resistor V_T and before the sample device V_S relative to ground were monitored using an oscilloscope with a $1 \text{ M}\Omega$ input impedance. An example measurement for a pulsed bias with magnitude 400 mV is shown in Fig. 6.2b. The stabilised voltage values could be read out at a time of 300 ns. The current I flowing through the device could then be obtained using the equation

$$I = (V_T - V_S)/R. \quad (6.1)$$

With this technique, the thin-film could be biased with a quasi-DC current of up to 10 mA.

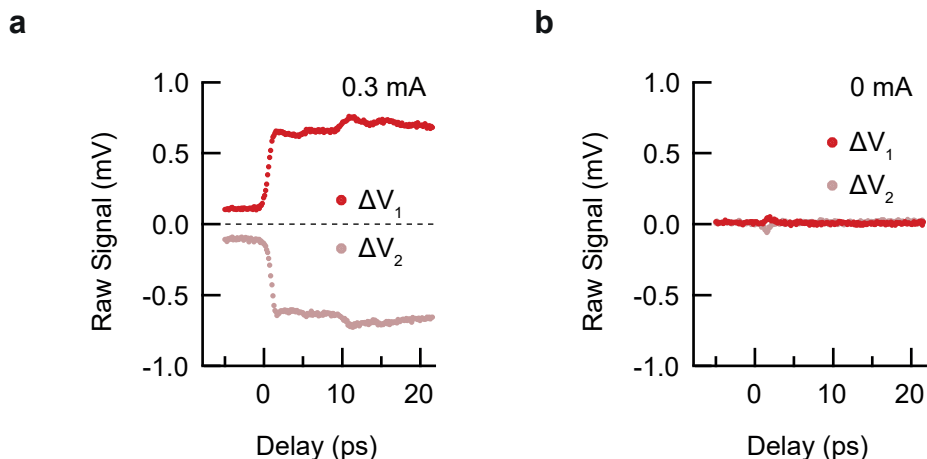


Figure 6.3: **Raw voltage transients for photo-excitation at 8 K.** **a**, Detected voltages ΔV_1 and ΔV_2 vs pump-probe delay, for an applied current of 0.3 mA. **b**, The same measurement in (a), but with no current applied.

6.2 Extraction of the on-chip voltage changes

The raw voltage transients obtained for photo-excitation below T_c are displayed in Fig. 6.3. To extract the photo-induced voltage dynamics originating from the K_3C_{60} thin film itself, additional contributions to the measured voltage were first isolated and subtracted.

6.2.1 Subtraction of zero-bias signal

The mid-infrared excitation pulse has finite intensity in the gap between the K_3C_{60} thin film and the ground plane of the waveguide. A coupling of the excitation pulse into the waveguide can therefore induce a transient electrical signal which would be detected concurrently with the photo-induced voltage changes across the sample. This effect can be isolated via a measurement with no quasi-DC current bias, and is shown in Fig. 6.3b. The voltage transients induced in this way were much smaller than the measured signal at finite bias, but they can nevertheless be removed by subtracting the 0 mA signal for each dataset from the data measured at finite current.

6.2.2 Subtraction of constant offset

A constant-in-time offset was observed in the raw data for each measurement. One must establish if this offset originates from trivial effects from the experimental setup

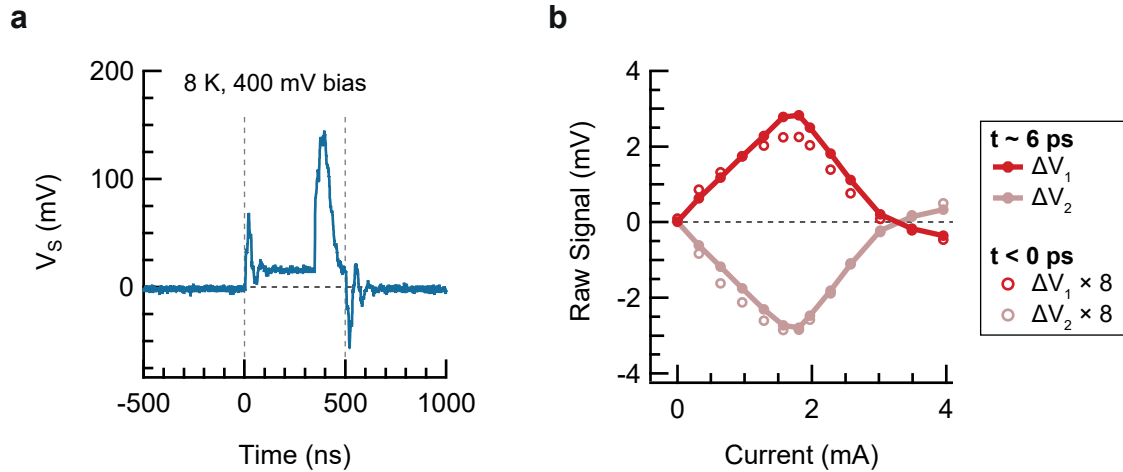


Figure 6.4: **Determining the origin of the offset.** **a**, Oscilloscope trace of the voltage across the device at 8 K for a 400 mV voltage pulse. The vertical dashed lines mark the start and end of the applied voltage pulse. The mid-infrared pump arrives at a time of ~ 300 ns. **b**, Transient voltage changes at 8 K (filled circles) and the offset before 0 ps delay (open circles).

and should be subtracted, or whether it contains relevant information related to time-averaged effects on the sample. Firstly, the time profile of the voltage changes at 8 K, measured with the oscilloscope setup from Fig. 6.2, are shown in Fig. 6.4a. After high-fluence excitation, the voltage changes relaxed within 200 ns, indicating that the offset is unlikely to be due to a long-lived heating effect. Examining the behaviour and dependencies of the offset can help to determine its origin. The offset before time-zero is shown in Fig. 6.4b as a function of the applied current for the measurements below T_c , alongside the voltage at 10 ps delay. The offset was proportional to the magnitude of the signal itself for this measurement, and this was found to be true for all measurements at every temperature. It is therefore likely that the offset results from signals flowing into the the detection line as leakage currents. This results in a voltage at the amplifier that is independent of the arrival time of the switch trigger pulse. To compensate for this, a constant offset was subtracted from the raw voltage transients.

6.2.3 Removing reflections

Reflections were also subtracted from the voltage transients. These can be seen as additional features in the time-domain data in Fig. 6.3a, and occur at the same time delays as those in the current pulse measurements in chapter 5, as expected. The optical microscope image of the device in Fig. 6.5 illustrates the origin of these reflections.

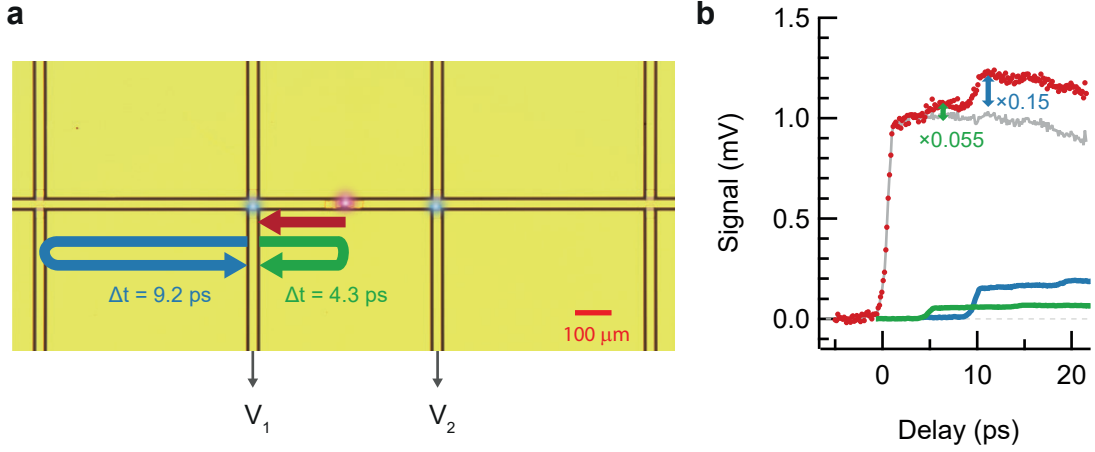


Figure 6.5: **Subtraction of reflections.** **a**, A zoomed-out microscope image of the device. The transient voltage changes propagate towards the detection switches (red arrow), after which reflections from the sample (green arrow) and from an additional pair of switches (blue arrow) occur with time offsets Δt of 4.3 ps and 9.2 ps, respectively. **b**, Illustration of the reflection removal procedure. An example data set at 8 K and 0.6 mA after subtraction of the zero-bias signal and voltage offset is displayed in red. The same measurement, offset in time by 4.3 ps (9.2 ps) and scaled by a factor 0.055 (0.15), is shown in green (blue). The green and blue traces are subtracted from the red trace to obtain the processed signal, shown in grey.

Without loss of generality for the discussion of reflections, we will consider the leftward propagating pulse. At switch 1, the pulse is partially reflected back towards the sample and partially transmitted. The reflected pulse is again reflected from the sample and returns to switch 1 (green arrow), while the transmitted pulse is reflected from the leftmost pair of switches (blue arrow) and returns to switch 1 at a later time.

The arrival time of the reflected pulses can be estimated from the device dimensions as follows: We consider the distance d_1 between switch 1 and the K_3C_{60} thin film, the distance d_2 between switch 1 and the leftmost pair of switches, and the effective relative dielectric constant of the coplanar waveguide on the sapphire substrate. We have $d_1 = 280 \mu\text{m}$ and $d_2 = 600 \mu\text{m}$. The effective relative dielectric constant of the coplanar waveguide on the sapphire substrate is given by

$$\epsilon_r = (\epsilon_{Al_2O_3} + 1)/2 = 5.27, \quad (6.2)$$

giving a pulse propagation speed $v = 0.43c$. The arrival times t_n for the reflections can be calculated as

$$t_n = \frac{2d_n}{v}, \quad (6.3)$$

giving 4.3 ps and 9.2 ps for the distances d_1 and d_2 , respectively. These values match

well with the features in the current pulse data in Fig. 5.5a and the voltage transients in Fig. 6.3a.

Copies of the measured data, scaled to 5% and 15% and offset in time by 4.3 ps and 9.2 ps, respectively, were subtracted. This resulted in a clear plateau when applied to the raw data in Fig. 6.3a, and the same procedure was used with the same parameters when subtracting reflections from every dataset.

6.2.4 Calibration of the transient voltage magnitudes

The experimental observable was a voltage at the lock-in amplifier, which was triggered at the chopping frequency of the mid-infrared pump pulse. Many conversion factors are compounded in the measurement scheme for detecting the on-chip voltage transients. The voltage changes in the signal line generated current pulses at the photo-conductive switches when the switches were triggered. The switches behave as a current source (see supplementary information of [14]), and the resulting current was converted to a voltage using a transimpedance amplifier and sent to the lock-in amplifier. If the voltage changes are in a regime where each of these conversion processes are linear, then we can combine them into one overall calibration factor κ_S for each switch S that relates the detected voltage V_d to the “bias” voltage in the waveguide V_b . We therefore define the calibration factor with the relation

$$V_b = \kappa_S \cdot V_d. \quad (6.4)$$

To determine the total conversion factor and calibrate the on-chip voltage transients, a DC voltage bias V_b was applied to the photo-conductive switch as depicted in Fig. 6.6a. The switch was illuminated with 515 nm laser pulses, which were chopped at a frequency of 1 kHz. Upon illumination, a voltage V_d was detected using the same amplification chain as used in the experiment. Fig. 6.6b and 6.6c display V_d versus V_b for switches 1 and 2 at a device temperature of 25 K. The switch response was linear for all temperatures, allowing us to obtain κ_S .

However, using the κ_S obtained from this measurement is expected to underestimate the magnitude of the voltage changes for two reasons. First, a travelling voltage pulse in the coplanar waveguide will be partially reflected from the photo-conductive switch. This can be accounted for by considering the transmittance of the switch. With the detected reflections discussed in section 6.2.3, we can determine that the second reflection of 15% magnitude (blue arrow in Fig. 6.5) involves the transmission from one pair of switches and the reflection from the other pair. It follows that the switch transmittance T for the transient voltages in the experiment can be estimated

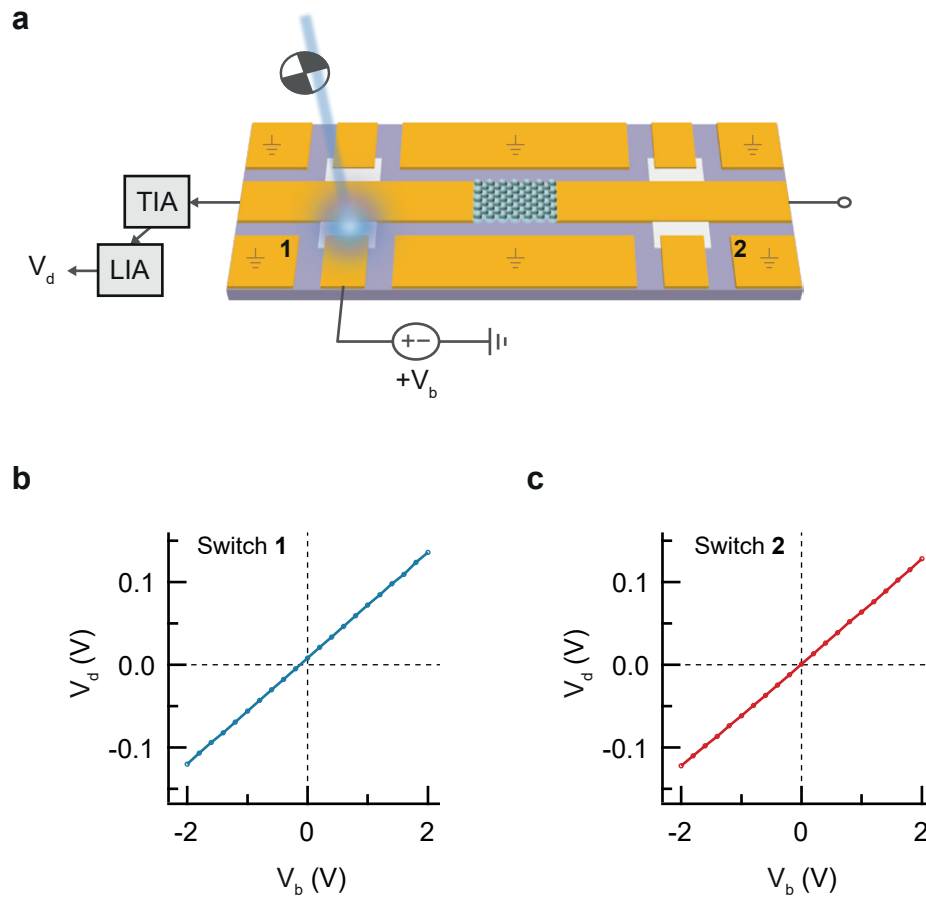


Figure 6.6: **Photoconductive switch calibration.** **a**, Measurement schematic. Switch 1 is biased with a DC voltage V_b and optically excited to launch current pulses into the waveguide. The total charge released in the current pulses is detected at the end of the signal line as a voltage V_d . **b**, Representative calibration curve for switch 1. **c**, Representative calibration curve for switch 2.

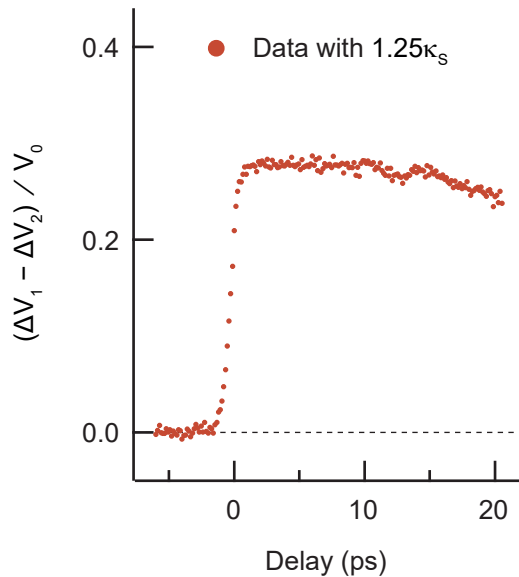


Figure 6.7: **Calibrated data.** Transient voltage changes at 8 K with a 0.3 mA bias, calibrated using a scaling factor of $1.25\kappa_S$.

given that $T(1 - T) = 0.15$, from which we find $T \approx 0.8$. We can therefore account for reflections by scaling the previously-obtained calibration factor as

$$\kappa_S \rightarrow \frac{\kappa_S}{0.8} = 1.25\kappa_S. \quad (6.5)$$

Second, the laser pulses incident on the switch will result in heating and an increase in DC conductivity of the switch, leading to a leakage current in addition to the one discussed when considering the offset. This effect will last as long as the thermal dissipation time of several nanoseconds. The leakage current therefore provides an additional contribution to V_d in the calibration measurement, meaning that the detected voltage with a DC bias is larger than with a several-picosecond voltage bias of the same magnitude. We therefore expect that a scaling factor slightly larger than $1.25\kappa_S$ is needed. A small systematic uncertainty is therefore likely to be present in the magnitude of the voltage changes.

6.3 Photoinduced voltage dynamics for $T < T_c$

The first measurements were carried out on the equilibrium superconducting state at temperatures below T_c . Above-gap optical excitation of a superconductor is expected

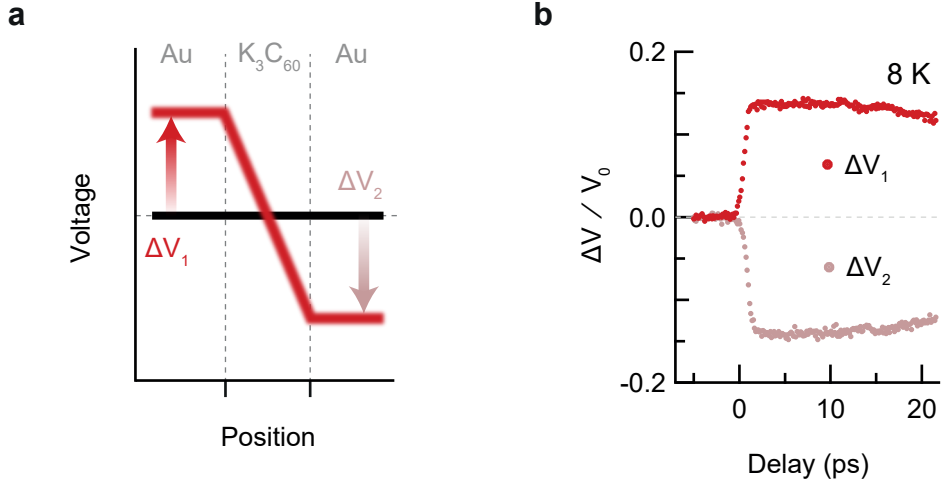


Figure 6.8: **Photo-induced voltage dynamics in K_3C_{60} ($T < T_c$) at high fluence.** **a**, Sketch of the voltage across the device. The voltage profile changes from the equilibrium superconducting state (black) to the disrupted state (red) upon photo-excitation. **b**, Pump-induced change in voltage on left (ΔV_1) and right (ΔV_2) of sample vs pump-probe delay, measured at 8 K, for a pump fluence of 5 mJ cm^{-2} . All voltages are normalized by a factor V_0 , which is defined for the measurements below T_c as the applied current multiplied by the sample resistance at 20 K.

to break Cooper pairs into unpaired electrons, disrupting superconductivity [99, 160]. The superconducting gap energy of K_3C_{60} has been measured to be 6 meV [118] — much smaller than the 180 meV photon energy of the excitation pulse. For in-current photo-excitation with this pump frequency, an increase in the voltage drop across the sample is therefore expected.

6.3.1 High-fluence excitation

We will first discuss the case of high-fluence excitation with 5 mJ cm^{-2} mid-infrared pulses, which will result in a large temperature increase, bringing the sample temperature above T_c . A complete disruption of superconductivity is therefore expected, and the corresponding changes to the voltage are depicted schematically in Fig. 6.8a.

The measured ΔV_1 and ΔV_2 are plotted in Fig. 6.8b as a function of pump-probe delay. All voltages are normalised by a factor V_0 , which, for the measurements below T_c , is defined as the applied current multiplied by the sample resistance at 20 K. ΔV_1 exhibited a step-like increase with a rise time of approximately 1 ps. ΔV_2 displayed equal and opposite behaviour to ΔV_1 . For the given direction of applied current, this indicates an increase in the total voltage drop across the sample, consistent with disruption of superconductivity.

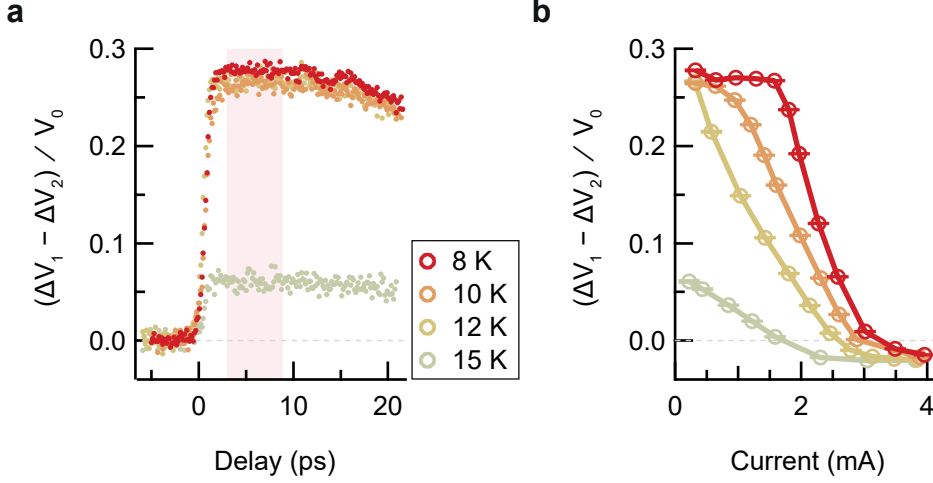


Figure 6.9: **Temperature and current dependence of the photo-induced voltage dynamics ($T < T_c$) at high fluence.** **a**, Pump-induced change in voltage drop across sample vs pump-probe delay, measured at 8 K, 10 K, 12 K, and 15 K, with an applied current of 0.3 mA. **b**, Pump-induced change in voltage drop across sample vs applied current, measured at the same temperatures as in (a). Each data point is the mean value of the time-trace within a 6 ps window centred at 6 ps delay. The error bars represent the standard error of the mean change in voltage drop. All voltages are normalized in the same way as in Fig. 6.8.

The total pump-induced change in voltage drop can be calculated as $\Delta V_1 - \Delta V_2$. Fig. 6.9a displays the pump-induced change in voltage drop across the K_3C_{60} thin film as a function of pump-probe delay for different temperatures below T_c . Fig. 6.9b displays the same normalised change in voltage drop as a function of applied current. Each data point in the current dependence is the mean value of the time-trace within a 6 ps window centred at 6 ps delay. At 8 K, the pump-probe signal was constant with the applied current up until 2 mA, above which the signal exhibited a step-like decrease. The step was consistent with the critical current of the equilibrium superconducting state displayed in Chapter 4. Upon increasing the temperature, the pump-probe signal began to decrease at lower currents and the step broadened.

For photo-excitation below T_c with such a large pump fluence, the step-like response can be attributed to heating of the K_3C_{60} thin film due to the excitation pulse. Here, above-gap excitation of the condensate disrupts superconductivity, and a large amount of energy is deposited into the formed quasiparticles and the lattice. The redistribution of this energy results in an increase in the temperature of the thin film, preventing the reformation of the condensate. Only after the imparted thermal energy has been extracted from the system (which occurs for films of this thickness on a timescale of nanoseconds [163]), can the condensate reform and the voltage return to its before- t_0 value.

At higher temperatures closer to T_c , the magnitude of the voltage change reduced. Since the resistivity of the equilibrium superconducting state becomes finite at temperatures approaching T_c , the resistivity change upon disruption of superconductivity is smaller, which is consistent with the temperature dependence of the voltage changes. Similarly, the same trend is observed in the current dependence, which results from the onset of resistivity due to the current in the superconducting state before t_0 .

6.3.2 Low-fluence excitation

An above-gap excitation with very small excitation fluence will introduce much less thermal energy into the system, ensuring that the sample temperature remains below T_c , while still disrupting the condensate. The voltage dynamics of K_3C_{60} when photo-excited with a fluence of $<100 \mu\text{J cm}^{-2}$ are displayed in Fig. 6.10. Here, a bipolar, nonthermal voltage response was observed. Such a voltage response is consistent with a kinetic inductive photoresponse, which is understood to originate from the destruction and subsequent recovery of the Cooper pairs [163–167]. The kinetic inductance L_K arises from the inertia of the charge carriers in a conductive medium, and is given by

$$L_K = \frac{m}{nq^2} \cdot \frac{L}{A}, \quad (6.6)$$

for charge carriers with mass m , charge q , and density n , where L is the sample length in the direction of the current and A is the cross-sectional area. A change in carrier density will therefore change the kinetic inductance. When this occurs in an applied current I , this generates an additional voltage V_K given by

$$V_K = I \cdot \frac{dL_K}{dt} = -\frac{mL}{q^2 A} \cdot \frac{1}{n^2} \cdot \frac{dn}{dt}. \quad (6.7)$$

For a decrease in superfluid density, V_K is positive. Similarly, V_K becomes negative for a recovery of the superfluid density [166]. A two-fluid model was used to fit the data under a time-variable superfluid density. For weak excitation, Cooper-pair-breaking and quasiparticle relaxation can be captured using a Rothwarf-Taylor time profile, followed by an exponential decay for the recovery of the superfluid [168–170]. Time constants for pair-breaking $\tau_{PB} = 0.8 \pm 0.1$ ps and for the recovery of superconductivity $\tau_R = 50 \pm 5$ ps were obtained from the fits, as well as a peak quasiparticle fraction of 0.88.

Fig. 6.11 displays the current dependence of the low-fluence voltage dynamics. At the lowest current of 0.2 mA, the bipolar, nonthermal voltage response is observed.

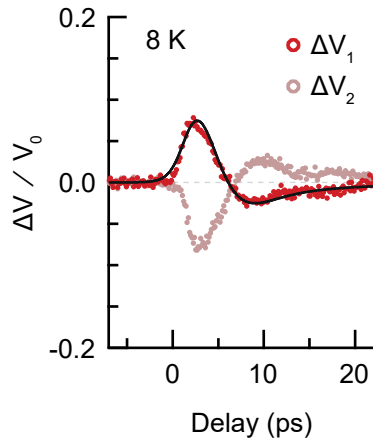


Figure 6.10: **Photo-induced voltage dynamics in K_3C_{60} ($T < T_c$) at low fluence.** Pump-induced change in voltage on left (ΔV_1) and right (ΔV_2) of sample vs pump-probe delay, measured at 8 K, for a pump fluence of $< 100 \mu\text{J cm}^{-2}$. All voltages are normalized in the same way as in Fig. 6.8.

As the current is increased up to 2.1 mA, the amplitude of the negative response reduces, until the voltage change resembles an increase followed by an exponential decay. By increasing the current further still, beyond the critical current of the equilibrium superconducting state, the voltage change reduces in magnitude to zero.

The changes in the negative voltage response that occur within the range 0.2–2.1 mA can be attributed to Joule heating arising from the photo-excited quasiparticles, which slows the recovery of the condensate. Furthermore, the suppression of the voltage response altogether which occurs for $I > 2.1$ mA is consistent with the suppression of the superconducting state at super-critical currents, which occurs before the arrival of the excitation pulse.

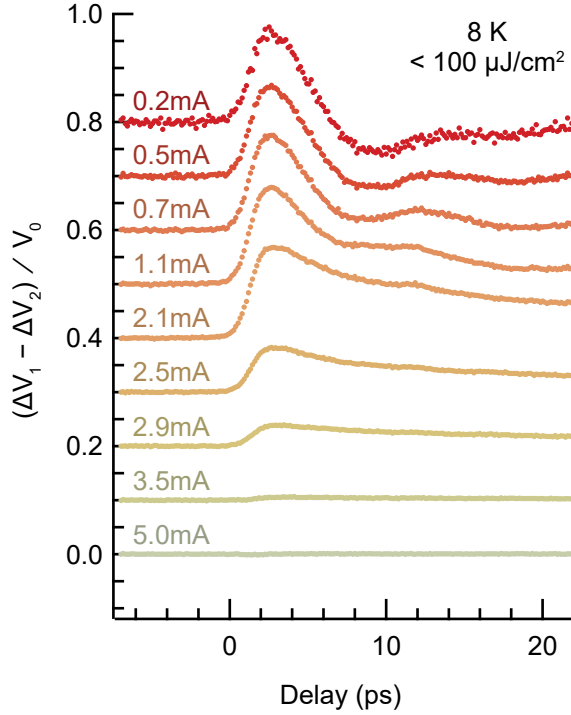


Figure 6.11: **Current dependence of the low-fluence voltage dynamics** ($T < T_c$). Traces are offset by a constant value for readability.

6.4 Photoinduced voltage dynamics for $T > T_c$

We now turn our attention to the photo-induced non-equilibrium state at temperatures above T_c . In the same experimental configuration, the voltage drop across the sample before photo-excitation corresponded to its equilibrium state resistance as sketched in Fig. 6.12a. Based on the enhancement of optical conductivity found in K_3C_{60} powder samples under the same optical excitation [32, 33], a reduction in the voltage drop is now expected.

The measured ΔV_1 and ΔV_2 for photo-excitation at 25 K are plotted in Fig. 6.12b as a function of pump-probe delay. All voltages are normalised by a factor V_0 , which, for the measurements above T_c , is defined as the applied bias multiplied by the sample resistance at the measurement temperature. A first glance at the data shows that the signs of ΔV_1 and ΔV_2 were reversed compared to the measurements below T_c , indicating a reduction in voltage drop upon photo-excitation and an increase in the conductivity of the sample. ΔV_1 became negative after photo-excitation, with dynamics present on two timescales; a fast, negative spike was present immediately after time-zero, which was followed by a slow decrease of ~ 10 ps duration. ΔV_2 displayed equal and opposite behaviour to ΔV_1 .

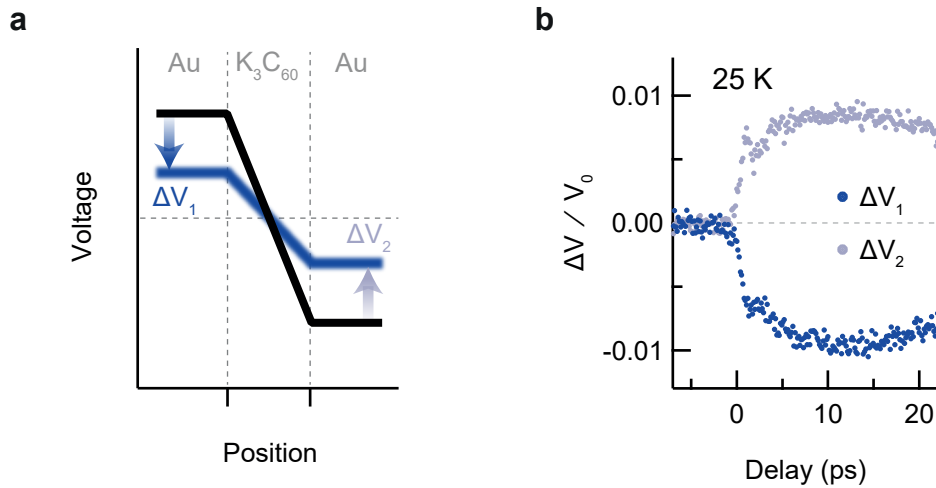


Figure 6.12: **Photo-induced voltage dynamics in K_3C_{60} ($T > T_c$).** **a**, Sketch of the voltage across the device. The voltage profile changes from the equilibrium metallic state (black) to the nonequilibrium state (blue) upon photo-excitation. **b**, Pump-induced change in voltage on left (ΔV_1) and right (ΔV_2) of sample vs pump-probe delay, measured at 25 K, for a pump fluence of 5 mJ cm^{-2} . All voltages are normalized by a factor V_0 , which is defined for the measurements below T_c as the applied current multiplied by the equilibrium sample resistance at the measurement temperature.

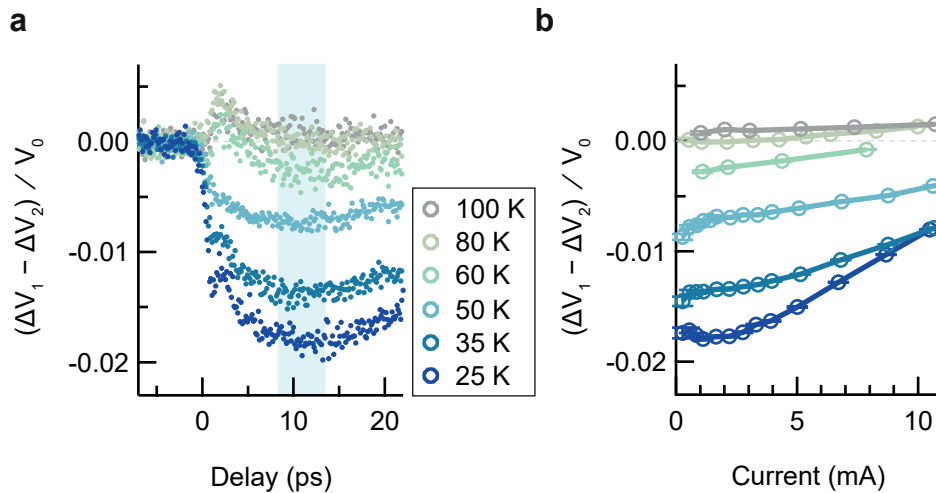


Figure 6.13: **Temperature and current dependence of the photo-induced voltage dynamics ($T > T_c$).** **a**, Pump-induced change in voltage drop across sample vs pump-probe delay, measured at 25 K, 35 K, 50 K, 60 K, 80 K, and 100 K, with an applied current of 1 mA. **b**, Pump-induced change in voltage drop across sample vs applied current, measured at the same temperatures as in (a). Each data point is the mean value of the time-trace within a 5 ps window centred at 11 ps delay. The error bars represent the standard error of the mean change in voltage drop. All voltages are normalized in the same way as in Fig. 6.12.

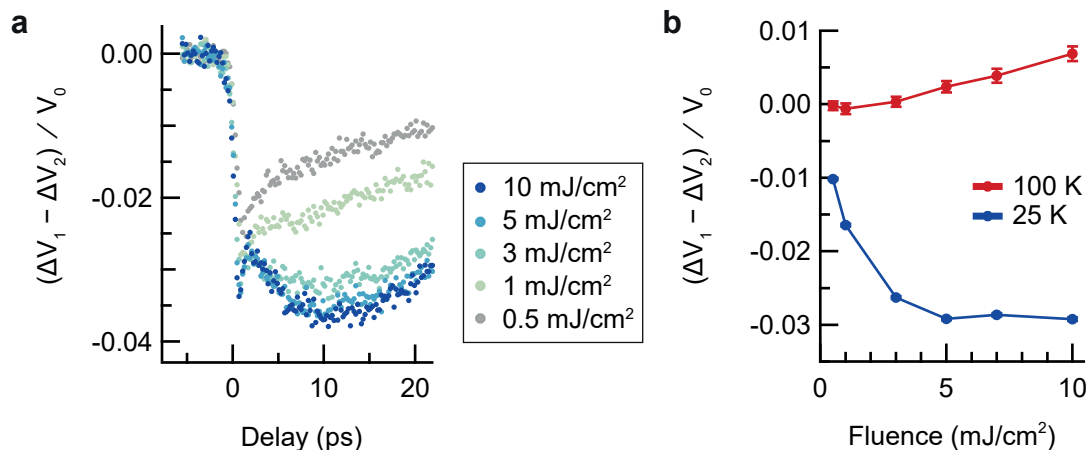


Figure 6.14: **Fluence dependence of the photo-induced voltage dynamics** ($T > T_c$). **a**, Voltage dynamics for mid-infrared pump fluences of 0.5–10 mJ cm⁻² at a base temperature of 25 K. The response saturates at around 3 mJ cm⁻². **b**, Voltage changes averaged in a 6 ps window around 10 ps delay for base temperatures of 25 K (blue) and 100 K (red).

Fig. 6.13a displays the pump-induced change in voltage drop across the K_3C_{60} thin film as a function of pump-probe delay for different temperatures above T_c . The magnitude of the voltage change decreased with increasing temperature, until the sign of the response was reversed at 80 K. The positive response at high temperatures also differed in its dynamics; only a single rise and decay was observed. Fig. 6.13b displays the voltage change as a function of the applied current. Each data point in the current dependence is the mean value of the time-trace within a 5 ps window centred at 11 ps delay. At 25 K, linear behaviour in current was observed for small currents. Above 2 mA, the signal became nonlinear with the applied current. Upon increasing the temperature, the onset of the nonlinear behaviour was shifted to lower currents. The nonlinear effect was also reduced alongside the signal magnitude at higher temperatures; the positive voltage change at 100 K was linear in current across the whole measurement range.

The fluence dependence of the photo-induced voltage dynamics is displayed for 25 K in Fig. 6.14a. At low fluences, the optically-induced changes decayed just after excitation, with the longer-timescale dynamics only emerging above fluences of 1 mJ cm⁻². Eventually, above 3 mJ cm⁻², the voltage response saturates. The voltage changes at 25 K are compared to those at 100 K in Fig. 6.14b. Notably, the fluence-dependent voltage changes at 25 K base temperature exhibited no upturn at high fluence, while the 100 K voltage changes increased with increasing fluence, which reinforces a non-thermal interpretation of the response at 25 K.

To understand the experimental data above T_c , we first consider the fast, negative

voltage spike found on short timescales after excitation. This fast response was importantly not present when measuring the sample transmittance with picosecond current pulses (Fig. 5.12), and this discrepancy is consistent with the fast response originating from a time-dependent kinetic inductance. Here, a negative $V \propto dL/dt$ arises from an increase or transfer of carrier density n . The negative voltage spike in the $T > T_c$ data was significantly faster than the positive spike in the low-fluence, $T < T_c$ data (Fig. 6.10), which can be understood as the changes in n occurring on the timescale of the excitation pulse duration.

On longer timescales, the voltage changes settled to a finite-resistivity state after about 10 ps, consistent with the measurements in Chapter 5. In both measurement schemes, the photo-induced state above T_c exhibited nonlinear current-voltage behaviour. The nonlinear current-voltage behaviour observed here was qualitatively different from that seen in the current pulse experiment in Chapter 5. In the ultrafast voltmeter measurement scheme, the current was applied before photo-excitation. This means that current-induced changes to the before-time-zero state that may affect the photo-induced dynamics, for example a suppression of the photosusceptibility, cannot be excluded.

At temperatures above 80 K, the sign of the voltage response reversed. The crossover temperature of 80 K is also the temperature below which superconducting fluctuations have been observed in K_3C_{60} pellets [171].

Before analysing the data within the framework of light-induced superconductivity, it is important to consider a range of physical processes that may arise from the use of granular thin film samples, which are discussed in the following section.

6.5 Discussion on the $T > T_c$ photo-induced state

The enhancement in conductivity in the ultrafast transport measurements presented here was found to be smaller than the σ_0 extrapolated from previous optical measurements on powder samples [32, 33, 110, 111]. The thin films used here were formed of well-connected grains after growth on the sapphire substrate. To account for the differences between the optical measurements on powder samples and the transport measurements on granular thin films, we first consider the impact of the substrate. Substrate-induced strain has been shown to affect the ground state in few-layer K_xC_{60} fullerides [172]. However, given the thickness of the samples used in this work (100 nm), the substrate is unlikely to have a significant impact. Indeed, the observed equilibrium resistivity and critical temperature in the films grown for this work were consistent with literature values [137, 138].

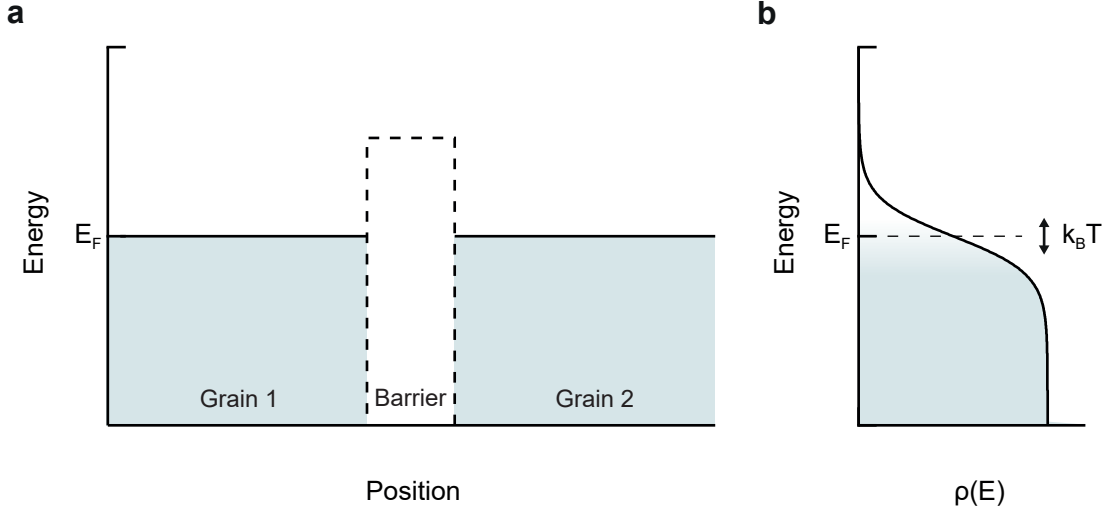


Figure 6.15: **Tunnelling at grain boundaries.** **a**, Energy diagram sketch of a potential boundary between two metallic grains. **b**, Fermi-Dirac distribution at finite temperature.

In Chapter 5, the current-voltage behaviour in the photo-induced state was found to exhibit considerable overlap with the equilibrium superconducting state at 16 K, where grain boundaries are understood to significantly affect the transport response. One important aspect to consider is the potential barriers arising from the grain boundary structure, resulting in the localisation of carriers. Localisation is a broad term, referring to various phenomena that inhibit carrier diffusion. It encompasses weak localisation, a precursor to Anderson localisation arising from wave interference between scattering paths [173–175], as well as Mott localisation due to the Coulomb interaction [176]. In this case, we will consider a much simpler form, where inter-grain transport is impeded in a granular material by a potential barrier that is present between adjacent grains. Fig. 6.15a depicts an energy diagram sketch of two grains separated by a potential barrier, while Fig. 6.15b shows a Fermi-Dirac distribution of carrier energies at finite temperature.

To understand how potential barriers influence transport, we consider the probability of an electron tunnelling from one grain to the other. In this simplified picture, assuming the grains are metallic, the probability of an electron of energy E to tunnel from Grain 1 to Grain 2 is proportional to both the probability that an electron is present at that energy in Grain 1, and the probability that a vacancy is available at that energy in Grain 2. We can write this as

$$\bar{P}(E, 1 \rightarrow 2) \propto \left(\frac{1}{e^{\beta(E-E_F)} + 1} \right) \left(1 - \frac{1}{e^{\beta(E-E_F)} + 1} \right), \quad (6.8)$$

where $\beta = 1/k_B T$. Integrating over all energies gives a quantity proportional to the

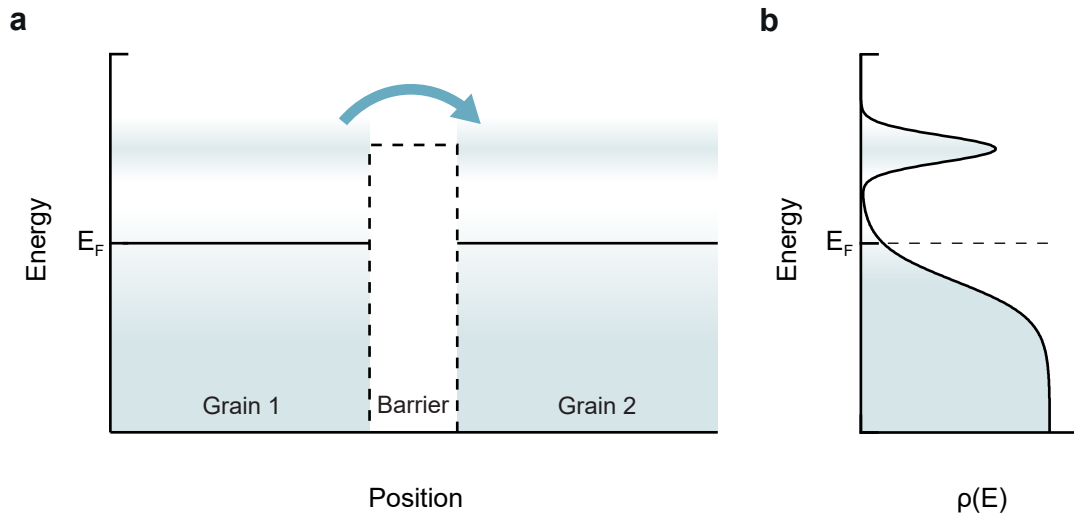


Figure 6.16: **Grain boundaries with a non-thermal carrier distribution.** **a**, Energy diagram sketch of a potential boundary between two metallic grains. The arrow indicates hopping over the potential barrier. **b**, Sketch of a non-thermal electronic distribution. The excited carriers experience greater mobility.

total tunnelling probability,

$$P(1 \rightarrow 2) \propto \int_0^\infty \bar{P} dE \propto \left[-\frac{1}{\beta (e^{\beta(E-E_F)} + 1)} \right]_0^\infty = \frac{1}{2} k_B T. \quad (6.9)$$

Unsurprisingly, we find that carriers are entirely localised at 0 K, and the tunnelling probability, and hence conductivity, must increase with increasing temperature.

The contribution of potential barriers to the material resistivity depends on the size and interconnectivity of the grains. In granular samples with small grains, intergrain transport is a dominant factor and sample resistivity increases with decreasing temperature [138]. Similarly, in single-crystal samples this effect is absent, and transport is dominated by the intrinsic material properties [137]. In the granular thin films studied in this work, the resistance versus temperature (Fig. 4.10a) indicated a transport response that was largely dominated by the metallic character of the bulk. Nevertheless, a small upturn in the resistivity was observed close to the superconducting transition, suggesting that localisation effects do in fact contribute to the transport properties of these films.

Now, we consider an excited system with a non-thermal carrier distribution, such as the one depicted in Fig. 6.16. In this picture, the excited carriers are able to overcome the potential barrier between grains via hopping or tunnelling, resulting in the expected increase in conductivity. Specifically, the excited carriers would provide an additional contribution to the conductivity that should not significantly

depend on temperature, resulting in an additional constant term in the tunnelling probability $P(1 \rightarrow 2)$. The lifetime of the excited state would be determined by the relaxation rate of the carriers in this case.

However, a simple picture of excited carriers does not suffice to explain several important features of the optically-driven phase of K_3C_{60} . In the transport measurements, the nonlinear current-voltage behaviour and sign-change at 80 K exclude the possibility of a trivial excitation. Furthermore, the pump energy of 177 meV is far from any inter-band transitions found from DFT calculations [62], and intra-band transitions are expected to relax on femtosecond timescales [177], much shorter than the 150 ps lifetime found in Chapter 5.

The exclusion of simple excitation processes leads one to consider other means by which transport may be enhanced in granular samples. Although a simple excitation mechanism is not possible, grain boundaries might still contribute to the transport properties of the excited state, which may be determined in future experiments through the use of monocrystalline samples. Nevertheless, the observation of nonlinear current-voltage behaviour (Chapter 5) and gapped optical features in the excited state [32, 33, 110] point towards a superconducting-like excited state. In optical measurements, recent work has revealed a broad resonance in the photo-susceptibility at the pump energy of 41 meV, which coincides with radial molecular modes of the C_{60} [111]. A likely theoretical mechanism underlying the excited state has been explored in the same work based on the displacement of infrared-active phonon modes, whereby displacement of the T_{1u} modes lifts the π -orbital degeneracy, favouring the formation of a spin-singlet pair on each molecule [111, 178].

If the transport response indeed originates from a photo-induced superconducting state, it is possible that the slow dynamics found in the voltage changes result from the stabilisation of thermal phase fluctuations. Since high-fluence photo-excitation will increase the temperature of the sample, the phase must be highly disordered upon photo-excitation. As such, the initial resistivity of the photo-excited state at early delays would be left unchanged from that of the metallic state. As the phase thermalises, the rate of thermally-induced phase slips decreases, and the resistivity drops on a timescale of several picoseconds [179, 180]. Nevertheless, the phase slip rate at longer delays would be significant due to lattice heating, resulting in finite resistivity in the long-lived state after photo-excitation. This is treated in much more detail in the simulations discussed in section 6.6.

6.6 Simulations of the voltage dynamics

Simulating superconductivity for an excited granular system requires accounting for a dynamical superfluid fraction in addition to changes in temperature, which heavily affect transport across grain boundaries. This is illustrated in the data for high-fluence excitation at $T < T_c$ (Fig. 6.9), which cannot be explained in a simple, homogeneous model of superconductivity. To see this clearly, consider the results close to T_c , where a reduction in signal magnitude was observed. This is related to the broadened superconducting transition observed in equilibrium DC measurements (Fig. 4.10), following the onset of finite resistivity in the superconducting state. As discussed in Chapter 5, finite resistivity in a granular superconductor arises from thermally-induced phase slips at grain boundaries [155], which must be accounted for in order to reconstruct the voltage dynamics upon optical excitation. In this section, we will develop a circuit model that can suitably capture the physics of a granular superconductor undergoing fast changes in superfluid density, first applying it to the $T < T_c$ case, and then examining its potential relevance to the $T > T_c$ excited state.

6.6.1 Granular two-fluid model

An illustration of a two-fluid system of Cooper pairs and resistive carriers in a granular material is depicted in Fig. 6.17a. When modelling the behaviour of the superconducting condensate in such a system, we consider the following: The Cooper pairs can tunnel across grain boundaries, thereby experiencing the Josephson effect [181, 182]. When $I > I_c$, the additional current must be carried by normal carriers that experience resistance. Finally, there is a capacitance across the grain boundary. The combination of these factors gives rise to a resistively- and capacitively-shunted Josephson junction (RCSJ) model [155, 183, 184].

A model for the superfluid in the granular thin film is therefore constructed by considering an RCSJ model in series with the kinetic inductance, with the latter representing the intra-grain transport. The two-fluid behaviour is modelled by including a resistive channel in parallel with the superfluid channel, representing the normal carriers. The circuit diagram for this granular two-fluid model is shown in Fig. 6.17b, where the granular superfluid channel is shown in blue, and the resistive channel in orange.

In the experiment, the K_3C_{60} thin film is photo-excited in a quasi-DC bias. The resulting voltage pulses are subject to the impedance of the coplanar waveguide as they propagate towards the detection switches. However, the quasi-DC current

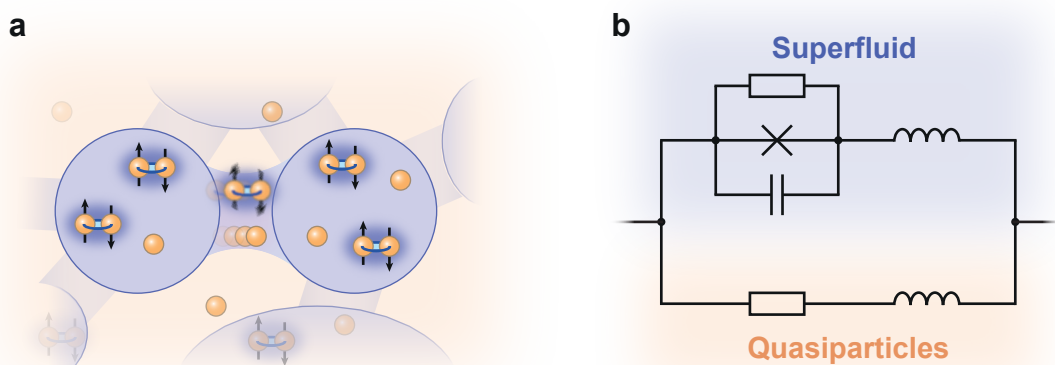


Figure 6.17: **Two-fluid model of a granular superconductor.** **a**, Sketch of a granular material with Cooper pairs and quasiparticles. Cooper pairs tunnel across grain boundaries, whilst thermal phase fluctuations disrupt phase coupling between the different superconducting grains. **b**, Circuit diagram of the granular two-fluid model used to represent the K_3C_{60} sample. The superfluid channel (highlighted in purple) consists of a typical RCSJ model extended to include the kinetic inductance of the superconducting grains. The resistive quasiparticle channel is highlighted in orange.

experiences only the resistance of the sample and the (negligible) resistance of the gold conduction line. To model this, the granular two-fluid model was incorporated into an extended model to separate the AC and DC components of the voltage. The equivalent circuit model for this is displayed in Fig. 6.18. The applied bias I_{DC} was separated from the sample model via low-pass filters, and the waveguide impedance Z_W was connected via high-pass filters on each side of the granular two-fluid model. Since the two sides of the waveguide share a common ground, they can be connected together as shown on the right hand side of the figure.

Determination of model parameters

The normal channel resistance was given by

$$R_N = \frac{R_0}{f_N}, \quad (6.10)$$

where R_0 is the resistance of the K_3C_{60} thin film above T_c , and f_N is the fraction of normal carriers. The resistance in the RCSJ model R_J is also given by the sample resistance above T_c [155] and was extended to a two-fluid regime with the equation

$$R_J = \frac{R_0}{f_S}, \quad (6.11)$$

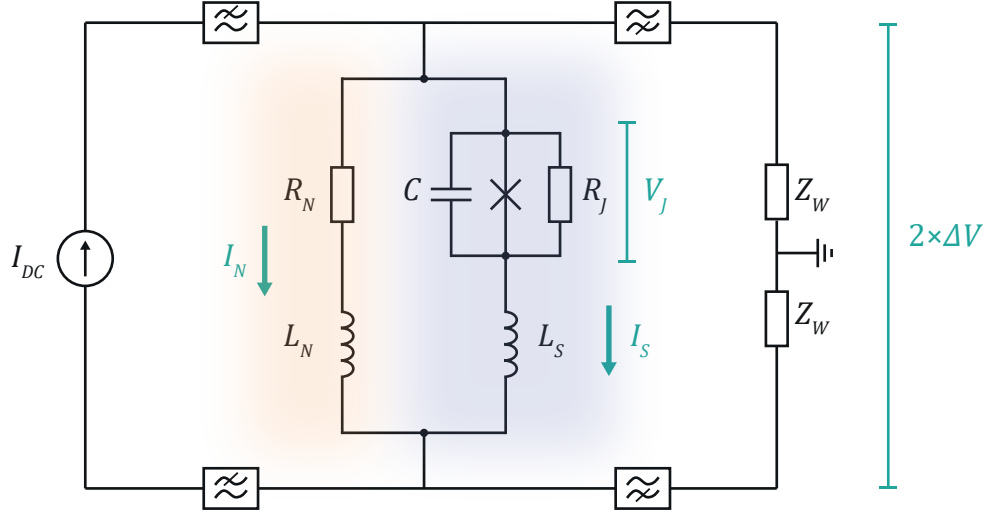


Figure 6.18: **Expanded circuit model including waveguide and current source.** The frequency dependence of the waveguide impedance is approximated using low-pass filters for the DC component, and high-pass filters for the picosecond voltage transients.

where f_S is the superfluid fraction, and $f_N + f_S = 1$.

The kinetic inductance for each channel was determined in the same way, following

$$L_N = \frac{L_0}{f_N} \quad (6.12)$$

and

$$L_S = \frac{L_0}{f_S}, \quad (6.13)$$

where L_0 is the kinetic inductance of the thin film with $f_S = 1$. L_0 was estimated using equation 6.6; for a K_3C_{60} thin film with a carrier density $n = 1.6 \times 10^{25} \text{ m}^{-3}$, as extracted from optical reflectivity measurements [32], and with dimensions of our thin film, we obtain $L = 22 \text{ pH}$.

The capacitance C for a single grain boundary was estimated by considering the boundary geometry to be $\sim 10^{-17} \text{ pF}$.

The critical current of the Josephson junction I_c was considered to follow the relation [43]

$$I_c(T) = I_c(0 \text{ K}) \left[1 - \left(\frac{T}{T_c} \right)^{3/2} \right]. \quad (6.14)$$

It was then assumed to also scale proportionally to the superfluid density as

$$I_c(T, f_S) = I_c(T) f_{S, \text{Norm}}, \quad (6.15)$$

where $f_{S, \text{Norm}}$ is the superfluid fraction normalised by the superfluid density at temperature T for temperatures below T_c .

Scaling to a single grain

The granular K_3C_{60} sample was modelled as an array of grains. The grain size was estimated from atomic force microscopy measurements discussed in chapter 4 to be $100 \text{ nm} \times 100 \text{ nm} \times 20 \text{ nm}$. A full array for the $20 \mu\text{m} \times 20 \mu\text{m} \times 100 \text{ nm}$ sample could therefore be built from a $200 \times 200 \times 5$ structure of grains. We will write the number of grains along the length, width, and height of the sample as $N_L = 200$, $N_W = 200$, and $N_H = 5$, respectively, where the length is defined parallel to the waveguide.

Each grain (and boundary) can be modelled using a copy of the granular two-fluid model in 6.17b. Instead of modelling the full array of grains, the process can be simplified by calculating voltage transients for a single grain and scaling the currents, voltages, and circuit elements appropriately. All currents, including the critical current of the Josephson junction, were scaled down to a single grain as

$$I_{\text{grain}} = \frac{I_{\text{sample}}}{N_W N_H}. \quad (6.16)$$

Similarly, resistances and inductances were scaled following

$$R_{\text{grain}} = \frac{N_W N_H}{N_L} R_{\text{sample}}, \quad (6.17)$$

$$L_{\text{grain}} = \frac{N_W N_H}{N_L} L_{\text{sample}}. \quad (6.18)$$

Finally, the calculated voltage changes for a single grain were scaled up to the full sample using

$$\Delta V_{\text{sample}} = N_L \Delta V_{\text{grain}}. \quad (6.19)$$

Circuit equations

The following circuit equations were derived from the granular two-fluid model:

$$2\Delta V = I_N R_N - V_0 + L_N \frac{dI_N}{dt} + I_N \frac{dL_N}{dt}, \quad (6.20)$$

$$I_N R_N + L_N \frac{dI_N}{dt} + I_N \frac{dL_N}{dt} = V_J + L_S \frac{dI_S}{dt} + I_S \frac{dI_S}{dt}, \quad (6.21)$$

and

$$I_{DC} - \frac{2\Delta V}{Z_W} = I_N + I_S, \quad (6.22)$$

where V_0 is the initialised voltage across the sample, and other parameters are defined as shown in Fig. 6.18. The voltage V_J refers to the voltage drop across the resistively- and capacitively-shunted Josephson junction, which was governed by the following equations [155]:

$$\frac{dV_J}{dt} = \frac{1}{C} \left(I_S - I_c \sin \theta - \frac{V_J}{R_J} - i_n(t) \right), \quad (6.23)$$

and

$$\frac{d\theta}{dt} = \frac{2eV_J}{\hbar}, \quad (6.24)$$

where θ is the difference in the phase of the superconducting order parameter between the two grains. The phase difference was assumed to be randomly initialised for each simulation, since coherent effects are not expected for a granular superconductor. $i_n(t)$ represents the noise current associated with thermal phase fluctuations. A white-noise frequency spectrum was used with a zero-mean Gaussian amplitude distribution. The full-width half-maximum of the amplitude distribution was determined by comparing the equations of motion for the Josephson phase with the Langevin equation [185], giving

$$\sqrt{\langle i_n(t) \cdot i_n(t') \rangle} = \sqrt{2k_B T / R_J} \cdot \delta(t - t'). \quad (6.25)$$

The circuit equations were rearranged for the numerical calculations as follows:

$$\begin{aligned} \frac{d\Delta V}{dt} = \frac{Z_W(L_N + L_S)}{L_N L_S} & \left\{ - \left[2 + \frac{L_N}{Z_W(L_N + L_S)} \frac{dL_S}{dt} \right] \Delta V \right. \\ & + \left[R_N + \frac{dL_N}{dt} - \frac{L_N}{L_N + L_S} \left(R_N + \frac{dL_N}{dt} + \frac{dL_S}{dt} \right) \right] I_N \\ & \left. + \frac{I_{DC} L_N}{L_N + L_S} \frac{dL_S}{dt} + (V_J - V_{J0} - V_0) \right\}, \quad (6.26) \end{aligned}$$

$$\begin{aligned} \frac{dI_N}{dt} = \frac{1}{L_N + L_S} & \left[- \frac{L_S}{Z_W} \frac{d\Delta V}{dt} - \frac{1}{Z_W} \frac{dL_S}{dt} \Delta V \right. \\ & \left. - \left(R_N + \frac{dL_N}{dt} + \frac{dL_S}{dt} \right) I_N + I_{DC} \frac{dL_S}{dt} \right], \quad (6.27) \end{aligned}$$

and

$$\frac{dV_J}{dt} = \frac{1}{C} \left[I_{DC} - \frac{\Delta V}{Z_W} - I_c \sin \theta - \frac{V_J}{R_J} - i_n(t) \right], \quad (6.28)$$

with

$$\frac{d\theta}{dt} = \frac{2eV_J}{\hbar} \quad (6.29)$$

remaining unchanged.

6.6.2 Pump-induced heating in a two-temperature model

In order to determine the amplitude of the thermal phase fluctuations in the photo-excited regime, we must consider the effect of the excitation pulse on the carrier temperature. This was done through the use of a two-temperature model [163, 167] of the form

$$c_e \frac{dT_e}{dt} = -\frac{c_e}{\tau_{e-ph}} (T_e - T_{ph}) + P(t) \quad (6.30)$$

$$c_{ph} \frac{dT_{ph}}{dt} = \frac{c_e}{\tau_{e-ph}} (T_e - T_{ph}) - \frac{c_{ph}}{\tau_{es}} (T_{ph} - T_0), \quad (6.31)$$

where T_e and T_{ph} are the electron and phonon temperatures, respectively, c_e and c_{ph} are the electronic and phononic specific heat capacities, τ_{e-ph} is approximately the electron-phonon scattering time, τ_{es} is the 'escape time', representing the rate of heat transfer from the thin film to the substrate, and $P(t)$ is the rate of energy absorbed at time t .

The absorbed fraction of the mid-infrared pulse energy was estimated from the optical properties [32] and the device geometry using a three-layer multi-reflection model. This provided an absorbed fraction of 30%. The absorbed energy E_{in} for a laser pulse of fluence F and spot radius r was therefore given by

$$E_{in} = 0.3\pi r^2 F. \quad (6.32)$$

The incident power was then calculated by taking a Gaussian pulse with FWHM of 300 fs with time-integral equal to E_{in} .

For films of tens of nanometres in thickness, the τ_{es} is several nanoseconds in duration and is not important on the timescales of this experiment. A value of 3 ns was used here. Measurements in other metals have found values for τ_{e-ph} on the order of 1 ps [179, 186]. In the simulations reported here, $\tau_{e-ph} = 0.8$ ps provided the best fit to the data.

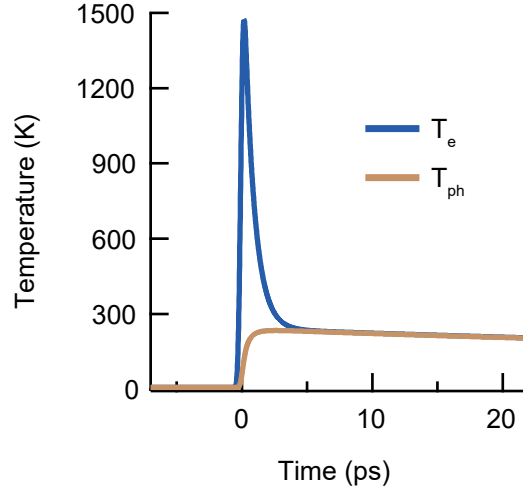


Figure 6.19: **Two-temperature model.** Calculated electron temperature (T_e) and lattice temperature (T_{ph}) versus time for photo-excitation of the K_3C_{60} thin film with a Gaussian laser pulse of 5 mJ cm^{-2} fluence.

The value for c_{ph} was obtained from fits to calorimetry data [187], where c_{ph} was approximated as linear within the range 6–300 K. Similarly, using

$$c_e = \gamma T_e \quad (6.33)$$

with $\gamma = 3.7 \times 10^{-2} \text{ J kg}^{-1} \text{ K}^{-2}$ [187] provided the electronic specific heat capacity.

The calculated T_e and T_{ph} for a 5 mJ cm^{-2} excitation pulse are displayed in Fig. 6.19. The electron temperature rises sharply during the excitation, and the lattice temperature increases on longer timescales due to electron-phonon scattering, with the electron and lattice temperatures stabilising at $\sim 300 \text{ K}$ after several picoseconds. The thermal phase fluctuations in the granular two-fluid model simulation were assumed to follow the electron temperature calculated here.

6.6.3 Simulations for $T < T_c$

The voltage dynamics for high-fluence excitation at temperatures below T_c were simulated using the granular two-fluid model. Before time-zero, the superfluid density n_S was assumed to depend on temperature following the relation [43]

$$n_S \propto 1 - \left(\frac{T}{T_c} \right)^4, \quad (6.34)$$

and to reduce from $n_S(T)$ to zero at time-zero, as shown in Fig. 6.20a. The calculated voltage transients are shown in Fig. 6.20b and Fig. 6.20c as functions of time and current, respectively, for different temperatures below T_c . The temperature and current dependencies display strong agreement with the experimental results discussed in section 6.3. In particular, both the near- T_c and high-current regimes were quantitatively well-captured by the model, allowing for carrier dynamics to be analysed without neglecting thermal dynamics in inhomogeneous superconductors.

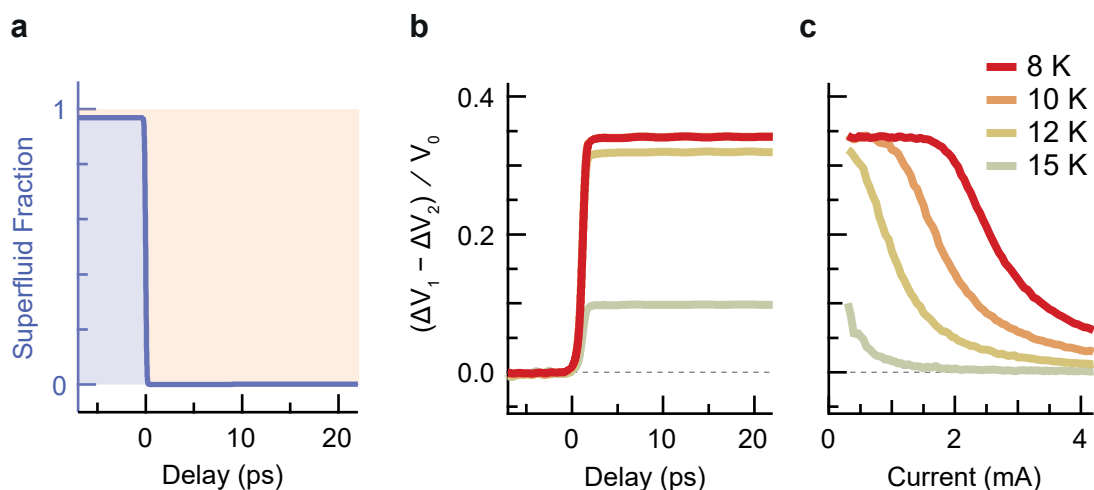


Figure 6.20: **Disruption of superconductivity in a granular two-fluid model.** **a**, Time-dependent superfluid density used in the disruption simulation at 8 K. The superfluid fraction is assumed to reduce to zero at 0-ps delay. **b**, Simulated change in voltage drop across sample vs delay, for base temperatures of 8 K, 10 K, 12 K, and 15 K, with an applied current of 0.3 mA. **c**, Simulated change in voltage drop across sample vs applied current, for the same base temperatures as in (b). All voltages are normalized by a factor V_0 , which is defined for the measurements below T_c as the applied current multiplied by the sample resistance at 20 K.

To demonstrate that the granular two-fluid model reduces to a simple, homogeneous two-fluid model for low temperatures and low excitation fluences, the low-fluence data at 8 K was fitted and the results displayed in Fig. 6.21. As before, a Rothwarf-Taylor time profile was used for the Cooper-pair breaking and quasiparticle relaxation, followed by an exponential decay. The granular two-fluid model produced a slightly improved fit, and time constants for pair-breaking $\tau_{PB} = 0.6 \pm 0.2$ ps and for the recovery of superconductivity $\tau_R = 30 \pm 5$ ps were obtained. The time constants found here are comparable to those found for the homogeneous two-fluid model fit, with slight differences likely arising from a small-but-finite thermal contribution that is not accounted for by the homogeneous model.

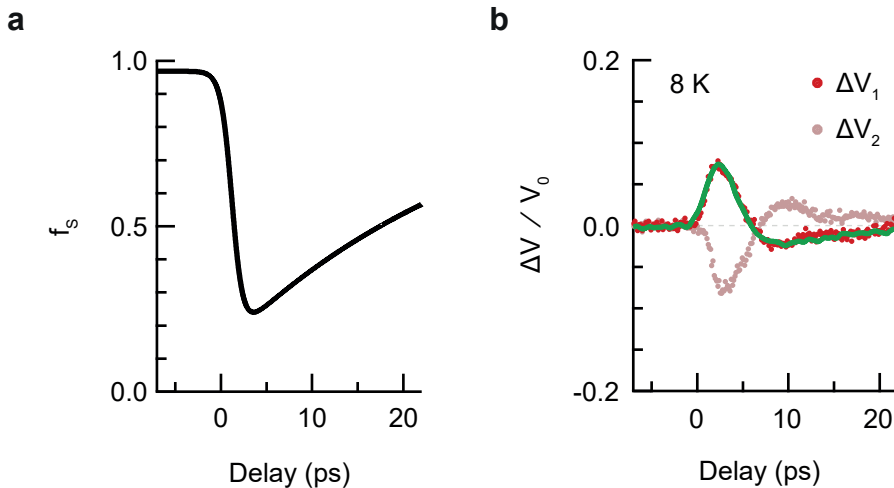


Figure 6.21: **Granular two-fluid model fit to the low-fluence data.** **a**, Time-dependent superfluid fraction with $\tau_{PB} = 0.6$ ps and $\tau_R = 30$ ps. **b**, The same data as in Fig. 6.10 (red and pink data points), fitted with the granular two-fluid model (green line) using the superfluid fraction shown in (a).

6.6.4 Simulations for $T > T_c$

An onset of superconductivity was treated similarly to the disruption simulations in the previous section. Here, the superfluid density was assumed to increase from zero to a finite value at time-zero, with a rise time of 300 fs (the duration of the excitation pulse), and to subsequently decay exponentially in time (Fig. 6.22a). The decay time of 150 ps was determined from fits to the lifetime data in section 5.5. The circuit simulation at each temperature was used to fit the slow response in the data at 10 ps delay, using the peak superfluid fraction at time-zero as a fitting parameter. Other parameters, such as the rise and decay times for the superfluid fraction, were held constant between temperatures.

The fits are displayed in Fig. 6.22b. The two-timescale dynamics seen in the measurements are also present in the simulations, with a fast, negative voltage spike appearing at time-zero, followed by a slower dip in voltage. The superfluid fraction fitting parameter is plotted in Fig. 6.22c as a function of temperature, and decreases with increasing temperature. For temperatures of 80 K and above, the experimental data no longer display a reduction in resistivity and these temperatures are represented with a superfluid fraction of zero in place of a fit.

In the granular two-fluid model, a large increase in carrier temperature is estimated upon high-fluence excitation. Since thermal fluctuations lead to phase-slips at the grain boundaries, these results are indicative of a trade-off between the strength of the nonlinear drive, which would favour a large photo-induced effect, and the induced heating, which is detrimental to coherent intergrain tunnelling.

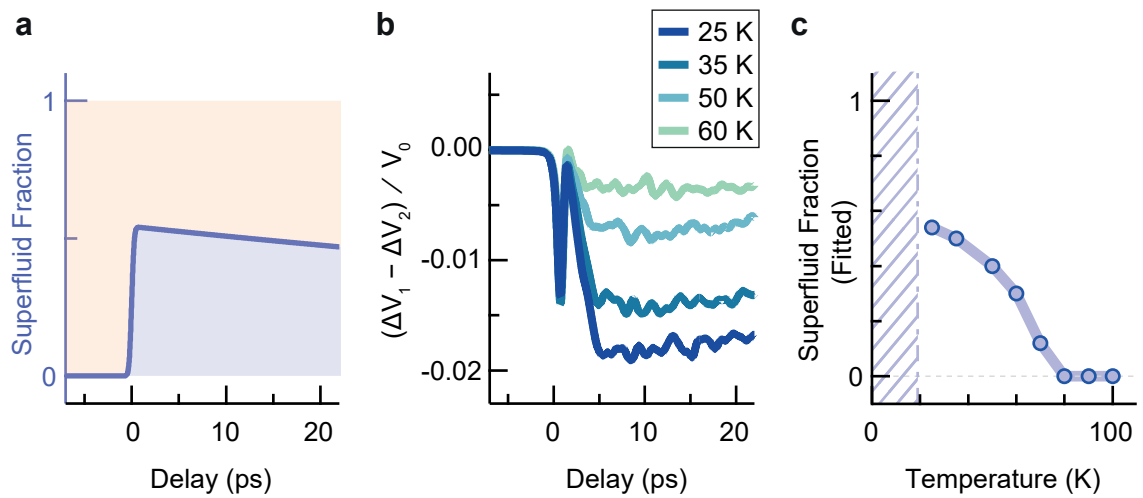


Figure 6.22: **Photo-induced superconductivity in a granular two-fluid model.** **a**, Time profile of the superfluid density for the simulation of the photo-excited state. **b**, Simulated change in voltage drop across sample vs delay, using peak superfluid fraction as the fitting parameter, for base temperatures of 25 K, 35 K, 50 K, and 60 K, with an applied current of 1 mA. All voltages are normalized by a factor V_0 , which is defined for the measurements above T_c as the applied current multiplied by the equilibrium sample resistance at the measurement temperature. **c**, Light-induced ‘superfluid fraction’ vs temperature as obtained from the fitting procedure described in the text. The blue symbols indicate granular two-fluid model fits to the voltage data on the granular thin films. The shaded region indicates temperatures below the equilibrium T_c .

6.7 Summary

In this chapter, the ultrafast voltage dynamics across the K_3C_{60} thin film were investigated upon mid-infrared excitation in both the $T < T_c$ and $T > T_c$ regimes.

For temperatures below T_c , a photo-induced increase in voltage drop consistent with disruption of superconductivity was observed, in concordance with the results from Chapter 5. In particular, for high-fluence excitation, a step-like voltage increase was observed, which likely resulted from two factors: above-gap optical excitation causing direct breaking of the Cooper pairs, followed by a large temperature increase suppressing pair reformation. Upon increasing the temperature or current, entering the finite-resistance regime while remaining below T_c , a reduction in photo-induced voltage change was observed.

Upon low-fluence excitation, the temperature increase of the charge carriers could be reduced significantly, such that the carrier temperature remains below T_c . In this case, a bipolar, non-bolometric voltage response was observed, which was attributable to changes in the kinetic inductance resulting from two-fluid carrier dynamics. By incorporating a model for granular superconductivity into a two-fluid model, the photo-induced changes in both regimes could be quantitatively reproduced, and timescales for pair-breaking and recovery could be extracted for the case of low-fluence excitation.

For temperatures above T_c , a photo-induced reduction in voltage drop was observed, with voltage dynamics on two timescales. A fast negative voltage spike was observed just after excitation, indicating a change in the kinetic inductance due to a shift in carrier density. Furthermore, a slow negative voltage change was observed over a ~ 10 ps timescale. These photo-induced voltage changes were found to be suppressed by increasing the applied current, and by increasing the temperature, with a reversal in sign observed for base temperatures above 80 K. By assuming an onset of superfluid density upon thermal excitation, the granular two-fluid model of superconductivity could reproduce the data and allowed for an estimation of the photo-induced superfluid fraction at each measurement temperature.

Chapter 7

Conclusions

7.1 Summary

In this thesis, we have discussed a series of ultrafast transport experiments in the optically-driven phase of K_3C_{60} thin films [145, 162]. In these experiments, ultrafast electronic devices were constructed from terahertz waveguides and photo-conductive switches to measure the transport properties of driven K_3C_{60} thin films with sub-picosecond time resolution. The devices allowed for two separate ultrafast transport experiments to be carried out. In the first experiment, discussed in Chapter 5, the photo-conductive switches were used to launch sub-picosecond current pulses into the coplanar waveguide. By detecting the transmitted pulse on the other side of the sample, a time-resolved ‘snapshot’ of the sample’s transport properties could be obtained, enabling an investigation of the current-voltage characteristics of the photo-induced state. Below T_c , measurements with these ultrashort current pulses in the equilibrium superconducting state allowed a critical current measurement to be obtained in the absence of heating effects. There, a slowed onset of resistivity was observed, with nonlinear current voltage behaviour found at all temperatures below T_c . Above T_c , an enhanced frequency-dependent transmittance was observed upon mid-infrared excitation, which could be partially suppressed by increasing the probe current. Strikingly, both the transmittance and its current-dependence were found to closely resemble the equilibrium state at 16 K, just below T_c .

In the second transport experiment, the ultrafast voltage dynamics across the K_3C_{60} thin film were measured upon in-current excitation. Below T_c , where above-gap excitation disrupts the equilibrium superconducting state, a sharp step was seen after high-fluence excitation, which was modelled as disruption of superconductivity for all measurement temperatures through the development of a granular two-fluid model. Low-fluence excitation allowed for the inductive response associated with the disruption and subsequent recovery of superconductivity to be observed, and,

with the granular two-fluid model, pair-breaking and recovery times for K_3C_{60} could be extracted. Above T_c , a small but long-lived reduction in voltage drop was observed upon photo-excitation, with a negative spike on short timescales that was attributable to changes in the kinetic inductance of the sample, indicative of an increase or transfer of carrier density. Furthermore, the sign of the voltage changes was reversed above a temperature of 80 K, corresponding to the disappearance of superconducting fluctuations in K_3C_{60} pellets [171].

The full set of voltage dynamics could be quantitatively reproduced using the same granular two-fluid model of superconductivity under a fast *onset* of superfluid density. In the model, thermally-induced phase slips at grain boundaries explained the suppression of dissipationless transport, revealing competition between the strength of the nonlinear excitation and the pump-induced thermal effects at the grain boundaries.

7.2 Outlook

The experiments in this work were performed on polycrystalline thin films of K_3C_{60} . While a non-trivial excited state could be clearly established in these films, experimentation on *monocrystalline* samples could reveal even more about the underlying physics of this state. In such samples, a macroscopically coherent state would exhibit a strongly enhanced transport response in the absence of grain boundaries, while any transport response associated only with enhanced tunnelling would be suppressed.

An investigation into Rb_3C_{60} , which has a larger critical temperature than K_3C_{60} and is closer to the Mott-insulating state, could provide great insight into a possible link between superconducting fluctuations and the photo-induced state, provided Rb_3C_{60} exhibits similar photo-induced properties. To do this, a Nernst effect measurement in Rb_3C_{60} would be necessary to search for the presence and temperature scaling of superconducting fluctuations. Following that, a comparison with the temperature scaling of photo-induced voltage changes could be used to determine if a positive correlation exists between the two parameters. Experiments on other alkali-doped fullerides would also allow a phase diagram to be mapped out for the photo-induced state in this family of materials.

Finally, the transport studies of the optically driven state in K_3C_{60} necessitated the development of non-conventional, high-frequency electronic devices, capable of probing transport properties in non-equilibrium states on picosecond timescales.

The platform developed here can be extended to other materials and provides interesting inroads towards potential applications of ultrafast quantum phenomena. In particular, the use of MBE-grown thin-films in this work presents an exciting opportunity to incorporate a broad range of bespoke thin films into ultrafast transport devices. Looking ahead, the capabilities of these devices can be extended via multi-pulse excitation of the photo-conductive switches, which offers the possibility to excite narrow-band pulses into the waveguide. This could open up the potential for on-chip coherent excitation, paving the way towards completely integrated systems exploiting the ultrafast control of quantum materials.

Bibliography

- [1] J. Bardeen and W. H. Brattain. “The Transistor, A Semi-Conductor Triode”. *Physical Review* **74**, 230–231 (1948).
DOI: 10.1103/physrev.74.230.
- [2] W. Shockley. “A Unipolar “Field-Effect” Transistor”. *Proceedings of the IRE* **40**, 1365–1376 (1952).
DOI: 10.1109/jrproc.1952.273964.
- [3] H. Ibach and H. Lüth. *Solid-State Physics: An Introduction to Principles of Materials Science*. Springer Berlin Heidelberg, 2009.
DOI: 10.1007/978-3-540-93804-0.
- [4] D. H. Auston. “Picosecond optoelectronic switching and gating in silicon”. *Applied Physics Letters* **26**, 101–103 (1975).
DOI: 10.1063/1.88079.
- [5] D. H. Auston. “Impulse response of photoconductors in transmission lines”. *IEEE Journal of Quantum Electronics* **19**, 639–648 (1983).
DOI: 10.1109/JQE.1983.1071904.
- [6] B. Keimer and J. E. Moore. “The physics of quantum materials”. *Nature Physics* **13**, 1045–1055 (2017).
DOI: 10.1038/nphys4302.
- [7] P. Seidel, editor. *Applied superconductivity*. en. Encyclopedia of Applied Physics. Weinheim, Germany: Wiley-VCH Verlag, 2015.
- [8] C. Nayak, S. H. Simon, A. Stern, M. Freedman, and S. Das Sarma. “Non-Abelian anyons and topological quantum computation”. *Reviews of Modern Physics* **80**, 1083–1159 (2008).
DOI: 10.1103/revmodphys.80.1083.
- [9] P. A. Lee. “From high temperature superconductivity to quantum spin liquid: progress in strong correlation physics”. *Reports on Progress in Physics* **71**, 012501 (2007).
DOI: 10.1088/0034-4885/71/1/012501.

- [10] D. N. Basov, R. D. Averitt, and D. Hsieh. “Towards properties on demand in quantum materials”. *Nature Materials* **16**, 1077–1088 (2017).
DOI: 10.1038/nmat5017.
- [11] R. Mankowsky, M. Först, and A. Cavalleri. “Non-equilibrium control of complex solids by nonlinear phononics”. *Reports on Progress in Physics* **79**, 064503 (2016).
DOI: 10.1088/0034-4885/79/6/064503.
- [12] J. Luo, T. Lin, J. Zhang, X. Chen, E. R. Blackert, R. Xu, B. I. Yakobson, and H. Zhu. “Large effective magnetic fields from chiral phonons in rare-earth halides”. *Science* **382**, 698–702 (2023).
DOI: 10.1126/science.adi9601.
- [13] M. Basini, M. Pancaldi, B. Wehinger, M. Udina, V. Unikandanunni, T. Tadano, M. C. Hoffmann, A. V. Balatsky, and S. Bonetti. “Terahertz electric-field-driven dynamical multiferroicity in SrTiO₃”. *Nature* **628**, 534–539 (2024).
DOI: 10.1038/s41586-024-07175-9.
- [14] J. W. McIver, B. Schulte, F.-U. Stein, T. Matsuyama, G. Jotzu, G. Meier, and A. Cavalleri. “Light-induced anomalous Hall effect in graphene”. *Nature Physics* **16**, 38–41 (2020).
DOI: 10.1038/s41567-019-0698-y.
- [15] J. H. Shirley. “Solution of the Schrödinger Equation with a Hamiltonian Periodic in Time”. *Phys. Rev.* **138**, B979–B987 (1965).
DOI: 10.1103/PhysRev.138.B979.
- [16] N. H. Lindner, G. Refael, and V. Galitski. “Floquet topological insulator in semiconductor quantum wells”. *Nature Physics* **7**, 490–495 (2011).
DOI: 10.1038/nphys1926.
- [17] Y. H. Wang, H. Steinberg, P. Jarillo-Herrero, and N. Gedik. “Observation of Floquet-Bloch States on the Surface of a Topological Insulator”. *Science* **342**, 453–457 (2013).
DOI: 10.1126/science.1239834.
- [18] M. Bukov, L. D’Alessio, and A. Polkovnikov. “Universal high-frequency behavior of periodically driven systems: from dynamical stabilization to Floquet engineering”. *Advances in Physics* **64**, 139–226 (2015).
DOI: 10.1080/00018732.2015.1055918.
- [19] T. Oka and S. Kitamura. “Floquet Engineering of Quantum Materials”. *Annual Review of Condensed Matter Physics* **10**, 387–408 (2019).
DOI: 10.1146/annurev-conmatphys-031218-013423.

-
- [20] S. A. Sato, J. W. McIver, M. Nuske, P. Tang, G. Jotzu, B. Schulte, H. Hübener, U. De Giovannini, L. Mathey, M. A. Sentef, A. Cavalleri, and A. Rubio. “Microscopic theory for the light-induced anomalous Hall effect in graphene”. *Phys. Rev. B* **99**, 214302 (2019).
DOI: 10.1103/PhysRevB.99.214302.
- [21] S. Ito, M. Schüler, M. Meierhofer, S. Schlauderer, J. Freudenstein, J. Reimann, D. Afanasiev, K. A. Kokh, O. E. Tereshchenko, J. Güdde, M. A. Sentef, U. Höfer, and R. Huber. “Build-up and dephasing of Floquet–Bloch bands on subcycle timescales”. *Nature* **616**, 696–701 (2023).
DOI: 10.1038/s41586-023-05850-x.
- [22] T. F. Nova, A. S. Disa, M. Fechner, and A. Cavalleri. “Metastable ferroelectricity in optically strained SrTiO₃”. *Science* **364**, 1075–1079 (2019).
DOI: 10.1126/science.aaw4911.
- [23] M. Först, C. Manzoni, S. Kaiser, Y. Tomioka, Y. Tokura, R. Merlin, and A. Cavalleri. “Nonlinear phononics as an ultrafast route to lattice control”. *Nature Physics* **7**, 854–856 (2011).
DOI: 10.1038/nphys2055.
- [24] A. S. Disa, T. F. Nova, and A. Cavalleri. “Engineering crystal structures with light”. *Nature Physics* **17**, 1087–1092 (2021).
DOI: 10.1038/s41567-021-01366-1.
- [25] A. Kogar et al. “Light-induced charge density wave in LaTe₃”. *Nature Physics* **16**, 159–163 (2020).
DOI: 10.1038/s41567-019-0705-3.
- [26] I. Radu, K. Vahaplar, C. Stamm, T. Kachel, N. Pontius, H. A. Dürr, T. A. Ostler, J. Barker, R. F. L. Evans, R. W. Chantrell, A. Tsukamoto, A. Itoh, A. Kirilyuk, T. Rasing, and A. V. Kimel. “Transient ferromagnetic-like state mediating ultrafast reversal of antiferromagnetically coupled spins”. *Nature* **472**, 205–208 (2011).
DOI: 10.1038/nature09901.
- [27] A. S. Disa, M. Fechner, T. F. Nova, B. Liu, M. Först, D. Prabhakaran, P. G. Radaelli, and A. Cavalleri. “Polarizing an antiferromagnet by optical engineering of the crystal field”. *Nature Physics* **16**, 937–941 (2020).
DOI: 10.1038/s41567-020-0936-3.
- [28] X. Wang, C. Xiao, H. Park, J. Zhu, C. Wang, T. Taniguchi, K. Watanabe, J. Yan, D. Xiao, D. R. Gamelin, W. Yao, and X. Xu. “Light-induced ferromagnetism in moiré superlattices”. *Nature* **604**, 468–473 (2022).
DOI: 10.1038/s41586-022-04472-z.

- [29] A. S. Disa, J. Curtis, M. Fechner, A. Liu, A. von Hoegen, M. Först, T. F. Nova, P. Narang, A. Maljuk, A. V. Boris, B. Keimer, and A. Cavalleri. “Photo-induced high-temperature ferromagnetism in YTiO_3 ”. *Nature* **617**, 73–78 (2023).
DOI: 10.1038/s41586-023-05853-8.
- [30] D. Fausti, R. I. Tobey, N. Dean, S. Kaiser, A. Dienst, M. C. Hoffmann, S. Pyon, T. Takayama, H. Takagi, and A. Cavalleri. “Light-Induced Superconductivity in a Stripe-Ordered Cuprate”. *Science* **331**, 189–191 (2011).
DOI: 10.1126/science.1197294.
- [31] W. Hu, S. Kaiser, D. Nicoletti, C. R. Hunt, I. Gierz, M. C. Hoffmann, M. Le Tacon, T. Loew, B. Keimer, and A. Cavalleri. “Optically enhanced coherent transport in $\text{YBa}_2\text{Cu}_3\text{O}_{6.5}$ by ultrafast redistribution of interlayer coupling”. *Nature Materials* **13**, 705–711 (2014).
DOI: 10.1038/nmat3963.
- [32] M. Mitrano, A. Cantaluppi, D. Nicoletti, S. Kaiser, A. Perucchi, S. Lupi, P. Di Pietro, D. Pontiroli, M. Riccò, S. R. Clark, D. Jaksch, and A. Cavalleri. “Possible light-induced superconductivity in K_3C_{60} at high temperature”. *Nature* **530**, 461–464 (2016).
DOI: 10.1038/nature16522.
- [33] M. Budden, T. Gebert, M. Buzzi, G. Jotzu, E. Wang, T. Matsuyama, G. Meier, Y. Laplace, D. Pontiroli, M. Riccò, F. Schlawin, D. Jaksch, and A. Cavalleri. “Evidence for metastable photo-induced superconductivity in K_3C_{60} ”. *Nature Physics* **17**, 611–618 (2021).
DOI: 10.1038/s41567-020-01148-1.
- [34] A. de la Torre, D. M. Kennes, M. Claassen, S. Gerber, J. W. McIver, and M. A. Sentef. “Colloquium: Nonthermal pathways to ultrafast control in quantum materials”. *Rev. Mod. Phys.* **93**, 041002 (2021).
DOI: 10.1103/RevModPhys.93.041002.
- [35] F. Di Paolo. *Networks and Devices Using Planar Transmissions Lines*. CRC Press, 2000.
DOI: 10.1201/9781315220369.
- [36] K. Yoshioka, N. Kumada, K. Muraki, and M. Hashisaka. “On-chip coherent frequency-domain THz spectroscopy for electrical transport”. *Applied Physics Letters* **117** (2020).
DOI: 10.1063/5.0024089.

-
- [37] A. M. Potts, A. K. Nayak, M. Nagel, K. Kaj, B. Stamenic, D. D. John, R. D. Averitt, and A. F. Young. “On-Chip Time-Domain Terahertz Spectroscopy of Superconducting Films below the Diffraction Limit”. *Nano Letters* **23**, 3835–3841 (2023).
DOI: 10.1021/acs.nanolett.3c00412.
- [38] W. Zhao, S. Wang, S. Chen, Z. Zhang, K. Watanabe, T. Taniguchi, A. Zettl, and F. Wang. “Observation of hydrodynamic plasmons and energy waves in graphene”. *Nature* **614**, 688–693 (2023).
DOI: 10.1038/s41586-022-05619-8.
- [39] G. Kipp et al. *Cavity electrodynamics of van der Waals heterostructures*. 2024.
DOI: 10.48550/arxiv.2403.19745.
- [40] H. K. Onnes. “Further experiments with liquid helium. C. On the change of electric resistance of pure metals at very low temperatures etc. IV. The resistance of pure mercury at helium temperatures.” *Leiden Comm.* **120b**, **122b**, **124c** (1911).
- [41] T. Van Duzer and C. W. Turner. *Principles of superconductive devices and circuits*. 2nd edition. Philadelphia, PA: Prentice Hall, 1998.
- [42] W. Hassenzahl, D. Hazelton, B. Johnson, P. Komarek, M. Noe, and C. Reis. “Electric power applications of superconductivity”. *Proceedings of the IEEE* **92**, 1655–1674 (2004).
DOI: 10.1109/jproc.2004.833674.
- [43] M. Tinkham. *Introduction to Superconductivity*. 2nd edition. Dover Publications, 2004.
- [44] W. Meissner and R. Ochsenfeld. “Ein neuer Effekt bei Eintritt der Supraleitfähigkeit”. *Die Naturwissenschaften* **21**, 787–788 (1933).
DOI: 10.1007/bf01504252.
- [45] J. N. Rjabinin and L. W. Shubnikow. “Magnetic Properties and Critical Currents of Supra-conducting Alloys”. *Nature* **135**, 581–582 (1935).
DOI: 10.1038/135581a0.
- [46] A. A. Abrikosov. “On the Magnetic Properties of Superconductors of the Second Group”. *Sov. Phys. JETP* **5**, 1174–1182 (1957).
- [47] H. W. Kroto, J. R. Heath, S. C. O’Brien, R. F. Curl, and R. E. Smalley. “C₆₀: Buckminsterfullerene”. *Nature* **318**, 162–163 (1985).
DOI: 10.1038/318162a0.

- [48] R. S. Ruoff and A. L. Ruoff. “The bulk modulus of C_{60} molecules and crystals: a molecular mechanics approach”. *Applied physics letters* **59**, 1553–1555 (1991).
- [49] R. S. Ruoff and A. L. Ruoff. “Is C_{60} stiffer than diamond?” *Nature* **350**, 663–664 (1991).
DOI: 10.1038/350663b0.
- [50] S. Woo, S. H. Lee, E. Kim, K. Lee, Y. H. Lee, S. Y. Hwang, and I. C. Jeon. “Bulk modulus of the C_{60} molecule via the tight binding method”. *Physics Letters A* **162**, 501–505 (1992).
- [51] A. Hirsch. “The chemistry of the fullerenes: an overview”. *Angewandte Chemie International Edition in English* **32**, 1138–1141 (1993).
- [52] P. W. Stephens, L. Mihaly, P. L. Lee, R. L. Whetten, S.-M. Huang, R. Kaner, F. Deiderich, and K. Holczer. “Structure of single-phase superconducting K_3C_{60} ”. *Nature* **351**, 632–634 (1991).
DOI: 10.1038/351632a0.
- [53] K. Momma and F. Izumi. “VESTA 3 for three-dimensional visualization of crystal, volumetric and morphology data”. *Journal of Applied Crystallography* **44**, 1272–1276 (2011).
DOI: 10.1107/s0021889811038970.
- [54] M. Dresselhaus, G. Dresselhaus, and P. Eklund. *Chapter 7 - Crystalline Structure of Fullerene Solids*. Edited by M. Dresselhaus, G. Dresselhaus, and P. Eklund. San Diego: Academic Press, 1996, pages 171–223.
DOI: <https://doi.org/10.1016/B978-012221820-0/50007-1>.
- [55] P. A. Heiney, J. E. Fischer, A. R. McGhie, W. J. Romanow, A. M. Denenstein, J. P. McCauley Jr., A. B. Smith, and D. E. Cox. “Orientational ordering transition in solid C_{60} ”. *Phys. Rev. Lett.* **66**, 2911–2914 (1991).
DOI: 10.1103/PhysRevLett.66.2911.
- [56] P. A. Heiney, G. B. M. Vaughan, J. E. Fischer, N. Coustel, D. E. Cox, J. R. D. Copley, D. A. Neumann, W. A. Kamitakahara, K. M. Creegan, D. M. Cox, J. P. McCauley, and A. B. Smith. “Discontinuous volume change at the orientational-ordering transition in solid C_{60} ”. *Phys. Rev. B* **45**, 4544–4547 (1992).
DOI: 10.1103/PhysRevB.45.4544.
- [57] R. M. Fleming, A. P. Ramirez, M. J. Rosseinsky, D. W. Murphy, R. C. Haddon, S. M. Zahurak, and A. V. Makhija. “Relation of structure and superconducting transition temperatures in A_3C_{60} ”. *Nature* **352**, 787–788 (1991).
DOI: 10.1038/352787a0.

-
- [58] A. F. Hebard, M. J. Rosseinsky, R. C. Haddon, D. W. Murphy, S. H. Glarum, T. T. M. Palstra, A. P. Ramirez, and A. R. Kortan. “Superconductivity at 18 K in potassium-doped C_{60} ”. *Nature* **350**, 600–601 (1991).
DOI: 10.1038/350600a0.
- [59] Y. Ihara, H. Alloul, P. Wzietek, D. Pontiroli, M. Mazzani, and M. Riccò. “Spin dynamics at the Mott transition and in the metallic state of the Cs_3C_{60} superconducting phases”. *Europhysics Letters* **94**, 37007 (2011).
DOI: 10.1209/0295-5075/94/37007.
- [60] A. Y. Ganin, Y. Takabayashi, Y. Z. Khimyak, S. Margadonna, A. Tamai, M. J. Rosseinsky, and K. Prassides. “Bulk superconductivity at 38 K in a molecular system”. *Nature Materials* **7**, 367–371 (2008).
- [61] R. H. Zadik et al. “Optimized unconventional superconductivity in a molecular Jahn-Teller metal”. *Science Advances* **1**, e1500059 (2015).
DOI: 10.1126/sciadv.1500059.
- [62] S. C. Erwin and W. E. Pickett. “Theoretical Fermi-Surface Properties and Superconducting Parameters for K_3C_{60} ”. *Science* **254**, 842–845 (1991).
DOI: 10.1126/science.254.5033.842.
- [63] S. Saito and A. Oshiyama. “Cohesive mechanism and energy bands of solid C_{60} ”. *Physical Review Letters* **66**, 2637–2640 (1991).
DOI: 10.1103/PhysRevLett.66.2637.
- [64] R. Haddon, L. Brus, and K. Raghavachari. “Electronic structure and bonding in icosahedral C_{60} ”. *Chemical Physics Letters* **125**, 459–464 (1986).
DOI: 10.1016/0009-2614(86)87079-8.
- [65] R. C. Haddon et al. “Conducting films of C_{60} and C_{70} by alkali-metal doping”. *Nature* **350**, 320–322 (1991).
DOI: 10.1038/350320a0.
- [66] K. Kamarás, G. Klupp, P. Matus, A. Y. Ganin, A. McLennan, M. J. Rosseinsky, Y. Takabayashi, M. T. McDonald, and K. Prassides. “Mott localization in the correlated superconductor Cs_3C_{60} resulting from the molecular Jahn-Teller effect”. *Journal of Physics: Conference Series* **428**, 012002 (2013).
DOI: 10.1088/1742-6596/428/1/012002.
- [67] R. W. Lof, M. A. van Veenendaal, B. Koopmans, H. T. Jonkman, and G. A. Sawatzky. “Band gap, excitons, and Coulomb interaction in solid C_{60} ”. *Physical Review Letters* **68**, 3924–3927 (1992).
DOI: 10.1103/PhysRevLett.68.3924.

- [68] P. A. Brühwiler, A. J. Maxwell, A. Nilsson, N. Mårtensson, and O. Gunnarsson. “Auger and photoelectron study of the Hubbard U in C_{60} , K_3C_{60} , and K_6C_{60} ”. *Physical Review B* **48**, 18296–18299 (1993).
DOI: 10.1103/PhysRevB.48.18296.
- [69] O. Gunnarsson. *Alkali-Doped Fullerenes: Narrow-Band Solids with Unusual Properties*. World Scientific, 2004.
DOI: 10.1142/5404.
- [70] Y. J. Uemura, A. Keren, L. P. Le, G. M. Luke, B. J. Sternlieb, W. D. Wu, J. H. Brewer, R. L. Whetten, S. M. Huang, S. Lin, R. B. Kaner, F. Diederich, S. Donovan, G. Grüner, and K. Holczer. “Magnetic-field penetration depth in K_3C_{60} measured by muon spin relaxation”. *Nature* **352**, 605–607 (1991).
DOI: 10.1038/352605a0.
- [71] R.-S. Wang, D. Peng, L.-N. Zong, Z.-W. Zhu, and X.-J. Chen. “Full set of superconducting parameters of K_3C_{60} ”. *Carbon* **202**, 325–335 (2023).
DOI: 10.1016/j.carbon.2022.10.076.
- [72] K. Holczer, O. Klein, G. Grüner, J. D. Thompson, F. Diederich, and R. L. Whetten. “Critical magnetic fields in the superconducting state of K_3C_{60} ”. *Phys. Rev. Lett.* **67**, 271–274 (1991).
DOI: 10.1103/PhysRevLett.67.271.
- [73] C. E. Johnson, H. W. Jiang, K. Holczer, R. B. Kaner, R. L. Whetten, and F. Diederich. “Upper-critical-field–temperature phase diagram of alkali-metal-intercalated C_{60} superconductors”. *Phys. Rev. B* **46**, 5880–5882 (1992).
DOI: 10.1103/PhysRevB.46.5880.
- [74] G. S. Boebinger, T. T. M. Palstra, A. Passner, M. J. Rosseinsky, D. W. Murphy, and I. I. Mazin. “Evidence of upper-critical-field enhancement in K_3C_{60} powders”. *Phys. Rev. B* **46**, 5876–5879 (1992).
DOI: 10.1103/PhysRevB.46.5876.
- [75] K. Holczer and R. L. Whetten. “Superconducting and normal state properties of the A_3C_{60} compounds”. *Carbon* **30**, 1261–1276 (1992).
DOI: 10.1016/0008-6223(92)90067-7.
- [76] O. Gunnarsson. “Superconductivity in fullerenes”. *Rev. Mod. Phys.* **69**, 575–606 (1997).
DOI: 10.1103/RevModPhys.69.575.
- [77] M. Lee, M. Tai, S. Luo, and J. Shi. “Critical current densities in K_3C_{60}/Rb_3C_{60} powders determined from AC/DC susceptibility measurements”. *Physica C: Superconductivity* **245**, 6–11 (1995).
DOI: 10.1016/0921-4534(95)00100-x.

-
- [78] Y. Nomura, S. Sakai, M. Capone, and R. Arita. “Exotic s-wave superconductivity in alkali-doped fullerenes”. *Journal of Physics: Condensed Matter* **28**, 153001 (2016).
DOI: 10.1088/0953-8984/28/15/153001.
- [79] C. M. Varma, J. Zaanen, and K. Raghavachari. “Superconductivity in the Fullerenes”. *Science* **254**, 989–992 (1991).
DOI: 10.1126/science.254.5034.989.
- [80] I. I. Mazin, S. N. Rashkeev, V. P. Antropov, O. Jepsen, A. I. Liechtenstein, and O. K. Andersen. “Quantitative theory of superconductivity in doped C_{60} ”. *Phys. Rev. B* **45**, 5114–5117 (1992).
DOI: 10.1103/PhysRevB.45.5114.
- [81] M. Schluter, M. Lannoo, M. Needels, G. A. Baraff, and D. Tománek. “Electron-phonon coupling and superconductivity in alkali-intercalated C_{60} solid”. *Phys. Rev. Lett.* **68**, 526–529 (1992).
DOI: 10.1103/PhysRevLett.68.526.
- [82] M. Schlüter, M. Lannoo, M. Needels, G. Baraff, and D. Tománek. “Superconductivity in alkali intercalated C_{60} ”. *Journal of Physics and Chemistry of Solids* **53**, 1473–1485 (1992).
DOI: 10.1016/0022-3697(92)90240-e.
- [83] G. Baskaran. “A Theory of the Normal and Superconducting States of Doped Solid C_{60} ”. *International Journal of Modern Physics B* **06**, 469–472 (1992).
DOI: 10.1142/s0217979292000268.
- [84] S. Chakravarty, M. P. Gelfand, and S. Kivelson. “Electronic Correlation Effects and Superconductivity in Doped Fullerenes”. *Science* **254**, 970–974 (1991).
DOI: 10.1126/science.254.5034.970.
- [85] R. Friedberg, T. D. Lee, and H. C. Ren. “Parity doublets and the pairing mechanism in C_{60} ”. *Phys. Rev. B* **46**, 14150–14173 (1992).
DOI: 10.1103/PhysRevB.46.14150.
- [86] J. Bardeen, L. N. Cooper, and J. R. Schrieffer. “Theory of Superconductivity”. *Phys. Rev.* **108**, 1175–1204 (1957).
DOI: 10.1103/PhysRev.108.1175.
- [87] C. C. Chen and C. M. Lieber. “Synthesis of pure $^{13}C_{60}$ and determination of the isotope effect for fullerene superconductors”. *Journal of the American Chemical Society* **114**, 3141–3142 (1992).
DOI: 10.1021/ja00034a072.

- [88] T. Ebbesen, J. Tsai, K. Tanigaki, H. Hiura, Y. Shimakawa, Y. Kubo, I. Hiro-sawa, and J. Mizuki. “Dopant isotope effect on superconductivity in Rb_3C_{60} ”. *Physica C: Superconductivity* **203**, 163–166 (1992).
DOI: 10.1016/0921-4534(92)90523-f.
- [89] B. Burk, V. H. Crespi, A. Zettl, and M. L. Cohen. “Rubidium isotope effect in superconducting Rb_3C_{60} ”. *Phys. Rev. Lett.* **72**, 3706–3709 (1994).
DOI: 10.1103/PhysRevLett.72.3706.
- [90] B. Burk, V. H. Crespi, M. Fuhrer, A. Zettl, and M. L. Cohen. “Alkali-metal isotope effect in Rb_3C_{60} ”. *Physica C: Superconductivity* **235–240**, 2493–2494 (1994).
DOI: 10.1016/0921-4534(94)92467-8.
- [91] J. Hou, L. Lu, V. H. Crespi, X.-D. Xiang, A. Zettl, and M. L. Cohen. “Resistivity saturation in alkali-doped C_{60} ”. *Solid State Communications* **93**, 973–977 (1995).
DOI: 10.1016/0038-1098(94)00915-5.
- [92] N. E. Hussey, K. Takenaka, and H. Takagi. “Universality of the Mott–Ioffe–Regel limit in metals”. *Philosophical Magazine* **84**, 2847–2864 (2004).
DOI: 10.1080/14786430410001716944.
- [93] M. Capone, M. Fabrizio, and E. Tosatti. “Direct Transition between a Singlet Mott Insulator and a Superconductor”. *Phys. Rev. Lett.* **86**, 5361–5364 (2001).
DOI: 10.1103/PhysRevLett.86.5361.
- [94] M. Capone, M. Fabrizio, C. Castellani, and E. Tosatti. “Strongly Correlated Superconductivity”. *Science* **296**, 2364–2366 (2002).
DOI: 10.1126/science.1071122.
- [95] M. Capone, M. Fabrizio, C. Castellani, and E. Tosatti. “Strongly Correlated Superconductivity and Pseudogap Phase near a Multiband Mott Insulator”. *Physical Review Letters* **93** (2004).
DOI: 10.1103/PhysRevLett.93.047001.
- [96] Y. Nomura, K. Nakamura, and R. Arita. “Ab initio derivation of electronic low-energy models for C_{60} and aromatic compounds”. *Physical Review B* **85** (2012).
DOI: 10.1103/PhysRevB.85.155452.
- [97] Y. Nomura, S. Sakai, M. Capone, and R. Arita. “Unified understanding of superconductivity and Mott transition in alkali-doped fullerenes from first principles”. *Science Advances* **1** (2015).
DOI: 10.1126/sciadv.1500568.

-
- [98] Y. Nomura and R. Arita. “Ab initio downfolding for electron-phonon-coupled systems: Constrained density-functional perturbation theory”. *Physical Review B* **92** (2015).
DOI: 10.1103/PhysRevB.92.245108.
- [99] L. R. Testardi. “Destruction of Superconductivity by Laser Light”. *Phys. Rev. B* **4**, 2189–2196 (1971).
DOI: 10.1103/PhysRevB.4.2189.
- [100] G. N. Gol’tsman, O. Okunev, G. Chulkova, A. Lipatov, A. Semenov, K. Smirnov, B. Voronov, A. Dzardanov, C. Williams, and R. Sobolewski. “Picosecond superconducting single-photon optical detector”. *Applied Physics Letters* **79**, 705–707 (2001).
DOI: 10.1063/1.1388868.
- [101] C. M. Natarajan, M. G. Tanner, and R. H. Hadfield. “Superconducting nanowire single-photon detectors: physics and applications”. *Superconductor Science and Technology* **25**, 063001 (2012).
DOI: 10.1088/0953-2048/25/6/063001.
- [102] A. F. G. Wyatt, V. M. Dmitriev, W. S. Moore, and F. W. Sheard. “Microwave-Enhanced Critical Supercurrents in Constricted Tin Films”. *Physical Review Letters* **16**, 1166–1169 (1966).
DOI: 10.1103/PhysRevLett.16.1166.
- [103] A. H. Dayem and J. J. Wiegand. “Behavior of Thin-Film Superconducting Bridges in a Microwave Field”. *Physical Review* **155**, 419–428 (1967).
DOI: 10.1103/physrev.155.419.
- [104] J. Fink, E. Schierle, E. Weschke, J. Geck, D. Hawthorn, V. Soltwisch, H. Wadati, H.-H. Wu, H. A. Dürr, N. Wizent, B. Büchner, and G. A. Sawatzky. “Charge ordering in $\text{La}_{1.8-x}\text{Eu}_{0.2}\text{Sr}_x\text{CuO}_4$ studied by resonant soft x-ray diffraction”. *Physical Review B* **79** (2009).
DOI: 10.1103/PhysRevB.79.100502.
- [105] S. Kaiser, C. R. Hunt, D. Nicoletti, W. Hu, I. Gierz, H. Y. Liu, M. Le Tacon, T. Loew, D. Haug, B. Keimer, and A. Cavalleri. “Optically induced coherent transport far above T_c in underdoped $\text{YBa}_2\text{Cu}_3\text{O}_{6+\delta}$ ”. *Phys. Rev. B* **89**, 184516 (2014).
DOI: 10.1103/PhysRevB.89.184516.
- [106] D. Nicoletti, E. Casandruc, Y. Laplace, V. Khanna, C. R. Hunt, S. Kaiser, S. S. Dhesi, G. D. Gu, J. P. Hill, and A. Cavalleri. “Optically induced superconductivity in striped $\text{La}_{2-x}\text{Ba}_x\text{CuO}_4$ by polarization-selective excitation in

- the near infrared”. *Phys. Rev. B* **90**, 100503 (2014).
DOI: 10.1103/PhysRevB.90.100503.
- [107] R. Mankowsky et al. “Nonlinear lattice dynamics as a basis for enhanced superconductivity in $\text{YBa}_2\text{Cu}_3\text{O}_{6.5}$ ”. *Nature* **516**, 71–73 (2014).
DOI: 10.1038/nature13875.
- [108] M. Buzzi et al. “Photomolecular High-Temperature Superconductivity”. *Phys. Rev. X* **10**, 031028 (2020).
DOI: 10.1103/PhysRevX.10.031028.
- [109] M. Buzzi, D. Nicoletti, S. Fava, G. Jotzu, K. Miyagawa, K. Kanoda, A. Henderson, T. Siegrist, J. A. Schlueter, M.-S. Nam, A. Ardavan, and A. Cavalleri. “Phase Diagram for Light-Induced Superconductivity in $\kappa\text{-(ET)}_2\text{-X}$ ”. *Phys. Rev. Lett.* **127**, 197002 (2021).
DOI: 10.1103/PhysRevLett.127.197002.
- [110] A. Cantaluppi, M. Buzzi, G. Jotzu, D. Nicoletti, M. Mitrano, D. Pontiroli, M. Riccò, A. Perucchi, P. Di Pietro, and A. Cavalleri. “Pressure tuning of light-induced superconductivity in K_3C_{60} ”. *Nature Physics* **14**, 837–841 (2018).
DOI: 10.1038/s41567-018-0134-8.
- [111] E. Rowe, B. Yuan, M. Buzzi, G. Jotzu, Y. Zhu, M. Fechner, M. Först, B. Liu, D. Pontiroli, M. Riccò, and A. Cavalleri. “Resonant enhancement of photo-induced superconductivity in K_3C_{60} ”. *Nature Physics* **19**, 1821–1826 (2023).
DOI: 10.1038/s41567-023-02235-9.
- [112] M. Dressel and G. Grüner. *Electrodynamics of Solids: Optical Properties of Electrons in Matter*. Cambridge University Press, 2002.
- [113] M. Fox. *Optical properties of solids*. English. Second edition. Oxford: Oxford University Press, 2010.
- [114] M. P. Gelfand and J. P. Lu. “Orientational correlations and order in A_3C_{60} ”. *Applied Physics A* **56**, 215–217 (1993).
DOI: 10.1007/BF00539477.
- [115] M. S. Deshpande, E. J. Mele, M. J. Rice, and H.-Y. Choi. “Midinfrared conductivity in orientationally disordered doped fullerides”. *Phys. Rev. B* **50**, 6993–7006 (1994).
DOI: 10.1103/PhysRevB.50.6993.
- [116] J. van den Brink, O. Gunnarsson, and V. Eyert. “Optical conductivity in A_3C_{60} ($A = \text{K, Rb}$)”. *Phys. Rev. B* **57**, 2163–2167 (1998).
DOI: 10.1103/PhysRevB.57.2163.

-
- [117] A. Nava, C. Giannetti, A. Georges, E. Tosatti, and M. Fabrizio. “Cooling quasiparticles in A_3C_{60} fullerenes by excitonic mid-infrared absorption”. *Nature Physics* **14**, 154–159 (2018).
DOI: 10.1038/nphys4288.
- [118] L. Degiorgi, G. Briceno, M. S. Fuhrer, A. Zettl, and P. Wachter. “Optical measurements of the superconducting gap in single-crystal K_3C_{60} and Rb_3C_{60} ”. *Nature* **369**, 541–543 (1994).
DOI: 10.1038/369541a0.
- [119] L. Degiorgi, E. J. Nicol, O. Klein, G. Grüner, P. Wachter, S.-M. Huang, J. Wiley, and R. B. Kaner. “Optical properties of the alkali-metal-doped superconducting fullerenes: K_3C_{60} and Rb_3C_{60} ”. *Phys. Rev. B* **49**, 7012–7025 (1994).
DOI: 10.1103/PhysRevB.49.7012.
- [120] J. D. Jackson. *Classical electrodynamics*. 3rd ed. New York, NY: Wiley, 1999.
- [121] H. Cheng, J. Whitaker, T. Weller, and L. Katehi. “Terahertz-bandwidth characterization of coplanar waveguide via time-domain electro-optic sampling”. *1994 IEEE MTT-S International Microwave Symposium Digest (Cat. No.94 CH3389-4)*. 1994, 477–480 vol.1.
DOI: 10.1109/MWSYM.1994.335437.
- [122] R. W. McGowan, D. Grischkowsky, and J. A. Misewich. “Demonstrated low radiative loss of a quadrupole ultrashort electrical pulse propagated on a three strip coplanar transmission line”. *Applied Physics Letters* **71**, 2842–2844 (1997).
DOI: 10.1063/1.120150.
- [123] I. Wolff. *Coplanar Microwave Integrated Circuits*. John Wiley & Sons, Ltd, 2006.
DOI: <https://doi.org/10.1002/0470040882>.
- [124] C. Wen. “Coplanar Waveguide: A Surface Strip Transmission Line Suitable for Nonreciprocal Gyromagnetic Device Applications”. *IEEE Transactions on Microwave Theory and Techniques* **17**, 1087–1090 (1969).
DOI: 10.1109/TMTT.1969.1127105.
- [125] F. W. Smith, H. Q. Le, M. Frankel, V. Diadiuk, M. A. Hollis, D. R. Dykaar, G. A. Mourou, and A. R. Calawa. “Picosecond GaAs-Based Photoconductive Optoelectronic Detectors”. Optica Publishing Group, 1989, OSDA176.
DOI: 10.1364/PEO.1989.OSDA176.

- [126] G. Loubriel, F. Zutavern, A. Baca, H. Hjalmarson, T. Plut, W. Helgeson, M. O'Malley, M. Ruebush, and D. Brown. "Photoconductive semiconductor switches". *IEEE Transactions on Plasma Science* **25**, 124–130 (1997).
DOI: 10.1109/27.602482.
- [127] K. G. McKay. "Avalanche Breakdown in Silicon". *Phys. Rev.* **94**, 877–884 (1954).
DOI: 10.1103/PhysRev.94.877.
- [128] H Fröhlich and B. V. Paranjape. "Dielectric Breakdown in Solids". *Proceedings of the Physical Society. Section B* **69**, 21 (1956).
DOI: 10.1088/0370-1301/69/1/304.
- [129] P. P. Pronko, P. A. VanRompay, C. Horvath, F. Loesel, T. Juhasz, X. Liu, and G. Mourou. "Avalanche ionization and dielectric breakdown in silicon with ultrafast laser pulses". *Phys. Rev. B* **58**, 2387–2390 (1998).
DOI: 10.1103/PhysRevB.58.2387.
- [130] S. Gupta, M. Y. Frankel, J. A. Valdmanis, J. F. Whitaker, G. A. Mourou, F. W. Smith, and A. R. Calawa. "Subpicosecond carrier lifetime in GaAs grown by molecular beam epitaxy at low temperatures". *Applied Physics Letters* **59**, 3276–3278 (1991).
DOI: 10.1063/1.105729.
- [131] F. Ganikhanov, G. Lin, W. Chen, C. Chang, and C. Pan. "Subpicosecond carrier lifetimes in arsenic-ion-implanted GaAs". *Applied Physics Letters* **67**, 3465–3467 (1995).
DOI: 10.1063/1.115248.
- [132] R. N. Simons. *Coplanar Waveguide Circuits, Components, and Systems*. Wiley, 2001.
DOI: 10.1002/0471224758.
- [133] C. Mack. *Fundamental Principles of Optical Lithography: The Science of Microfabrication*. Wiley, 2007.
DOI: 10.1002/9780470723876.
- [134] D. Schmicker, S. Schmidt, J. G. Skofronick, J. P. Toennies, and R. Vollmer. "Epitaxial growth of single-crystal C₆₀ on mica by helium-atom scattering". *Phys. Rev. B* **44**, 10995–10997 (1991).
DOI: 10.1103/PhysRevB.44.10995.
- [135] G. P. Kochanski, A. F. Hebard, R. C. Haddon, and A. T. Fiory. "Electrical Resistivity and Stoichiometry of K_xC₆₀ Films". *Science* **255**, 184–186 (1992).
DOI: 10.1126/science.255.5041.184.

-
- [136] O. Klein, G. Grüner, S.-M. Huang, J. B. Wiley, and R. B. Kaner. “Electrical resistivity of K_3C_{60} ”. *Phys. Rev. B* **46**, 11247–11249 (1992).
DOI: 10.1103/PhysRevB.46.11247.
- [137] X. D. Xiang, J. G. Hou, G. Briceño, W. A. Vareka, R. Mostovoy, A. Zettl, V. H. Crespi, and M. L. Cohen. “Synthesis and Electronic Transport of Single Crystal K_3C_{60} ”. *Science* **256**, 1190–1191 (1992).
DOI: 10.1126/science.256.5060.1190.
- [138] T. T. M. Palstra, R. C. Haddon, A. F. Hebard, and J. Zaanen. “Electronic transport properties of K_3C_{60} films”. *Phys. Rev. Lett.* **68**, 1054–1057 (1992).
DOI: 10.1103/PhysRevLett.68.1054.
- [139] T. T. M. Palstra, A. F. Hebard, R. C. Haddon, and P. B. Littlewood. “Fermi-liquid behavior in the electrical resistivity of K_3C_{60} and Rb_3C_{60} ”. *Physical Review B* **50**, 3462–3465 (1994).
DOI: 10.1103/PhysRevB.50.3462.
- [140] H. R. Phillip and E. A. Taft. “Kramers-Kronig Analysis of Reflectance Data for Diamond”. *Phys. Rev.* **136**, A1445–A1448 (1964).
DOI: 10.1103/PhysRev.136.A1445.
- [141] A. Frydman, O. Naaman, and R. C. Dynes. “Universal transport in two-dimensional granular superconductors”. *Phys. Rev. B* **66**, 052509 (2002).
DOI: 10.1103/PhysRevB.66.052509.
- [142] A. Gerber, T. Grenet, M. Cyrot, and J. Beille. “Double-peak superconducting transition in granular L-M-Cu-O (L=Pr,Nd,Sm,Eu,D; M=Ce,Th) superconductors”. *Phys. Rev. Lett.* **65**, 3201–3204 (1990).
DOI: 10.1103/PhysRevLett.65.3201.
- [143] E. A. Early, C. C. Almasan, R. F. Jardim, and M. B. Maple. “Double resistive superconducting transition in $Sm_{2-x}Ce_xCuO_{4-y}$ ”. *Phys. Rev. B* **47**, 433–441 (1993).
DOI: 10.1103/PhysRevB.47.433.
- [144] R. F. Jardim, L. Ben-Dor, D. Stroud, and M. B. Maple. “Granular behavior in polycrystalline $Sm_{2-x}Ce_xCuO_{4-y}$ compounds”. *Phys. Rev. B* **50**, 10080–10087 (1994).
DOI: 10.1103/PhysRevB.50.10080.
- [145] E. Wang, J. D. Adelinia, M. Chavez-Cervantes, T. Matsuyama, M. Fechner, M. Buzzi, G. Meier, and A. Cavalleri. “Superconducting nonlinear transport in optically driven high-temperature K_3C_{60} ”. *Nature Communications* **14**, 7233 (2023).
DOI: 10.1038/s41467-023-42989-7.

- [146] F. B. Silsbee. “A note on electrical conduction in metals at low temperatures”. *Journal of the Washington Academy of Sciences* **6**, 597–602 (1916).
- [147] D. Dew-Hughes. “The critical current of superconductors: an historical review”. *Low Temperature Physics* **27**, 713–722 (2001).
DOI: 10.1063/1.1401180.
- [148] T. Matsushita and M. Kiuchi. “Depairing current density in superconductors”. *Applied Physics Express* **12**, 063003 (2019).
DOI: 10.7567/1882-0786/ab1f94.
- [149] E. F. Talantsev and J. L. Tallon. “Universal self-field critical current for thin-film superconductors”. *Nature Communications* **6**, 7820 (2015).
DOI: 10.1038/ncomms8820.
- [150] A. Y. Rusanov, M. B. S. Hesselberth, and J. Aarts. “Depairing currents in superconducting films of Nb and amorphous MoGe”. *Phys. Rev. B* **70**, 024510 (2004).
DOI: 10.1103/PhysRevB.70.024510.
- [151] K. Matsumoto and P. Mele. “Artificial pinning center technology to enhance vortex pinning in YBCO coated conductors”. *Superconductor Science and Technology* **23**, 014001 (2009).
DOI: 10.1088/0953-2048/23/1/014001.
- [152] K. Xu, P. Cao, and J. R. Heath. “Achieving the Theoretical Depairing Current Limit in Superconducting Nanomesh Films”. *Nano Letters* **10**, 4206–4210 (2010). PMID: 20738113.
DOI: 10.1021/nl102584j.
- [153] S. Nawaz, R. Arpaia, F. Lombardi, and T. Bauch. “Microwave Response of Superconducting $\text{YBa}_2\text{Cu}_3\text{O}_{7-\delta}$ Nanowire Bridges Sustaining the Critical Depairing Current: Evidence of Josephson-like Behavior”. *Phys. Rev. Lett.* **110**, 167004 (2013).
DOI: 10.1103/PhysRevLett.110.167004.
- [154] S. Frasca, B. Korzh, M. Colangelo, D. Zhu, A. E. Lita, J. P. Allmaras, E. E. Wollman, V. B. Verma, A. E. Dane, E. Ramirez, A. D. Beyer, S. W. Nam, A. G. Kozorezov, M. D. Shaw, and K. K. Berggren. “Determining the depairing current in superconducting nanowire single-photon detectors”. *Phys. Rev. B* **100**, 054520 (2019).
DOI: 10.1103/PhysRevB.100.054520.
- [155] V. Ambegaokar and B. I. Halperin. “Voltage Due to Thermal Noise in the dc Josephson Effect”. *Phys. Rev. Lett.* **22**, 1364–1366 (1969).
DOI: 10.1103/PhysRevLett.22.1364.

-
- [156] C. M. Falco, W. H. Parker, S. E. Trullinger, and P. K. Hansma. “Effect of thermal noise on current-voltage characteristics of Josephson junctions”. *Phys. Rev. B* **10**, 1865–1873 (1974).
DOI: 10.1103/PhysRevB.10.1865.
- [157] B. I. Halperin and D. R. Nelson. “Resistive transition in superconducting films”. *Journal of Low Temperature Physics* **36**, 599–616 (1979).
DOI: 10.1007/bf00116988.
- [158] P. England, T. Venkatesan, X. D. Wu, and A. Inam. “Granular superconductivity in $R_1\text{Ba}_2\text{Cu}_3\text{O}_{7-\delta}$ thin films”. *Phys. Rev. B* **38**, 7125–7128 (1988).
DOI: 10.1103/PhysRevB.38.7125.
- [159] M. Baenitz, M. Heinze, E. Straube, H. Werner, R. Schlögl, V. Thommen, H.-J. Güntherodt, and K. Lüders. “Inter- and intragrain AC response of the granular superconductors K_3C_{60} and Rb_3C_{60} ”. *Physica C: Superconductivity* **228**, 181–189 (1994).
DOI: 10.1016/0921-4534(94)90191-0.
- [160] C. S. Owen and D. J. Scalapino. “Superconducting State under the Influence of External Dynamic Pair Breaking”. *Phys. Rev. Lett.* **28**, 1559–1561 (1972).
DOI: 10.1103/PhysRevLett.28.1559.
- [161] M. Mitrano. “Nonequilibrium emergent phenomena in organic molecular solids”. PhD thesis. University of Hamburg, 2015.
- [162] J. D. Adelinia, E. Wang, M. Chavez-Cervantes, T. Matsuyama, M. Fechner, M. Buzzi, G. Meier, and A. Cavalleri. “Probing optically driven K_3C_{60} thin films with an ultrafast voltmeter”. *Structural Dynamics* **12**, 024503 (2025).
DOI: 10.1063/4.0000295.
- [163] A. D. Semenov, R. S. Nebosis, Y. P. Gousev, M. A. Heusinger, and K. F. Renk. “Analysis of the nonequilibrium photoresponse of superconducting films to pulsed radiation by use of a two-temperature model”. *Phys. Rev. B* **52**, 581–590 (1995).
DOI: 10.1103/PhysRevB.52.581.
- [164] F. A. Hegmann and J. S. Preston. “Origin of the fast photoresponse of epitaxial $\text{YBa}_2\text{Cu}_3\text{O}_{7-\delta}$ thin films”. *Phys. Rev. B* **48**, 16023–16039 (1993).
DOI: 10.1103/PhysRevB.48.16023.
- [165] F. A. Hegmann, R. A. Hughes, and J. S. Preston. “Picosecond photoresponse of epitaxial $\text{YBa}_2\text{Cu}_3\text{O}_{7-\delta}$ thin films”. *Applied Physics Letters* **64**, 3172–3174 (1994).
DOI: 10.1063/1.111329.

- [166] M. Heusinger, A. Semenov, R. Nebosis, Y. Gousev, and K. Renk. “Nonthermal kinetic inductance photoresponse of thin superconducting films”. *IEEE Transactions on Applied Superconductivity* **5**, 2595–2598 (1995).
DOI: 10.1109/77.403121.
- [167] R. Sobolewski. “Ultrafast dynamics of nonequilibrium quasi-particles in high-temperature superconductors”. *Superconducting and Related Oxides: Physics and Nanoengineering III*. Edited by D. Pavuna and I. Bozovic. **3481**. Society of Photo-Optical Instrumentation Engineers (SPIE) Conference Series. 1998, pages 480–491.
DOI: 10.1117/12.335897.
- [168] A. Rothwarf and B. N. Taylor. “Measurement of Recombination Lifetimes in Superconductors”. *Phys. Rev. Lett.* **19**, 27–30 (1967).
DOI: 10.1103/PhysRevLett.19.27.
- [169] J. Demsar, R. D. Averitt, A. J. Taylor, V. V. Kabanov, W. N. Kang, H. J. Kim, E. M. Choi, and S. I. Lee. “Pair-Breaking and Superconducting State Recovery Dynamics in MgB₂”. *Phys. Rev. Lett.* **91**, 267002 (2003).
DOI: 10.1103/PhysRevLett.91.267002.
- [170] M. Beck, M. Klammer, S. Lang, P. Leiderer, V. V. Kabanov, G. N. Gol’tsman, and J. Demsar. “Energy-Gap Dynamics of Superconducting NbN Thin Films Studied by Time-Resolved Terahertz Spectroscopy”. *Phys. Rev. Lett.* **107**, 177007 (2011).
DOI: 10.1103/PhysRevLett.107.177007.
- [171] G. Jotzu, G. Meier, A. Cantaluppi, A. Cavalleri, D. Pontiroli, M. Riccò, A. Ardavan, and M.-S. Nam. “Superconducting Fluctuations Observed Far above T_c in the Isotropic Superconductor K₃C₆₀”. *Physical Review X* **13** (2023).
DOI: 10.1103/physrevx.13.021008.
- [172] P. Ai, L. Moreschini, R. Mori, D. W. Latzke, J. D. Denlinger, A. Zettl, C. Ojeda-Aristizabal, and A. Lanzara. “Linearly dispersive bands at the onset of correlations in K_xC₆₀ films”. *Phys. Rev. Res.* **5**, L022042 (2023).
DOI: 10.1103/PhysRevResearch.5.L022042.
- [173] P. W. Anderson. “Absence of Diffusion in Certain Random Lattices”. *Phys. Rev.* **109**, 1492–1505 (1958).
DOI: 10.1103/PhysRev.109.1492.

-
- [174] E. Abrahams, P. W. Anderson, D. C. Licciardello, and T. V. Ramakrishnan. “Scaling Theory of Localization: Absence of Quantum Diffusion in Two Dimensions”. *Phys. Rev. Lett.* **42**, 673–676 (1979).
DOI: 10.1103/PhysRevLett.42.673.
- [175] G. Bergmann. “Weak localization in thin films”. *Physics Reports* **107**, 1–58 (1984).
DOI: 10.1016/0370-1573(84)90103-0.
- [176] N. F. Mott. “Metal-Insulator Transition”. *Rev. Mod. Phys.* **40**, 677–683 (1968).
DOI: 10.1103/RevModPhys.40.677.
- [177] J. M. Dawlaty, S. Shivaraman, M. Chandrashekhara, F. Rana, and M. G. Spencer. “Measurement of ultrafast carrier dynamics in epitaxial graphene”. *Applied Physics Letters* **92** (2008).
DOI: 10.1063/1.2837539.
- [178] E. Rowe. “Resonant Enhancement of Light Induced Superconductivity in K_3C_{60} ”. PhD thesis. University of Hamburg, 2024.
- [179] H. E. Elsayed-Ali, T. B. Norris, M. A. Pessot, and G. A. Mourou. “Time-resolved observation of electron-phonon relaxation in copper”. *Phys. Rev. Lett.* **58**, 1212–1215 (1987).
DOI: 10.1103/PhysRevLett.58.1212.
- [180] C.-K. Sun, F. Vallée, L. Acioli, E. P. Ippen, and J. G. Fujimoto. “Femtosecond investigation of electron thermalization in gold”. *Phys. Rev. B* **48**, 12365–12368 (1993).
DOI: 10.1103/PhysRevB.48.12365.
- [181] B. Josephson. “Possible new effects in superconductive tunnelling”. *Physics Letters* **1**, 251–253 (1962).
DOI: 10.1016/0031-9163(62)91369-0.
- [182] B. D. Josephson. “The discovery of tunnelling supercurrents”. *Reviews of Modern Physics* **46**, 251–254 (1974).
DOI: 10.1103/revmodphys.46.251.
- [183] D. E. McCumber. “Effect of ac Impedance on dc Voltage-Current Characteristics of Superconductor Weak-Link Junctions”. *Journal of Applied Physics* **39**, 3113–3118 (1968).
DOI: 10.1063/1.1656743.

- [184] S. Chakravarty, G.-L. Ingold, S. Kivelson, and G. Zimanyi. “Quantum statistical mechanics of an array of resistively shunted Josephson junctions”. *Physical Review B* **37**, 3283–3294 (1988).
DOI: 10.1103/PhysRevB.37.3283.
- [185] D. S. Lemons and A. Gythiel. “Paul Langevin’s 1908 paper “On the Theory of Brownian Motion” [“Sur la théorie du mouvement brownien, ” C. R. Acad. Sci. (Paris) 146, 530–533 (1908)]”. *American Journal of Physics* **65**, 1079–1081 (1997).
DOI: 10.1119/1.18725.
- [186] R. H. M. Groeneveld, R. Sprik, and A. Lagendijk. “Femtosecond spectroscopy of electron-electron and electron-phonon energy relaxation in Ag and Au”. *Phys. Rev. B* **51**, 11433–11445 (1995).
DOI: 10.1103/PhysRevB.51.11433.
- [187] K. Allen and F. Hellman. “Specific heat of C₆₀ and K₃C₆₀ thin films for $T = 6 - 400$ K”. *Phys. Rev. B* **60**, 11765–11772 (1999).
DOI: 10.1103/PhysRevB.60.11765.
- [188] V. Kozich, A. Mognilevski, and K. Heyne. “High energy femtosecond OPA pumped by 1030nm Yb:KGW laser.” *Optics Communications* **285**, 4515–4518 (2012).
DOI: 10.1016/j.optcom.2012.06.077.

Appendix A

Optical setup

The optical part of the setup (Fig. A.1) is based on a Pharos laser, which outputs pulses of 250 fs duration and 400 μJ pulse energy, with a wavelength centred at 1030 nm, at 50 kHz repetition rate. Part of the pulse energy is converted to 515 nm wavelength via second harmonic generation. This was used to operate the photoconductive switches. The remainder serves as the input for an optical parametric amplifier (OPA) based on silver thiogallate (AGS), which outputs mid-infrared pulses centred at 7 μm wavelength (43 THz) with 1 THz bandwidth, and was based on the design by Kozich et al. [188].

In the first stage of the OPA, laser pulses of the fundamental were split into three paths, with one beam serving as a pump for the second stage, while another was focused onto a YAG crystal to generate a broad spectrum of white light with a strong component at 900 nm wavelength, and the third was passed into a BBO-crystal to generate second harmonic at 515 nm. The white light and 515 nm beams were combined at a second BBO, after which the difference frequency generation (DFG) component at 1200 nm was taken as the input for the second stage. In the second stage, the 1200 nm pulses were combined with the fundamental in an AGS crystal to amplify the 1200 nm. Finally, the amplified 1200 nm was combined with the remaining fundamental at a second AGS, after which the DFG component at 7 μm wavelength was separated out using a low-pass filter. These pulses were used to excite the K_3C_{60} thin film. The mid-infrared pulses were chopped at a frequency of ~ 1 kHz, and optical delay lines were used to scan the mutual time delay between the 515 nm pulses and the mid-infrared pulses.

The wavelength of the mid-infrared pulses was characterised using Fourier-transform infrared (FTIR) spectroscopy. The measured interference pattern and the frequency spectrum of the pulses are displayed in Fig. A.2a and A.2b. The spot size of the mid-infrared beam in the device plane wave determined using knife-edge measurements

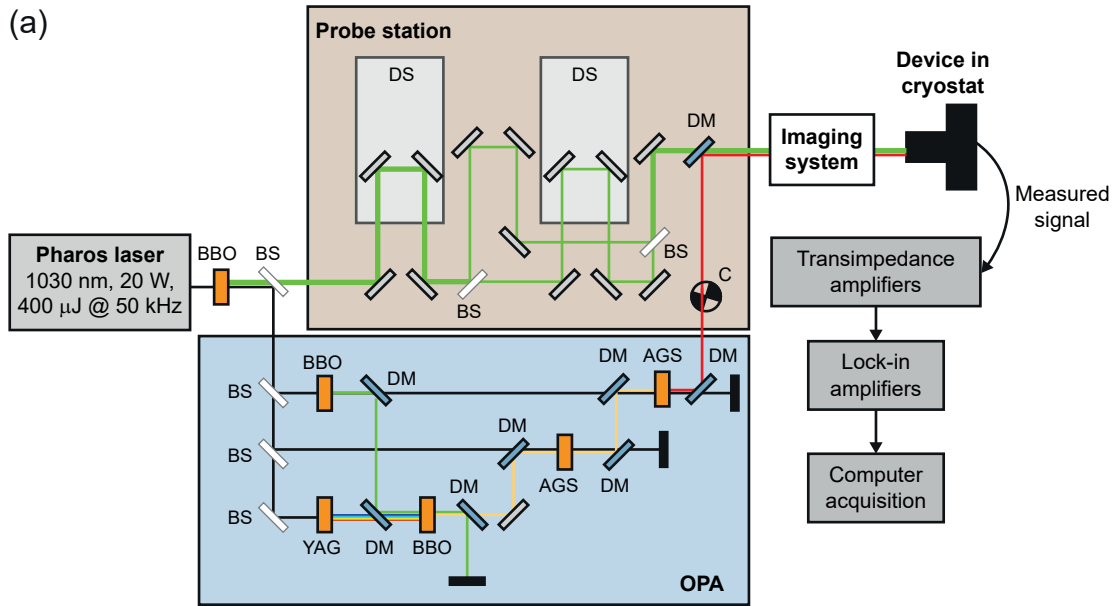


Figure A.1: **Optical setup.** Optical components are abbreviated as follows: AGS – silver thiogallate crystal, BBO – beta barium borate crystal, BS – beam splitter, C – mechanical chopper, DM – dichroic mirror, DS – delay stage, OPA – optical parametric amplifier, YAG – yttrium aluminium garnet. The wavelength of the optical pulses is represented by the colour: 1030 nm (black), 515 nm (green), 1200 nm (yellow), and 7 μ m (red).

and can be seen in Fig. A.2c and A.2d for the horizontal and vertical measurements, respectively.

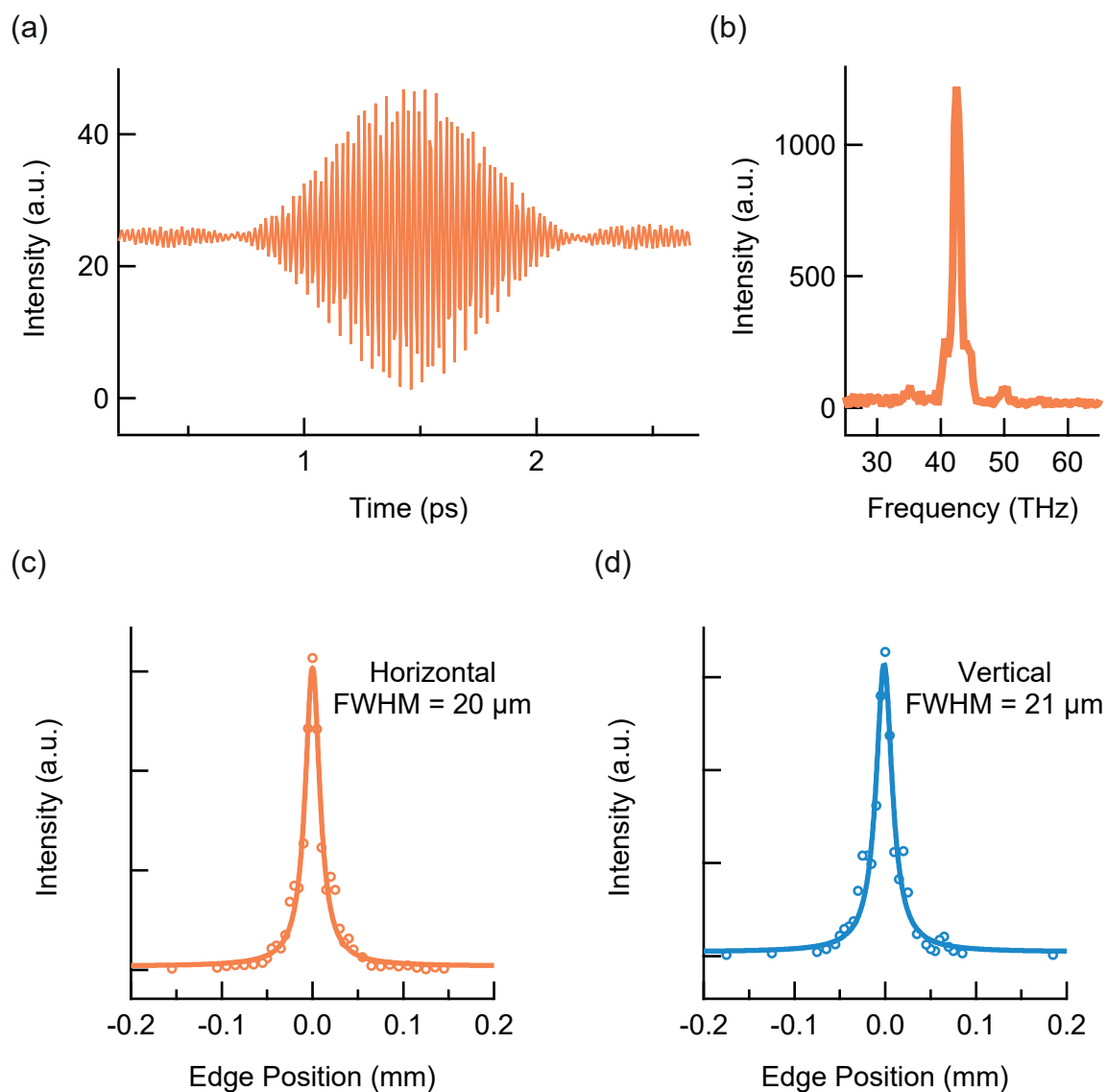
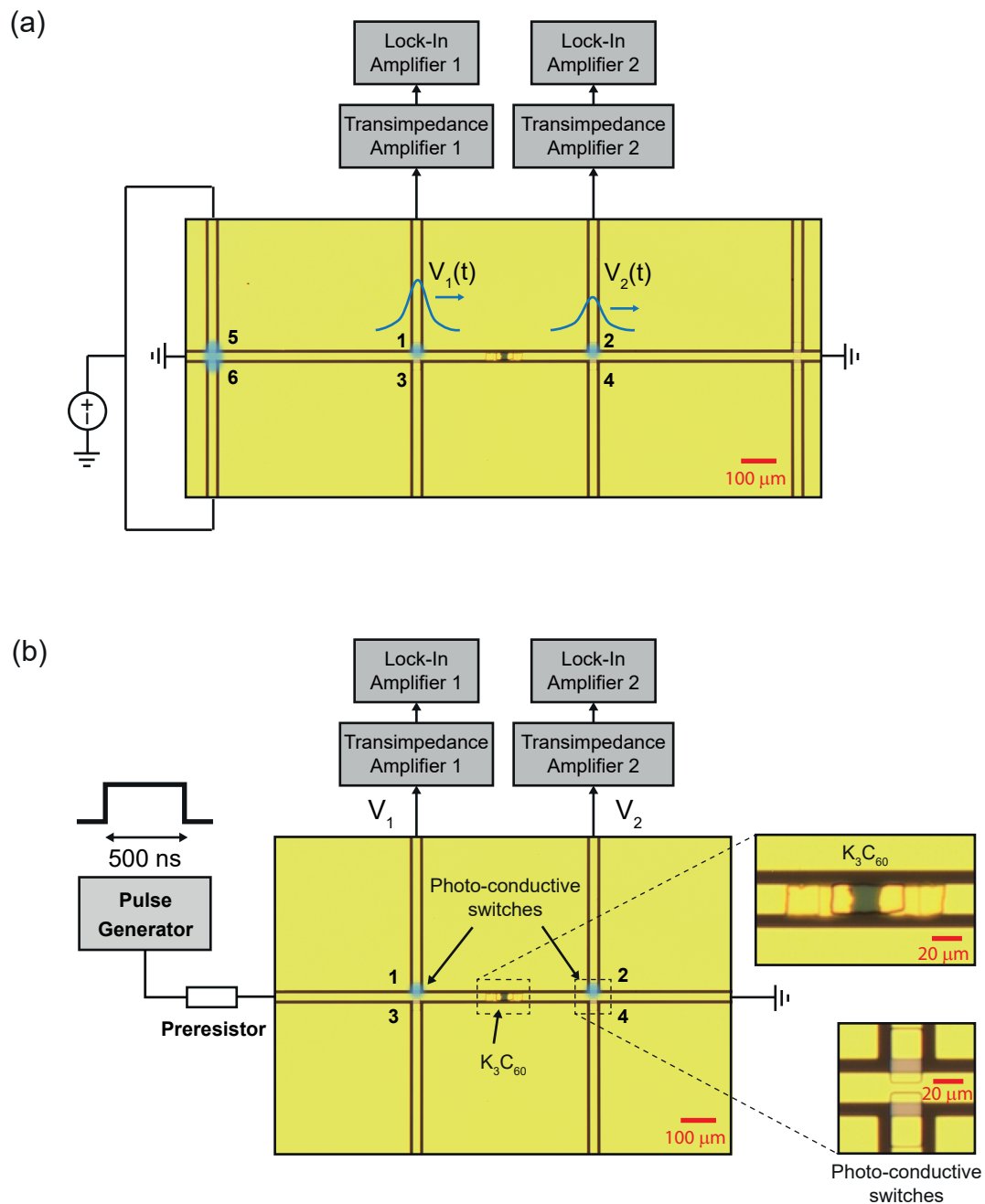


Figure A.2: **Characterisation of the mid-infrared pulses.** **a**, Interference pattern in the time domain, as measured with an FTIR interferometer. **b**, Fourier transform of the data in (a). **c** and **d**, Knife-edge measurements of the mid-infrared spot size, showing intensity versus the horizontal (c) and vertical (d) positions of the edge.

Appendix B

Electronic setup

The electronic part of the setup is displayed in Fig. B.1 for both the current pulse experiment in Chapter 5 and the ultrafast voltmeter experiment in Chapter 6. For both experiments, transient currents in each detection line were sent into in-house transimpedance amplifiers with a flat frequency dependence, an optimised -3 dB point at 3 kHz, and an amplification factor of $2 \times 10^9 \text{ V A}^{-1}$. The voltage output of the transimpedance amplifiers were then sent into lock-in amplifiers (LIAs). For the ultrafast voltmeter experiment, the LIAs were triggered at the chopping frequency of the mid-infrared pulses. For the current pulse experiment, the time-resolved transmitted pulses were measured by chopping the excitation beam for the launching switches 5 and 6. Data from the lock-in amplifier was acquired digitally using custom software written in LabVIEW.



Appendix C

Calibration of the picosecond current pulses

The picosecond currents used in Chapter 5 were calibrated by determining the total charge carried by the probe pulses. The total charge was measured using the experimental setup illustrated in Fig. C.1a. The photo-conductive switches were excited under a bias, launching pulses in both the left and right directions along the coplanar waveguide. By keeping one end of the waveguide open, the total charge contained in both pulses was able to reach the amplifiers. The voltage V_d measured at the lock-in amplifier was used to obtain the peak current following the relation

$$I_{\text{Peak}} = \frac{1}{2} \frac{2\sqrt{2}}{1.273} \frac{V_d}{A_{\text{TIA}} f_{\text{rep}}} \frac{1}{\int \text{pulse}_{\text{norm}}(t) dt}, \quad (\text{C.1})$$

where $A_{\text{TIA}} = 2 \times 10^{-9} \text{ V A}^{-1}$ is the amplification factor of the transimpedance amplifier, and $f_{\text{rep}} = 50 \text{ kHz}$ is the repetition rate of the switch trigger pulses. The factor $1/2$ arises from the fact that both the left and right travelling pulses are detected at the amplifier. The factor $2\sqrt{2}/1.273$ arises from the sinusoidal signal modulation of a square-wave input in the lock-in amplifier, where a detailed explanation can be found in the supplementary material of McIver, *et al.* [14]. The integral $\int \text{pulse}_{\text{norm}}(t) dt \approx 1.5 \text{ ps}$ is the integral of the time profile of the current pulse, with the peak of the pulse normalised to 1.

The calibrated currents are shown in Fig. C.1b and exhibited a linear dependence on the bias voltage. In Chapter 5, the data is plotted against the peak current in the transmitted pulse, given by $I_{\text{Peak}} V_{2,\text{Peak}}/V_{1,\text{Peak}}$.

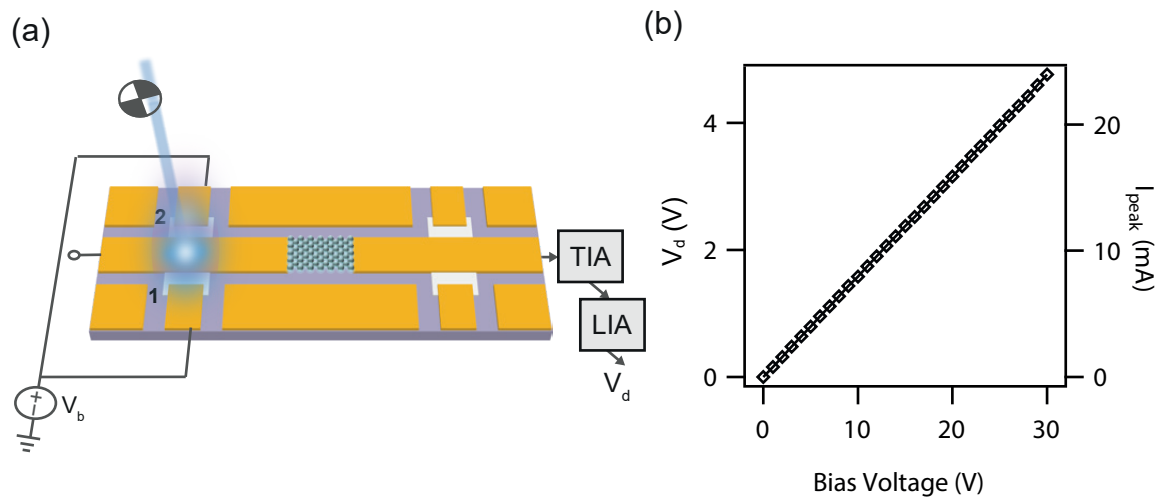


Figure C.1: **Calibration of picosecond currents.** **a**, Setup for calibration measurements. Switches 1 and 2 were biased with a voltage V_b and excited simultaneously, launching current pulses whose total charge was detected as a voltage V_d at the end of the signal line after amplification with a transimpedance amplifier (TIA) and lock-in amplifier (LIA). **b**, Detected voltage at the lock-in amplifier V_d and calibrated peak current I_{Peak} as a function of the bias voltage.

Appendix D

Processing of ultrafast voltmeter data

D.1 Raw data

The unprocessed data for the ultrafast voltmeter experiment discussed in Chapter 6 is displayed in Figs. D.1, D.2, D.3, and D.4, alongside the calibration curves in Fig. D.5.

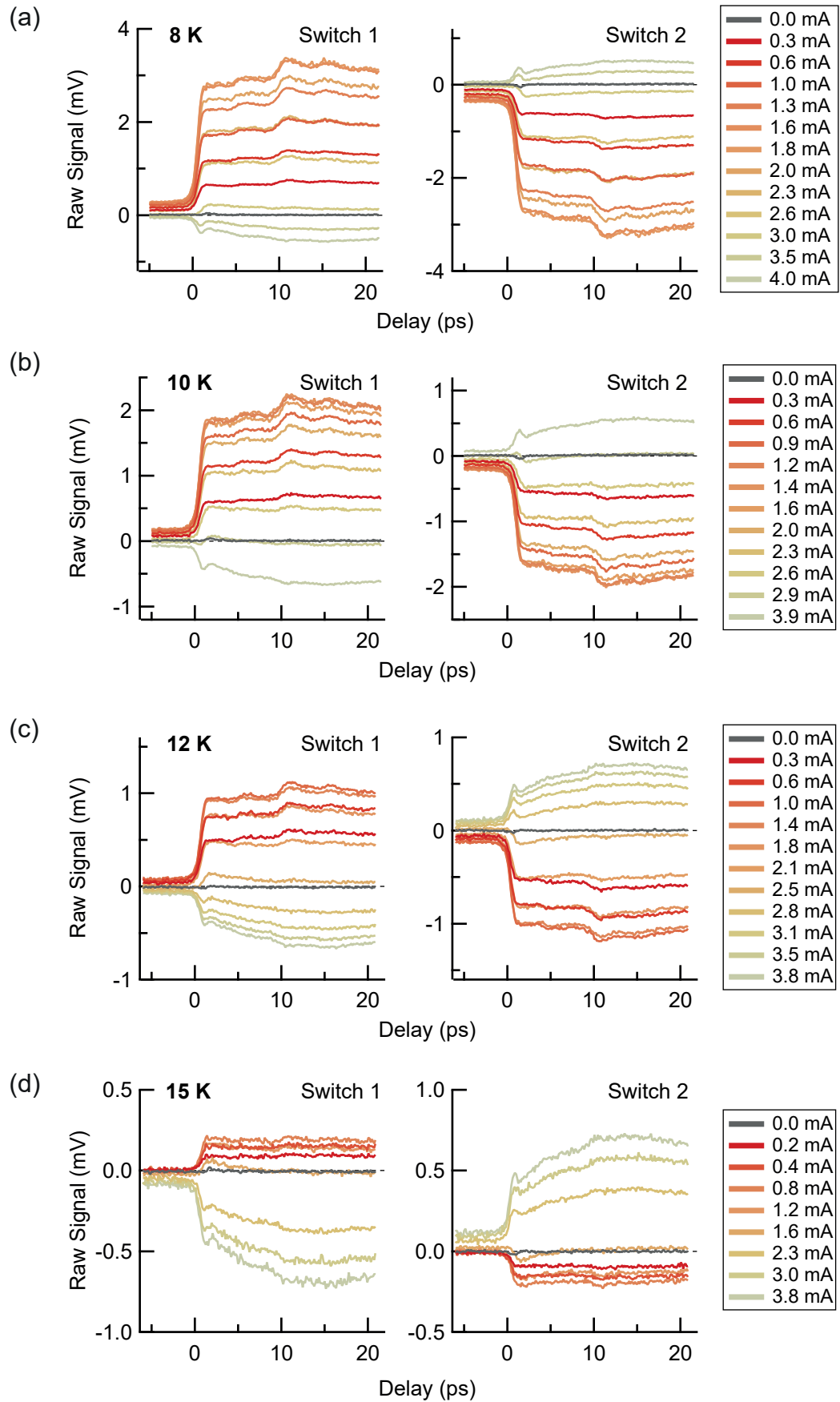


Figure D.1: **Raw high-fluence data** for $T < T_c$. Measured at **a** 8 K, **b** 10 K, **c** 12 K, and **d** 15 K with a fluence of 5 mJ cm^{-2} .

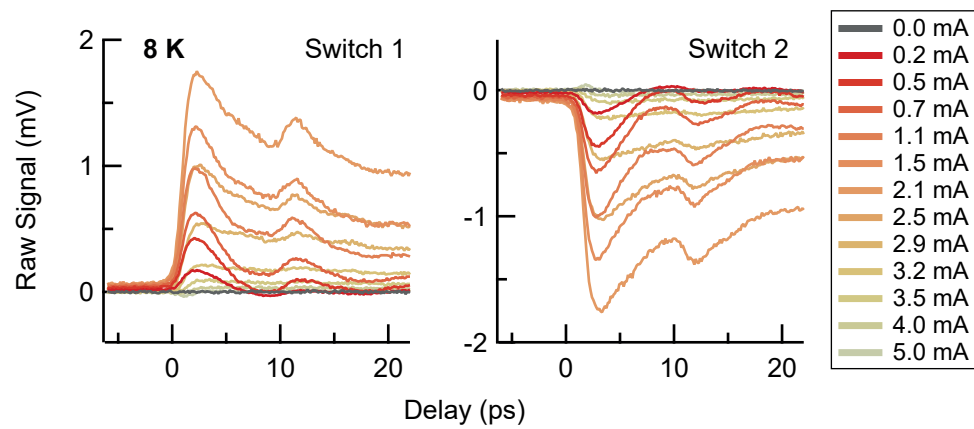


Figure D.2: **Raw low-fluence data at 8 K.** Measured with a fluence of $< 100 \mu\text{J cm}^{-2}$. Even before subtracting reflections, a bipolar response is observable for the smallest currents.

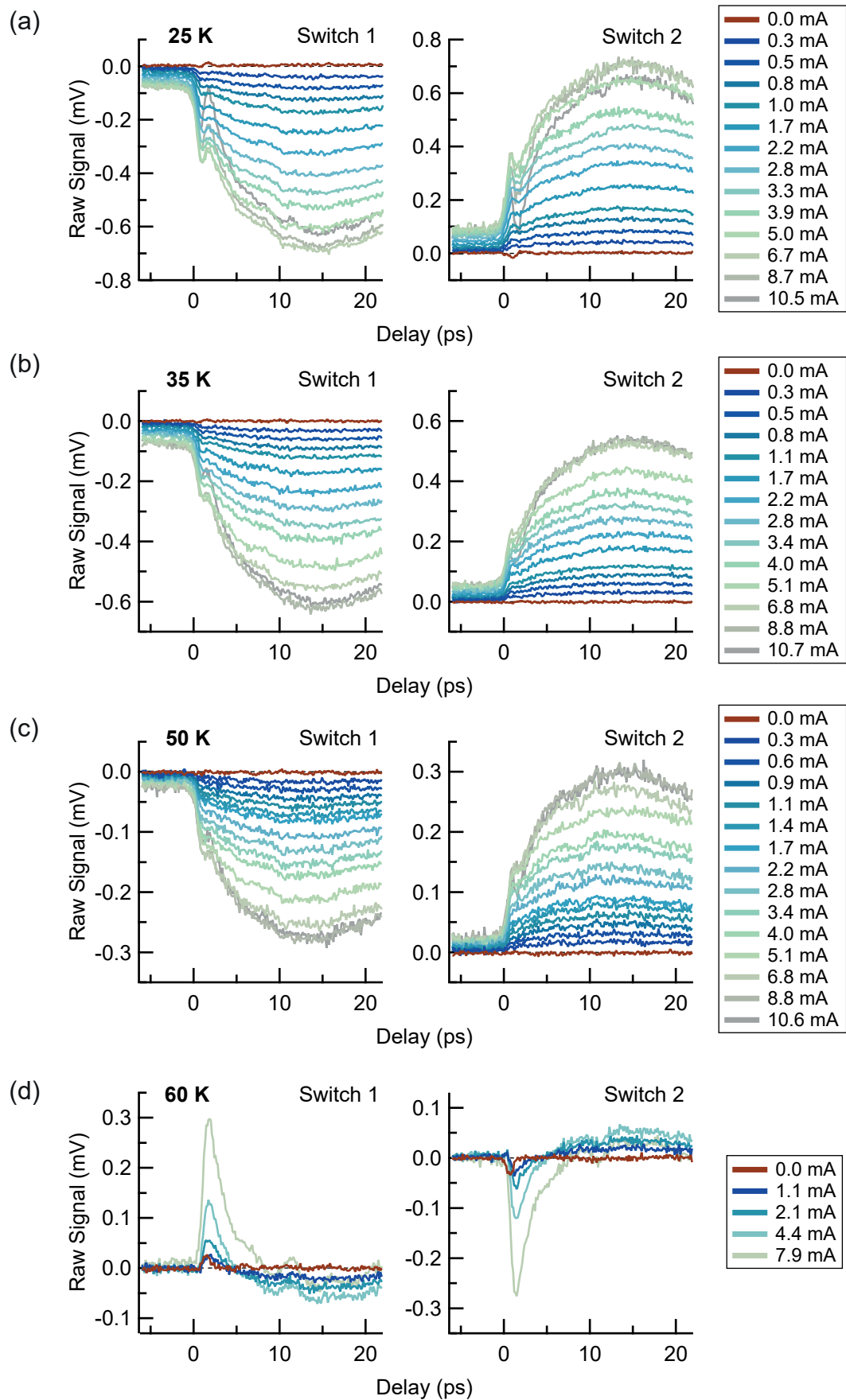


Figure D.3: **Raw data for $T > T_c$.** Measured at **a** 25 K, **b** 35 K, **c** 50 K, and **d** 60 K with a fluence of 5 mJ cm^{-2} .

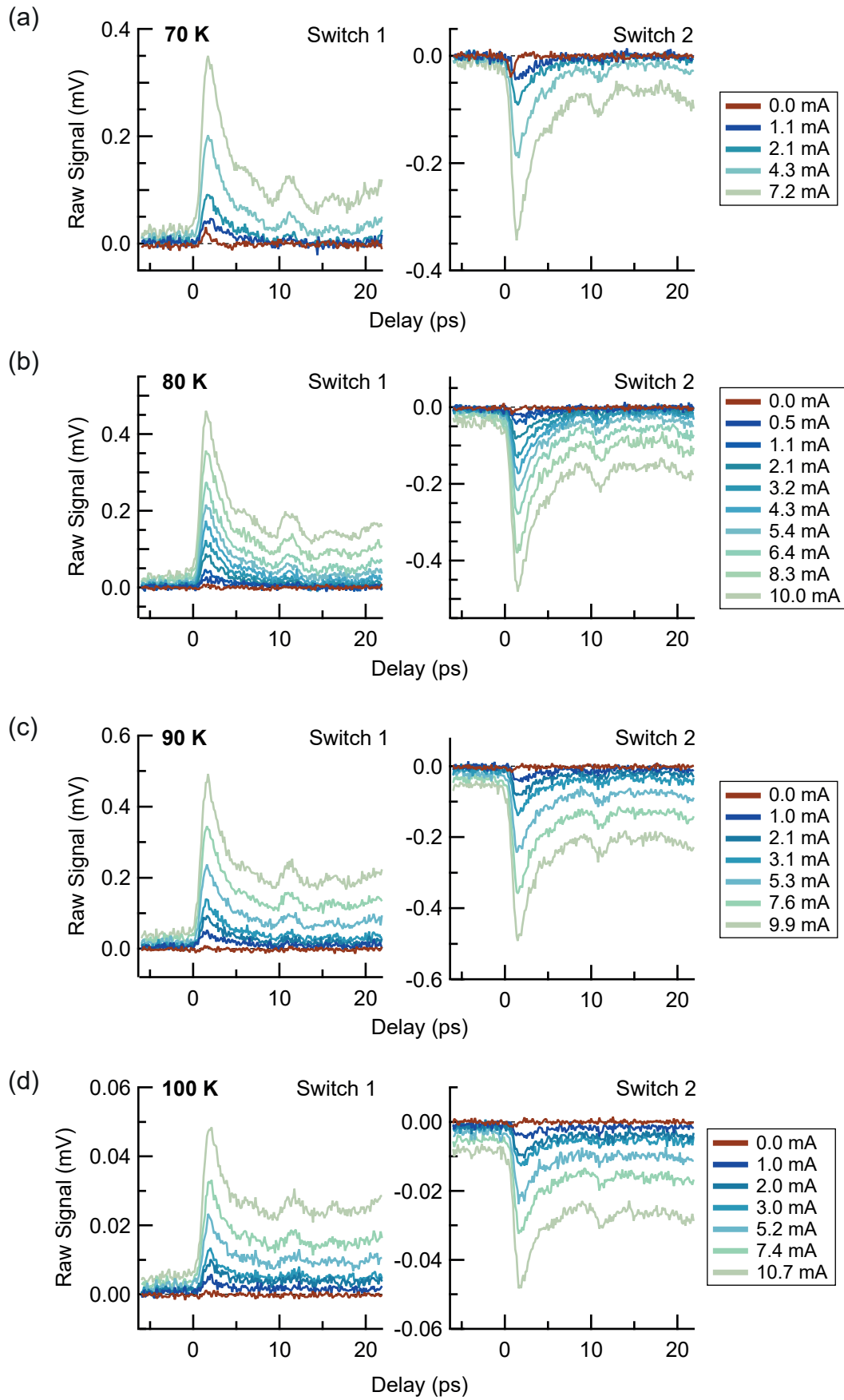


Figure D.4: **Raw data for $T > T_c$ (continued)**. Measured at **a** 70 K, **b** 80 K, **c** 90 K, and **d** 100 K with a fluence of 5 mJ cm^{-2} .

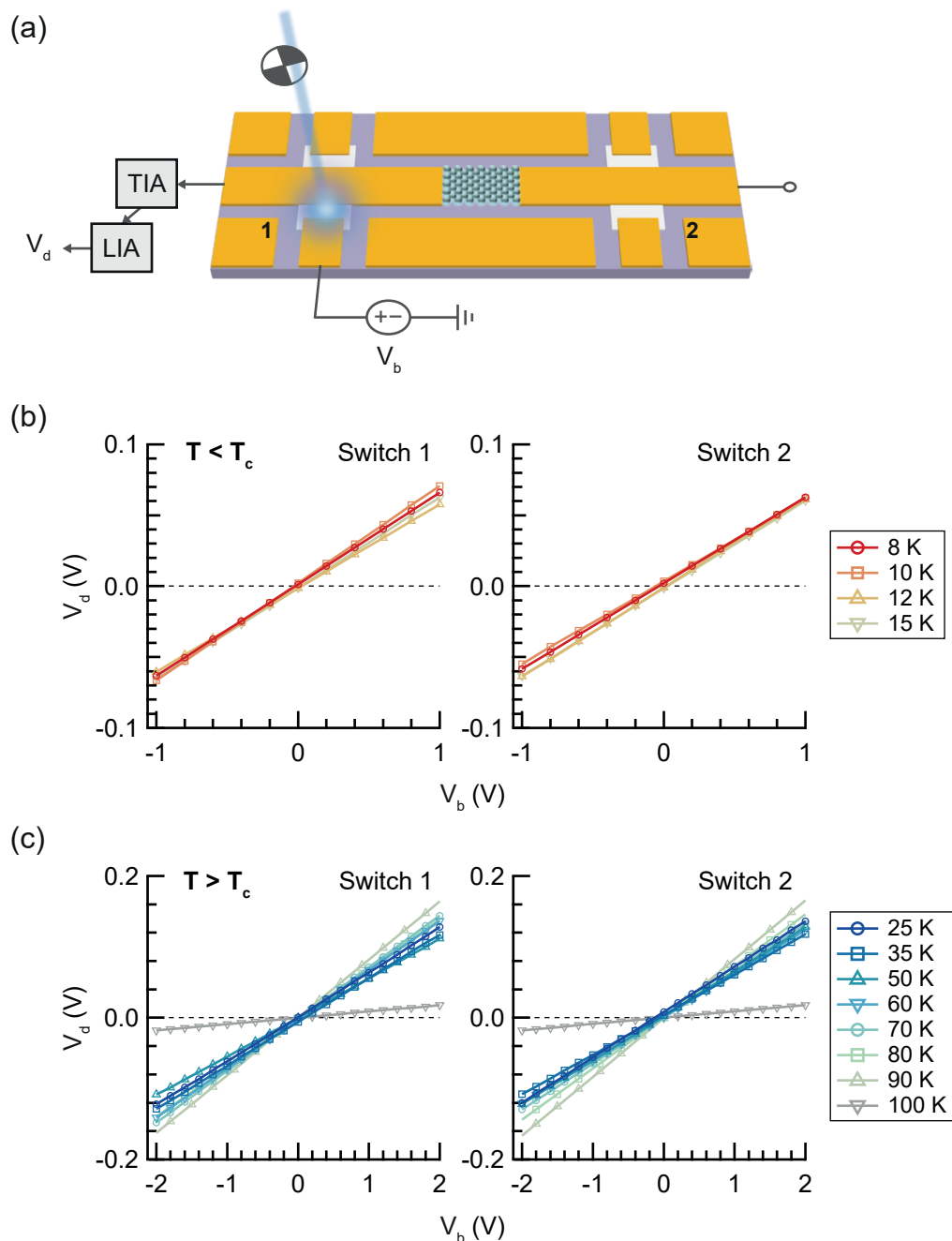


Figure D.5: **Calibration curves.** **a**, Configuration for the calibration measurements, as shown in Section 6.2.4. Shown below is the measured output voltage V_d of the photoconductive switches when photo-excited under a DC voltage bias V_b for temperatures **b** below T_c and **c** above T_c . The amplifier configuration was the same as that used in the time-resolved measurements—a transimpedance amplifier (TIA) followed by a lock-in amplifier (LIA). The gradient of these curves was used to retrieve the voltage in the waveguide from the measured raw signal. At all temperatures except 100 K, a transimpedance amplifier with an amplification factor of 2×10^9 V/A was used. At 100 K, a smaller amplification factor of 2×10^8 V/A was used to prevent lock-in amplifier overload due to dark currents at the high temperature, resulting in a smaller absolute magnitude of the signal.

D.2 Processed data

The complete data processing followed the description in Section 6.2.4, and the processed data is shown in Figs. D.6, D.7, D.8, and D.9.

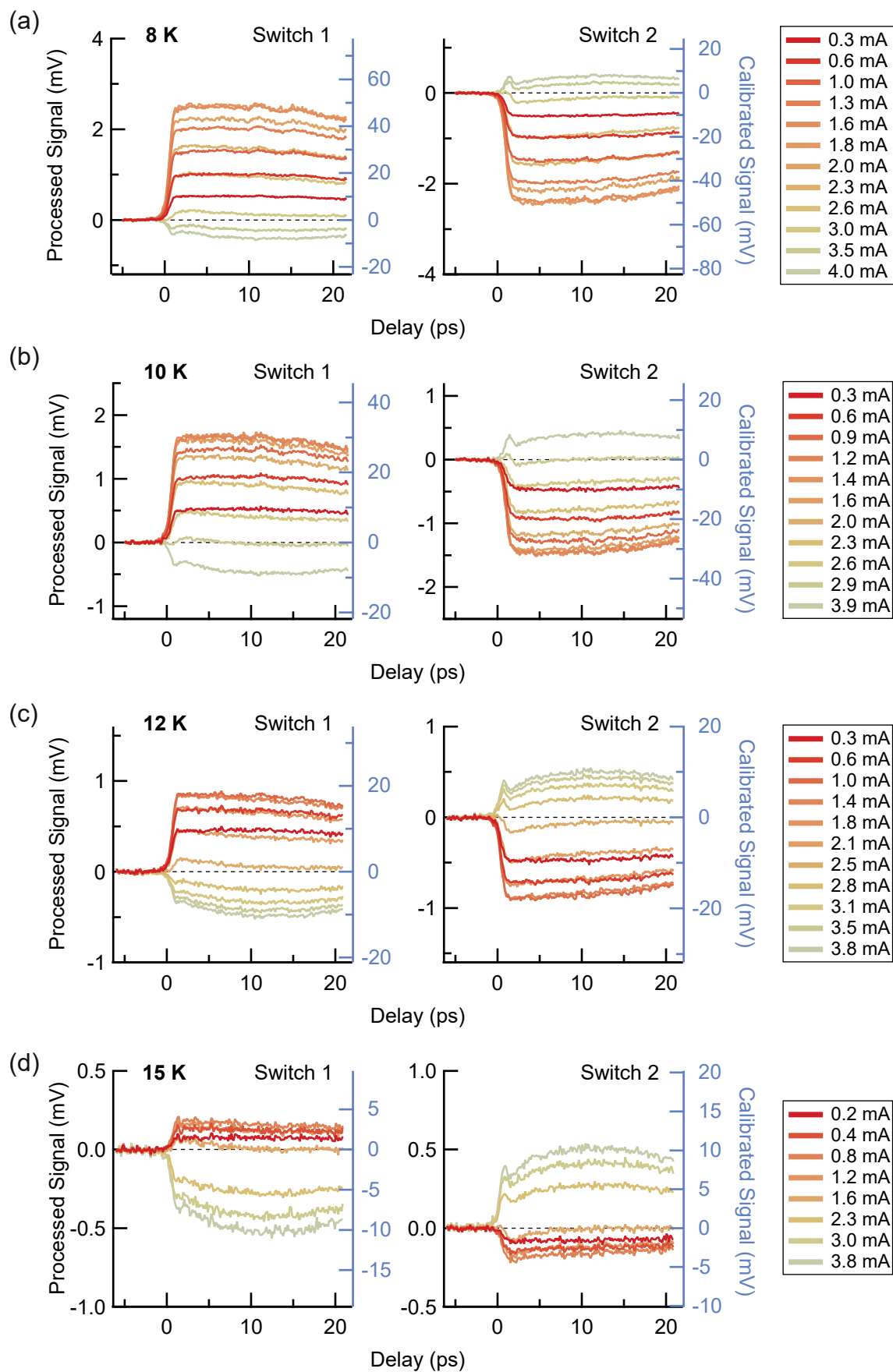


Figure D.6: **Processed high-fluence data for $T < T_c$.** Data is shown for **a** 8 K, **b** 10 K, **c** 12 K, and **d** 15 K, with a fluence of 5 mJ cm^{-2} , after subtraction of the before-time-zero offset, 0 mV signal, and reflections at 4.3 ps and 9.2 ps. The blue axes represent the calibrated voltages.

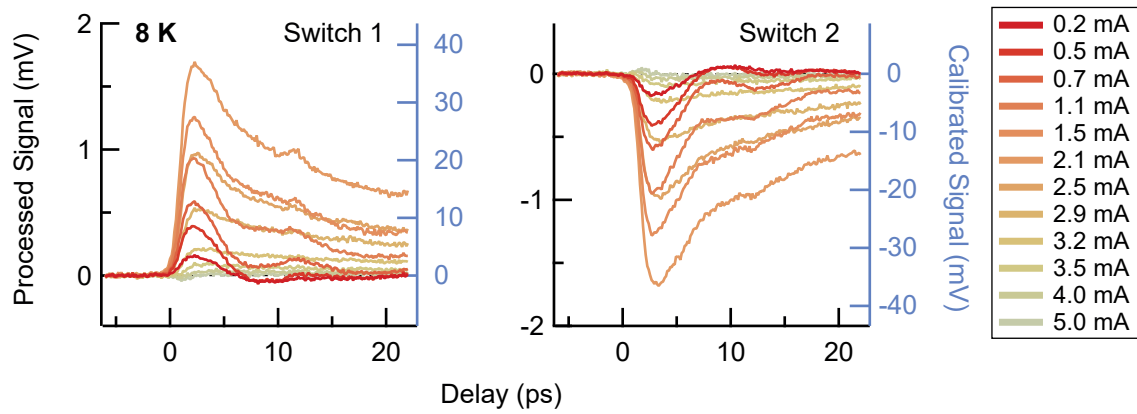


Figure D.7: **Processed low-fluence data at 8 K.** Data is shown for a fluence of $< 100 \text{ mJ cm}^{-2}$. The data is displayed after subtraction of the before-time-zero offset, 0 mV signal, and reflections at 4.3 ps and 9.2 ps. The blue axes represent the calibrated voltages.

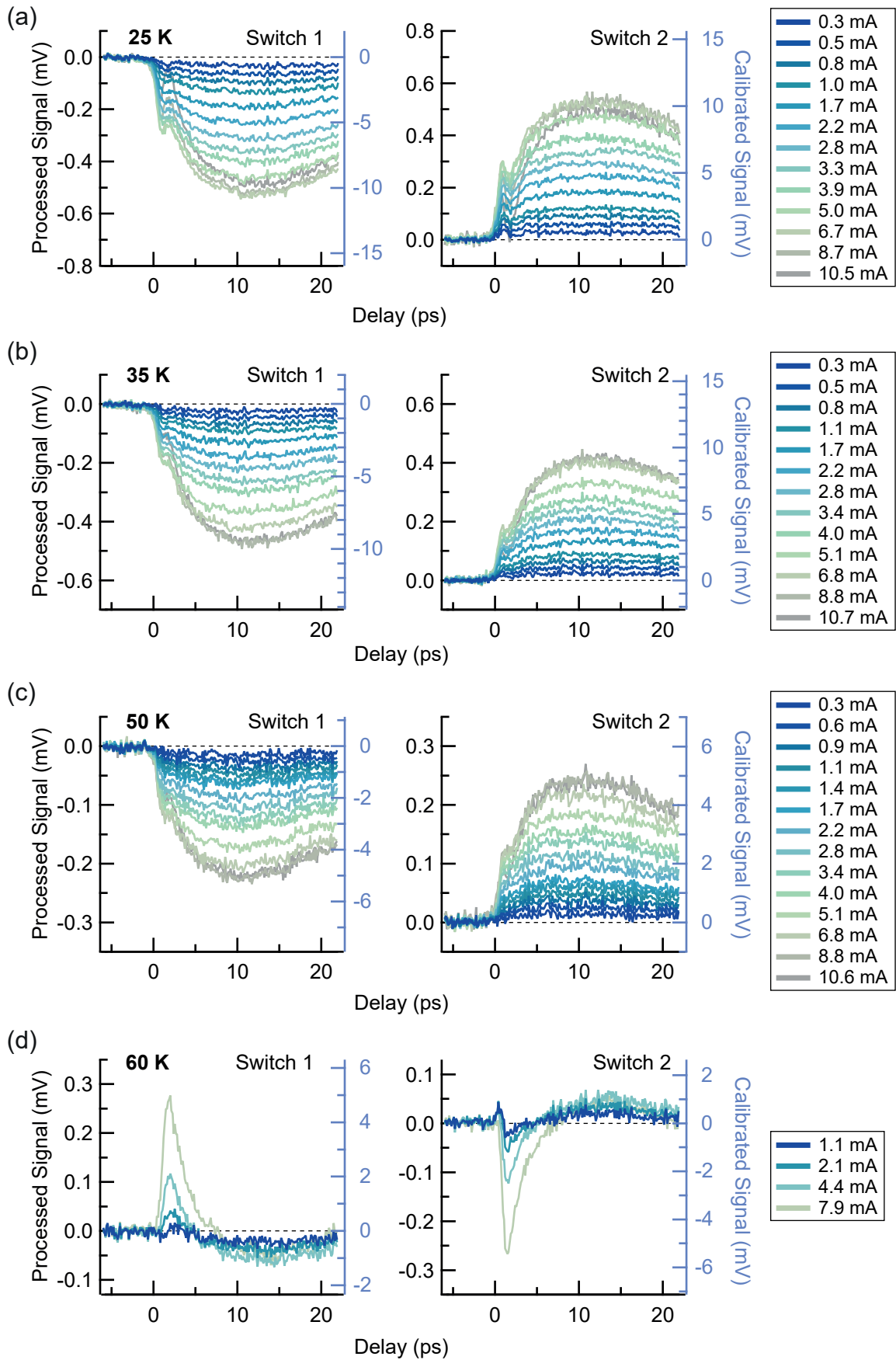


Figure D.8: **Processed data for $T < T_c$.** Data is shown for **a** 25 K, **b** 35 K, **c** 50 K, and **d** 60 K with a fluence of 5 mJ cm^{-2} , after subtraction of the offset, 0 mV signal, and reflections at 4.3 ps and 9.2 ps. The blue axes represent the calibrated voltages.

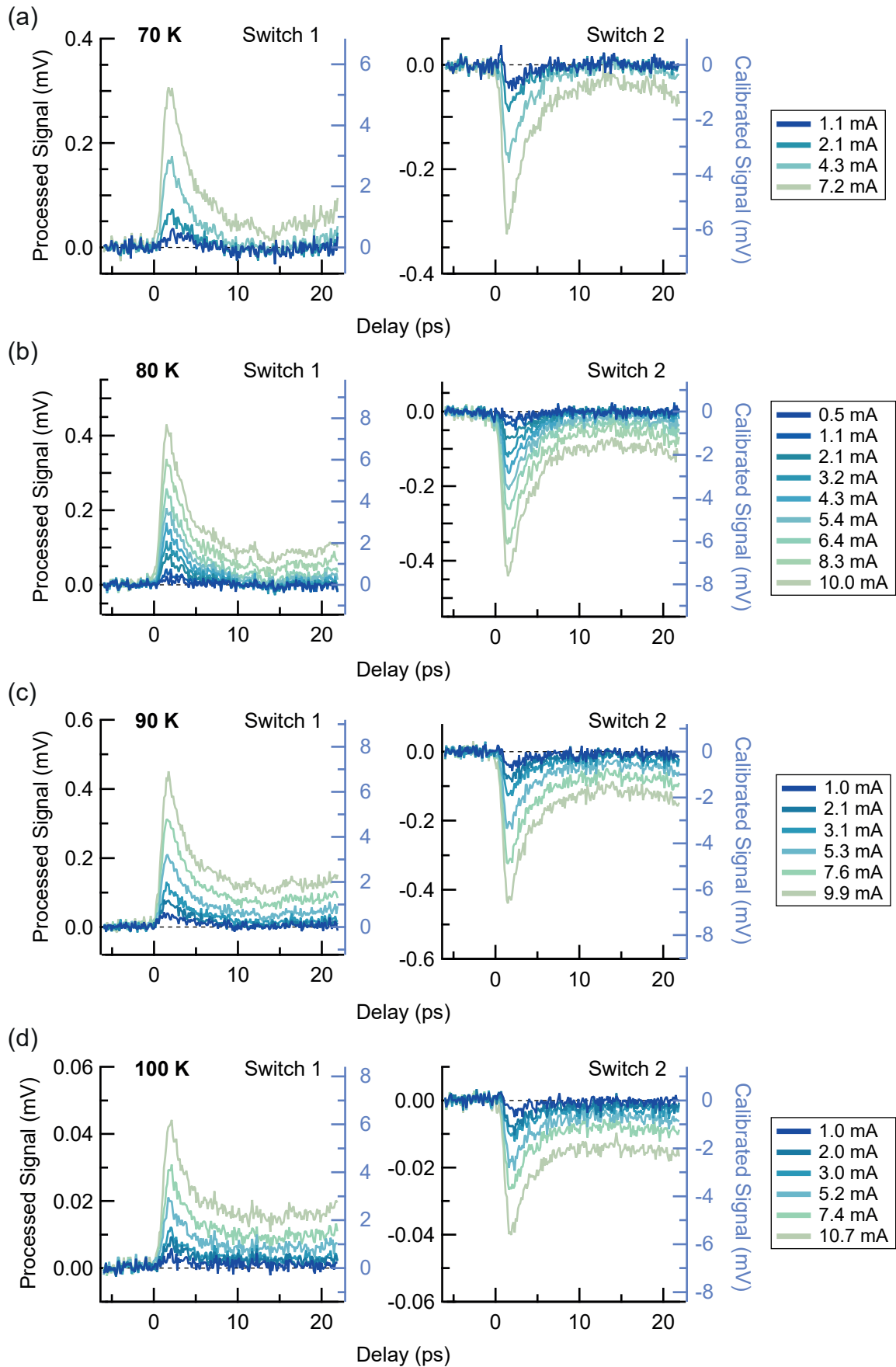


Figure D.9: **Processed data for $T < T_c$ (continued)**. Data is shown for **a** 70 K, **b** 80 K, **c** 90 K, and **d** 100 K, with a fluence of 5 mJ cm^{-2} , after subtraction of the offset, 0 mV signal, and reflections at 4.3 ps and 9.2 ps. The blue axes represent the calibrated voltages.